INFORMATION TO USERS

This manuscript has been reproduced from the microfilm master. UMI films the text directly from the original or copy submitted. Thus, some thesis and dissertation copies are in typewriter face, while others may be from any type of computer printer.

The quality of this reproduction is dependent upon the quality of the copy submitted. Broken or indistinct print, colored or poor quality illustrations and photographs, print bleedthrough, substandard margins, and improper alignment can adversely affect reproduction.

In the unlikely event that the author did not send UMI a complete manuscript and there are missing pages, these will be noted. Also, if unauthorized copyright material had to be removed, a note will indicate the deletion.

Oversize materials (e.g., maps, drawings, charts) are reproduced by sectioning the original, beginning at the upper left-hand corner and continuing from left to right in equal sections with small overlaps.

Photographs included in the original manuscript have been reproduced xerographically in this copy. Higher quality 6" x 9" black and white photographic prints are available for any photographs or illustrations appearing in this copy for an additional charge. Contact UMI directly to order.

ProQuest Information and Learning
300 North Zeeb Road, Ann Arbor, MI 48106-1346 USA
800-521-0600

TOWARDS IONIC SIGNAL PROPAGATION

by

Todd Sutherland
B. Sc. in Biochemistry, Simon Fraser University, 1997

A Dissertation Submitted in Partial Fulfillment of the
Requirements for the Degree of

DOCTOR OF PHILOSOPHY

in the Department of Chemistry

We accept this thesis as conforming
to the required standard

Dr. T. M. Fyles, Supervisor (Department of Chemistry)

Dr. D. A. Harrington, Departmental Member (Department of Chemistry)

Dr. R. G. Hicks, Departmental Member (Department of Chemistry)

Dr. B. F. Koop, Outside Member (Department of Biology)

Dr. G. A. Woolley, External Examiner (University of Toronto)

Supervisor: Dr. T. M. Fyles

ABSTRACT

The components necessary to propagate a synthetic ionic signal is described, and experiments leading to the required experimental system are the focus of this work. Two thiol-derivatized fluorescent probe molecules were synthesized that balanced both electrochemical and fluorescent properties necessary for trace analysis. Self-assembled monolayers (SAMs) of 11-(1-1'-biphenyl-4-yloxy)-1-undecanethiol were formed on Au/glass slides by open-circuit incubation and potential-assisted adsorption methods. A potentiostat was built capable of producing current responses on the microsecond time-scale.

Monolayer integrity was established by two methods: cyclic voltammetry and chronoamperometry. Monolayers formed under potential-assisted adsorption conditions showed attenuation of the peak current due to $Fe(CN)_6^{3-/4-}$ redox probe in cyclic voltammetry, indicating a tightly packed monolayer. Chronoamperometric studies also confirmed the monolayer integrity by fitting the current response of a potential-step to an equivalent circuit. The chronoamperometric study was dependent on solvent and electrolyte. In water, the difference between bare Au and monolayer protected Au was large, whereas in DMF, the difference was negligible. Likewise, the use of tetra-butyl ammonium hexafluorophosphate as the electrolyte showed little difference between bare Au and monolayer protected Au.

The electrochemical reduction of the SAMs was done in various solvents and electrolytes and the products were analysed by HPLC with fluorescent detection. Along the series of solvents from water to MeCN to DMF the current efficiencies for release increased but still were very low. In water and MeCN, the thiol was the sole detectable product, while in DMF, the sole detected product was the disulfide. Reproducibility of release was poor in MeCN and water, probably due to the low solubility of the thiol.

Single-channel analysis of two acyclic bola-amphiphiles (diester and diamide) was done to establish their feasibility as components of a synthetic signal propagation system. Channels from the diester derivative have a Na^+ conductance of 10.2 pS and a Cs^+ conductance of 39.3 pS. Channels from the diester have a Cs^+/Na^+ permeability ratio of 4.7, Cs^+/Cl^- permeability ratio of 7.5 and a Na^+/Cl^- permeability ratio of 3.1. Channels

of the diester bola-amphiphile have two lifetimes: 117 ms and 842 ms at -100 mV, 1 M CsCl electrolyte and DiPhyPC lipid at 25 °C. Similarly, Channels from the diamide derivative have a Na^+ conductance of 10.3 pS and a Cs^+ conductance of 38.9 pS. Channels of the diamide have a Cs^+/Na^+ permeability ratio of 5.2, Cs^+/Cl^- permeability ratio of 7.2 and a Na^+/Cl^- permeability ratio of 2.1. The diamide bola-amphiphile channels have a lifetime of 277 ms at +100 mV, 1 M CsCl electrolyte and DiPhyPC lipid at 25 °C. Both channels show a regular non-uniform step-conductance pattern. The sub-level openings, when graphically represented with lifetime data, show the trend that the lower conductance states of one-level openings are also the shorter-lived channels.

A traceless linker to release alcohols from a gold surface was developed. Thiobutyric acid was found to undergo intramolecular thiolactone formation after electrochemical reduction from an Au-electrode to liberate the alcohol. A thiobutyric ester at the C-terminus of gramicidin was synthesized. This compound released gramicidin by chemical reduction with DTT as seen by HPLC analysis and MALDI TOF MS. The electrochemical release of the Au-immobilized thiobutyric ester of gramicidin adjacent to a lipid bilayer, as monitored by bilayer clamp technique, produced an increase in channel activity that is consistent with incorporation of gramicidin.

Examiners:

Dr. T. M. Fyles, Supervisor (Department of Chemistry)

Dr. D. A. Harrington, Departmental Member (Department of Chemistry)

Dr. R. G. Hicks, Departmental Member (Department of Chemistry)

Dr. B. F. Koop, Outside Member (Department of Biology)

Dr. G. A. Woolley, External Examiner (University of Toronto)

Table of Contents

List of Tables

List of Figures

List of Schemes

List of Equations

List of Abbreviations

ATP	adenosine triphosphate
CN	cyano
CV	cyclic voltammetry
DIC	di-isopropyl carbodiimide
diPhyPC	diphytanoyl phosphatidylcholine
DMAP	N-N'-dimethyl aminopyridine
DMF	N-N'-dimethylformamide
DTT	dithiothreitol
EtOH	ethanol
FRET	fluorescent resonance energy transfer
HPLC	high pressure liquid chromatography
LC	liquid chromatography
LSV	linear sweep voltammetry
MALDI TOF MS	matrix assited laser desorption ionization time of flight mass spectrometry
MeCN	acetonitrile
ML	monolayer
MS	mass spectrometry
NMR	nuclear magnetic resonance
OMe	methoxy
PCB	printed circuit board
QCM	quartz-crystal microbalance
SAMs	self-assembled monolayers
t-butanol	tertiary butanol
TFA	trifluoroacetic acid
THF	tetra hydrofuran
TLC	thin layer chromatography
UV-Visible	ultraviolet-visible

Acknowledgements

- Dr. Fyles for his countless discussions, encouragement, enthusiasm for science and creating a challenging project.
- Dr. Harrington, Dr. Labayen and R. Dean for their help in the design of the potentiostat.
- R. Rowe for his help in teaching the Electronic CAD software to layout and print the circuit boards of the potentiostat.
- P. Eggers for his synthesis of the ion-channel compounds.
- M. Buchmann, T. Mischki and V. Yip for their synthetic contributions in the traceless linker experiments.
- Fellow graduate students at UVic for many discussions; particularly, Pedro, Chiwei, Blair, Dave, Marty, Greg and Miguel.
- Katriona Duncan for her editorial comments.
- Richard Robinson for his creation of a micro puncturing device.
- The Department of Chemistry secretarial staff for smoothing the administrative bumps along the way.
- My parents for their continual support
- Andria Dyck for her day-to-day support, encouragement and patience.

ASMD

Chapter 1 Ionic Signal Propagation

1.1 Ion-channels

Ion-channels are an essential element for cells to communicate with their environment. Ion-channels are found throughout all living organisms from single-cell structures, where they regulate osmotic pressure, to multi-cellular organisms where they permit the transfer of information over macroscopic distances. Without the ability to interact with, and respond to, changes in the environment, survival outlook is dismal at best. Thus, structures that permit the flow of information across an otherwise impermeable membrane are critical to survival. In animals, information is communicated by two methods: electrical signals and chemical signals. Electrical signals are transmitted by local ionic concentration changes on opposing sides of a lipid bilayer whereas chemical signals transmit signals via messenger molecules that are recognized by specific chemical receptor molecules. The important distinction between these two classifications arises in that electric signals are transmitted through a single cell whilst chemical messengers allow communication between cells. Therefore, both systems are necessary for complete information transfer. An example of the function of a chemical messenger system would be the pituitary gland of the brain releasing a hormone, that hormone finding its way to the receptors on the surface of a cell, and once bound the hormone would induce some change in

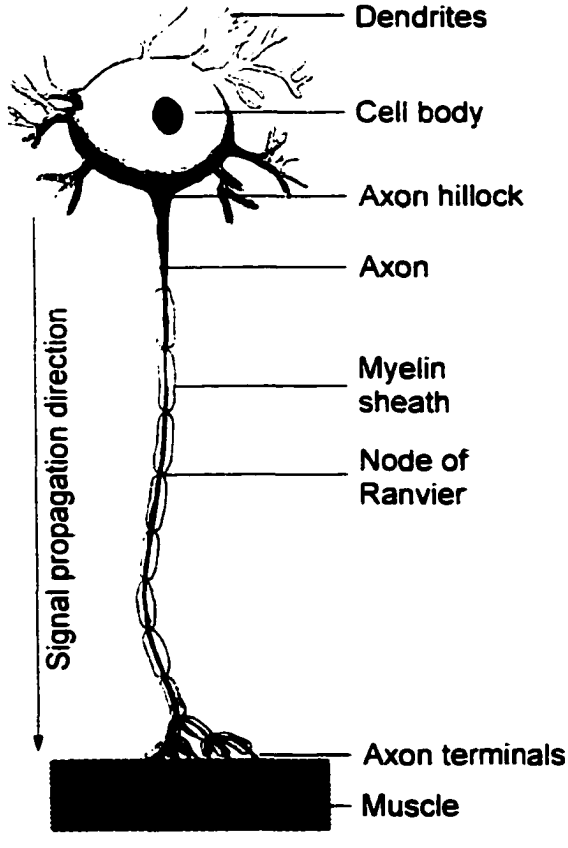

Figure 1-1. Structure of typical motor neuron. Adapted from Molecular Cell Biology, 3rd ed. Darnell, J. Redrawn by A. Lu.

cellular operation. Relying solely on chemical messengers to do sensory signaling would cause several problems. Messengers work by diffusing through the extra cellular medium until binding to a receptor cell, which in turn reacts according to the receptor. This diffusion mechanism of propagation is inherently slow. Furthermore, a diffusible messenger is diluted as it propagates and is prone to chemical interference. However, ion-channels in conjunction with chemical signal propagation can lead to a variety of environmental stimuli being sensed such as, light, touch, pressure, sound and odour.

Electrical signal propagation within one cell is a well-studied area. Much is known about the physiological properties of certain neurons and their responses to different stimuli. Studies have elucidated the process of signal propagation at a biochemical level, but molecular level mechanistic insight remains elusive[1]. Results since the 1930s have shown that ionic signals are propagated by ion-channels imbedded in lipid bilayers in specialized cells called neurons[1], illustrated in Figure 1-1. Each neuron has the capacity to make contact with 10^4 other neurons through dendrites. The human brain contains trillions of neurons and each one of those neurons makes up to ten thousand connections. The massive extent of parallel circuitry is unmatched even by today's growing electronic device complexity. Haarer[2] has compared the human brain to hard disk drives in the personal computer. The brain has a memory-capacity on the order of 10^{15} bits. To mimic this memory capacity one would need 100 000 ten gigabyte hard drives each consuming about 50 Watts of power. In total, 5 MW of power would be consumed to match the brain's storage capability; the brain consumes only tens of Watts for both storage and processing, an energy consumption difference of five orders of magnitude.

At the most basic level, signal propagation is carried out by ion-channels. There are many different families of ion-channels. For example, there are those that only allow the transport of specific cations[3] such as Na^+ or Ca^{2+}. Other channels[4] only have permeability to anions like Cl^-. Aside from their selective permeability, ion-channels are often under the control of various properties of their environment. The Na^+ channel in neurons, for example, has a gating mechanism that closes its permeability to Na^+ at negative membrane potentials and drastically alters its permeability at slightly more positive potentials[5]. Many diseases are known to stem from ion-channel defects. Cystic

fibrosis is a life threatening disease with defective chloride channels at its root. Cardiac arrhythmia is sometimes caused by a genetic mutation in a K^+ channel.

Structurally, many protein channels appear to be built of multiple transmembrane segments. Bundles of helices forming pores in lipid membranes are common in biological ion-channel formation and as a result, this mode of action has become known as the barrel-stave model. A space-filling model of an α-helix clearly shows there is very little free volume down its axis thus ion-conduction is extremely unlikely to function by this mechanism. Transport occurs adjacent to the helices in a cluster.

Recent papers[6-9] have shown the path taken by a K^+ ion as it transports through a KcsA K^+ ion-channel by obtaining detailed crystal structures at various K^+ concentrations. The ion-channel's opening provides the selectivity filter based on size and charge. The K^+ ion must first lose it hydration shell before it can be transported so the structure of the ion-channel carbonyl groups are positioned along the inside to mimic a hydration shell while each K^+ is transported. The transport across a lipid membrane operates in an assembly-line fashion with each K^+ hopping along to the next carbonyl coordination site down its concentration gradient. The crystal structure also showed that the coordinating carbonyl groups alter their position in response to low local K^+ concentrations. The principle findings were not surprising, as the mechanism had been correctly postulated from extensive experimental evidence, but the confirmation of mechanism by a crystal structure in such a complex system at atomic resolution is very rare. The lack of information regarding mechanistic detail at the molecular level of ion-channel activity has led chemists to synthesize ion-channels to provide a simpler ion-channel model where structure-activity relationships and mechanism can be deduced.

1.1.1 Synthetic Peptide Models

Recent examples of synthetic peptides that form ion-channels reported by DeGrado[10] and Woolley[11-13] are used as representatives of this large field. DeGrado used a 21-residue amphiphilic polypeptide to determine the electrostatic effects on ion selectivity and rectification. Three structures below (Figure 1-2) were synthesized and their corresponding properties were tested. The 21-mer structure, $(LSSLLSL)_3$, has been

characterized in previous papers[14,15] and found to organize into an α-helical structure denoted by the sketch where the N and C correspond to the N-terminus and C-terminus, respectively. The helices are 40 Å and are thus long enough to span the lipid bilayer. Moreover, the active structure of the ion-channel is proposed to be a bundle of helices.

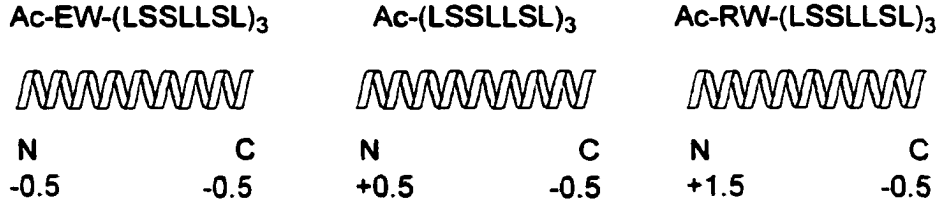

Figure 1-2. Amphiphilic peptides for determination of electrostatic effects on ion-channels.

The channel-forming species is proposed to act in a hexameric aggregate with each helix oriented perpendicular to the lipid surface and spanning the bilayer. No experimental evidence concerning the helices parallel or anti-parallel orientation was given. The middle structure of Figure 1-2 has an overall neutral charge but because of the way amide bonds align in an α-helix, a -0.5 charge resides at the C-terminus and a +0.5 charge resides at the N-terminus. Addition of a formal negatively charged glutamate residue to the N-terminus results in an overall –0.5 charge at both ends of the helix as shown in the leftmost structure in Figure 1-2. Conversely, addition of a positively charged arginine residue gives the N-terminus an overall +1.5 charge and the C-terminus remains unchanged as shown in the rightmost structure. The tryptophan residue was added as a spectroscopic tag and was used to determine its local environment. Ion-channels from the overall neutral helix showed modest cation selectivity and exhibited asymmetric current-voltage curves. The glutamate derivative converted the channel to become more cation selective at the expense of losing rectification. The arginine adduct lost much of its cation selectivity but gained in the area of rectification. Clearly, the electrostatics play a major role in both ion selectivity and ion flux.

Using a different approach, Woolley has taken natural ion-channels and covalently modified their structure to alter their properties. The goal of the work is to

take the well-characterised ion-channel systems, gramicidin and alamethicin, and modify their structures to gain a measure of control over the transport. Gramicidin contains a terminal hydroxyl that was covalently modified with an azobenzene derivative. The principle of operation is that the *cis/trans* transformation of the azobenzene will provide a photo-driven gate at the entrance of the ion-channels. General shapes and characteristics are illustrated in Figure 1-3. Gramicidin is a cation channel that in its bilayer active form is arranged in a head-to-head dimer as indicated by the two N-termini adjacent to one

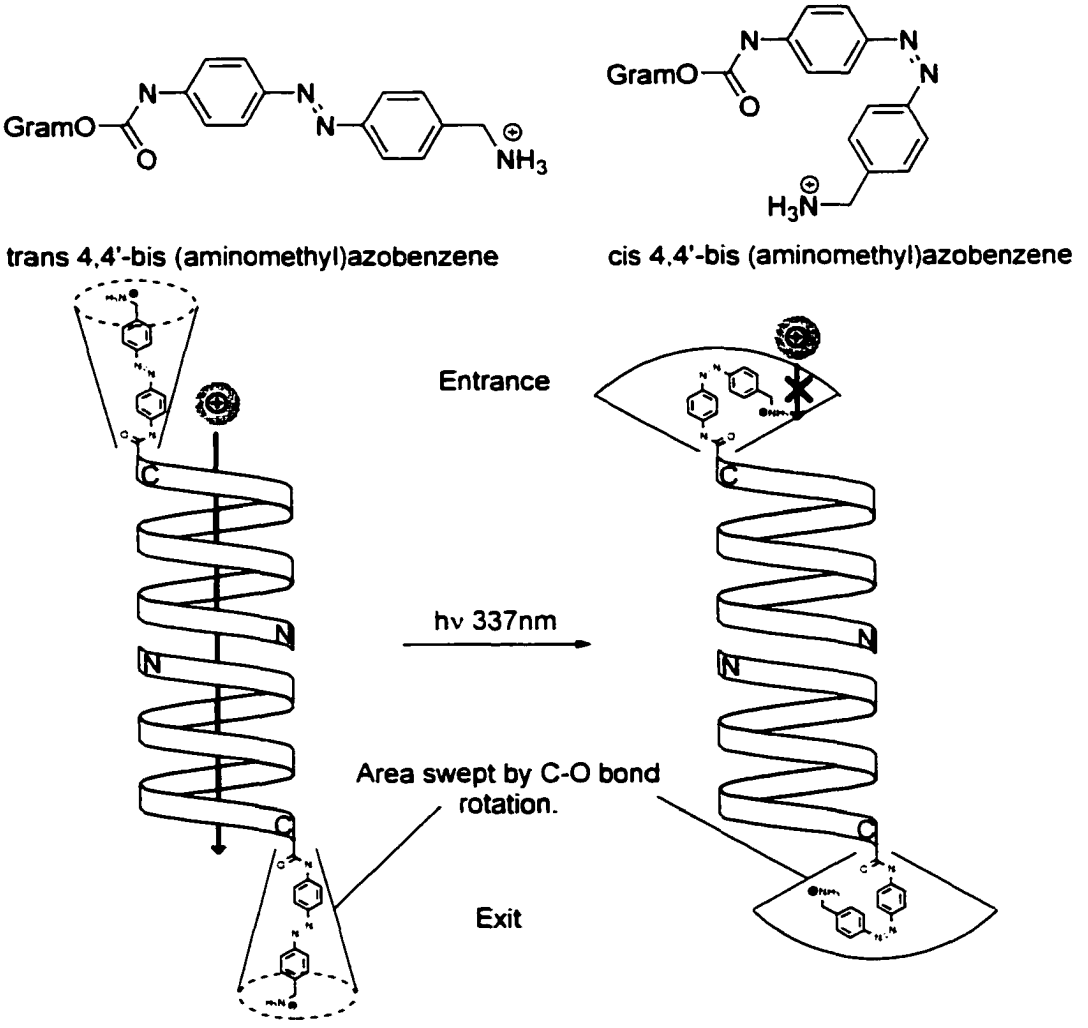

Figure 1-3. Schematic of azobenzene-modified gramicidin channels. The position of the *cis* and *trans* forms of azobenzene on dimer of gramicidin indicating the gating mechanism. The N and C notation refer to the N- and C-termini of the polypeptide, respectively.

another[16-22] and transport occurs down the axis of the β–helix. Unlike the α–helical aggregates described above, a structure that forms β-helices would have an internal opening of about 4 Å and would permit ion transport down its axis if length and

orientation were considered. As Figure 1-3 illustrates, *in situ* irradiation of the *trans*-conducting-form converts to the less conducting *cis* form. The *trans* conformation of azobenzene positions the cationic ammonium further from the entrance of the ion-channel enabling cations to pass through the β-helix unimpeded. However, the *cis* conformation positions the cationic ammonium near the entrance of the ion-channel providing an electrostatic block of cations. Irradiation at 337 nm yielded predominantly the *cis* conformer. The area swept by rotating around the C-O bond of the carbamate linker to gramicidin shows more interference with cation conduction down the β-helix in the *cis* case than compared to the *trans* case. The current trace of the azobeneze derivatized gramicidin showed four discrete levels attributed to the four pairs of isomers, *trans*/*trans*, *trans* (entrance)/*cis* (exit), *cis* (entrance)/*trans* (exit) and *cis*/*cis*, in order of decreasing current magnitude. The results imply that effective gating is best achieved by gating at the entrance to the ion-channel rather than the exit. Another paper[13] by the same author shows how a photo-isomerizable azobenzene can be introduced to a helical peptide and depending on the azobenzene conformation alter the helical structure. This is an excellent example of a method to induce gating by a conformational change instead of a blocking agent as Figure 1-3.

Cation/anion selectivity was accomplished by synthesizing an analog of alamethicin where the glycine at position 18 has been substituted by lysine. Alamethicin is known to operate by a barrel stave mechanism, sketched in Figure 1-4. Each bilayer-spanning helical peptide is represented by a cylinder. Native alamethicin demonstrates voltage-dependent properties and the aggregate number can range from 6 to 12 even though the octamer is the only structure shown in Figure 1-4. The addition of lysine introduces a positive charge to the pore lining of each cylinder of the aggregate,

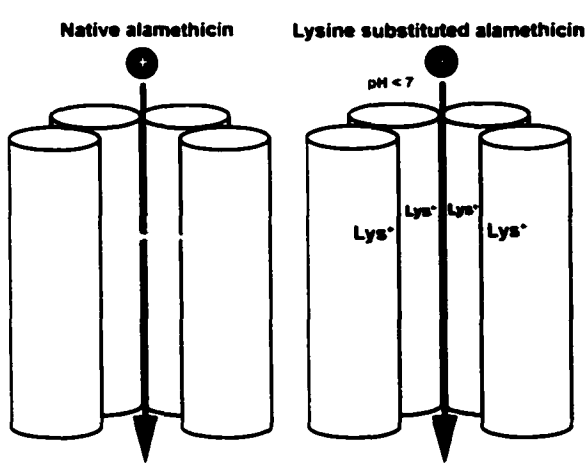

Figure 1-4. Schematic of one-half of an octameric aggregate of alamethicin

which alters its native cation selectivity to favoring anions. In addition, the selectivity is also governed by pH, where at neutral pH values, the channel is anion selective and at pH values greater than 11, only cation selectivity was found.

There are numerous other peptide based approaches to probing similar questions but the examples above are good representations of the techniques used and the analysis of structure-activity relationships.

1.1.2 Synthetic Non-peptidic Ion-channels

The information learned from natural and synthetic peptide ion-channels has led to many design principles thought to be critical to channel function. It is usually assumed the active channel structure spans the bilayer and therfore must have an overall length of about 40 Å. Although this could be achieved by one molecule, it is also possible to envisage end-to-end dimers. However, some stabilization feature must be included to bring the two ends of the dimer together. The structure must be amphiphilic, meaning it must have a polar head group as to align itself with the head groups of neighbouring phospholipids and a non-polar region to allow partitioning into the hydrophobic region of the bilayer. Since the mode of ion-transport is believed to involve dehydration of an ion during transport, donor groups should line the inside of the pore to lower the dehydration energy. Also, it is assumed the channel should have a roughly columnar shape to "fit in" with the columnar shape of the phospholipids. The last twenty years has seen many groups synthesize, analyze and modify structures that follow these design principles but for the purpose of this introduction, only a representative selection of recent work will be discussed to illustrate the current position of the field[23-29].

Kobuke[30,31] has recently synthesized channel-forming compounds containing cholic acid derivatives. Two families of derivatives are shown in Figure 1-5. The topmost structure is a resorcin[4]arene with cholic ether groups in the R positions; the next two compounds belong to the same family where the only difference lies in the formal charges on the terminal portions of the molecules. The resorcin[4]arene compound is proposed to form tail-to-tail dimers in the bilayer with the polar alcohol groups pointing into the aqueous side of the bilayer and the steroidal ethers pointing

towards one another within the lipid layer forming a hydrophilic channel. The resorcin[4]arene structure is sufficiently rigid to discriminate between cations based on size. The alcohol groups will decrease the dehydration energy required to transport the ion to yield a highly conducting, cation selective pore. A cation selectivity of P_K/P_{Na} of 2.8 was achieved, however, the channel exhibited Ohmic behaviour. The last two compounds in Figure 1-5 link two amphiphilic cholic acid methyl ethers through a

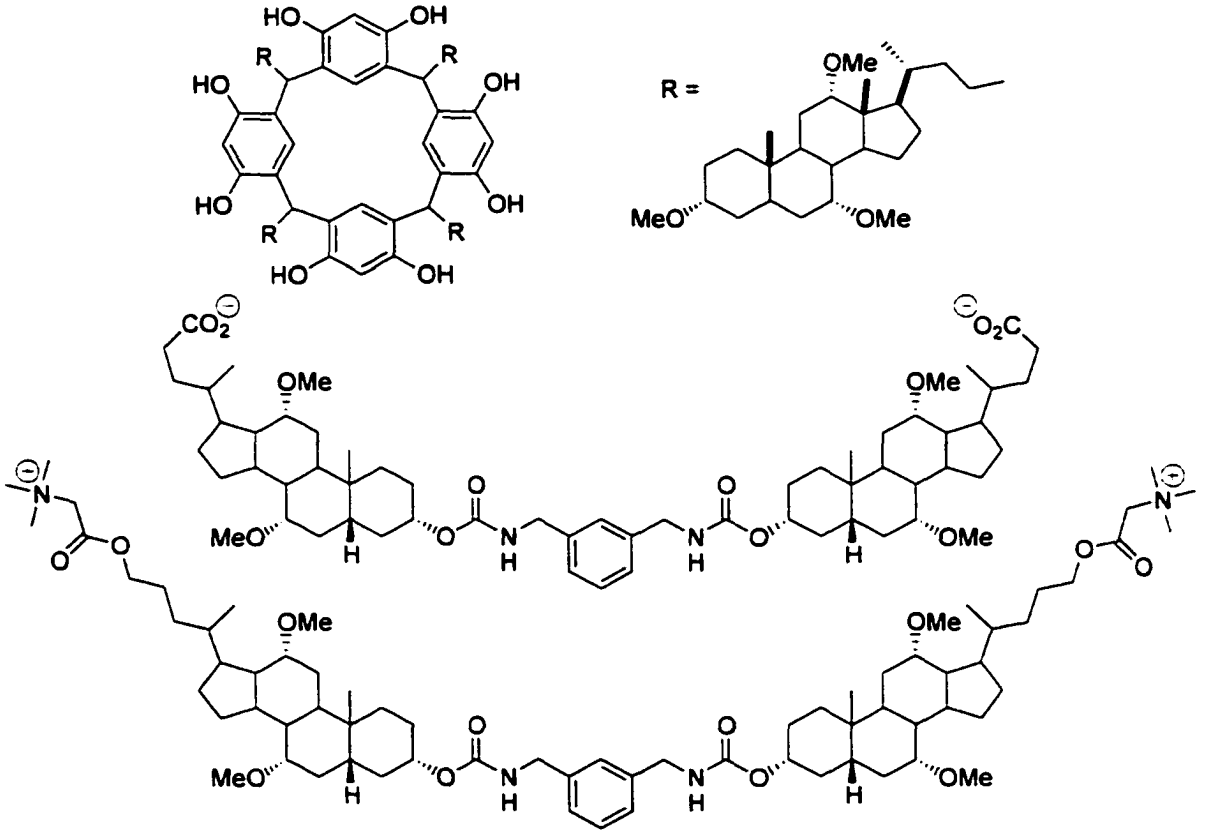

Figure 1-5. Three cholic acid derivatives that act as ion-channels.

biscarbamate. In this system the results are not much different from the previous findings but the effect of a negative charge in the headgroup region did alter the selectivity of cations over anions. The negatively charged diacid compound had a P_K/P_{Cl} of 17 while the positively charged bis-quaternary ammonium compound had a P_K/P_{Cl} of 7.9. These findings are in agreement with electrostatic reasoning whereby negative charges are most likely to be repelled from the channel entrance if there is a covalently bound negative charge already present. Furthermore, this system can be looked at as four covalently linked monomer units dimerising in the lipid bilayer to form the conducting channel.

These results support the argument that channel forming structures most likely operate in aggregates.

In the same vein, Regen[32-36] has employed the compounds shown in Figure 1-6, to elucidate structure-function relationships. Regen's work uses polyether-sterol conjugates as ionophores. The mode of action is similar to the barrel stave model except in this case the staves of the barrel only span half of the lipid membrane meaning lateral relaxation dynamics play a role in channel formation. This type of mechanism is known

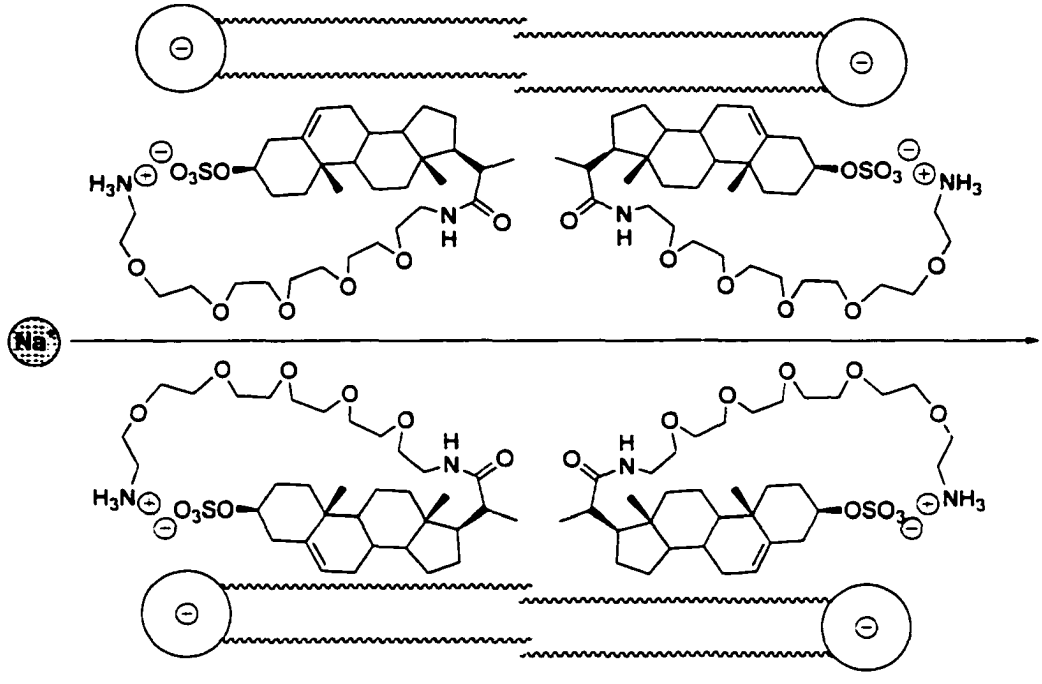

Figure 1-6. The structure of squalamine analog and its proposed mode of action in lipid bilayers.

in nature: it is the mode of action for amphotericin B[37]. The synthetic system is a mimic of the antimicrobial sterol squalamine, which may itself act via an amphiphilic mechanism. The polyether chains are proposed to line the pore of the channel while the hydrophobic sterols lie in each leaflet of the bilayer. This conformation permits a water-filled pore to span the lipid bilayer once the two halves of the channels diffuse together. The polyether-sterol adduct also exhibits different activities in different lipid environments[33]. The activity of the ionophore in negatively charged lipids (egg phosphatidylglycerol) is enhanced compared to the same experiments in a neutral lipid environment (egg phosphatidylcholine). The results clearly show electrostatic interactions with the surrounding lipid environment play a crucial role in channel

activation. This is the first documented example of an ion-channel system that displays both lipid and ion selectivity.

Another compound Regen studied[35] is very similar to Kobuke's resorcin[4]arene and is shown below in Figure 1-7. The main difference is that spermine has many more degrees of freedom than resorcin[4]arene and as a result the pore formed cannot be as size selective. The significance of this compound comes mainly from its ease of synthesis. Spermine and cholic acid are commercially available and the entire synthesis is a one-step, one-pot reaction compared to Kobuke's multistep synthesis. This brings up an important point concerning synthetic strategy. Because most synthetic ion-channels to date have been difficult to synthesize, many groups are hesitant to apply extensive structural modifications to their target after characterisation is complete. To this end, a modular approach to synthesis is appealing since structural changes would be easily applied with little new chemistry. The modular approach to ion-channel synthesis is favored because

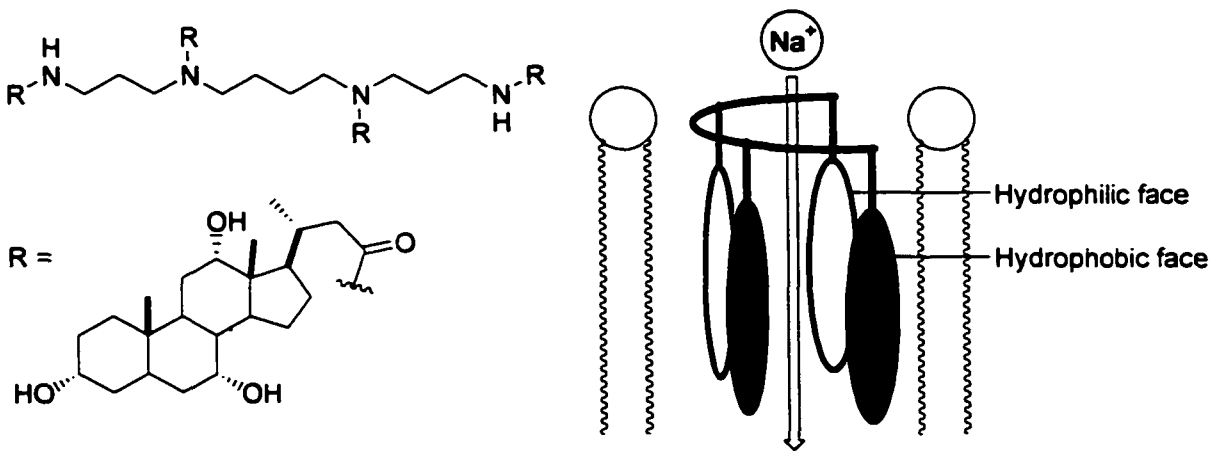

Figure 1-7. Scematic of a cholic acid-spermine condensation product and its orientation in a bilayer leaflet.

it allows a more diverse selection of structural variants to be tested with a small increment of additional effort.

The recent work of Matile[28,29,38-43] focuses on the effects of a permanent trans-membrane dipole on the voltage response properties of ion-channels. The family of molecules used are oligo(*p*-phenylene) rods shown in Figure 1-8. Matile systematically approaches ion-channels by varying one component at a time in a system that is relatively

constrained compared to others mentioned above. The oligo(*p*-phenylene) backbone is

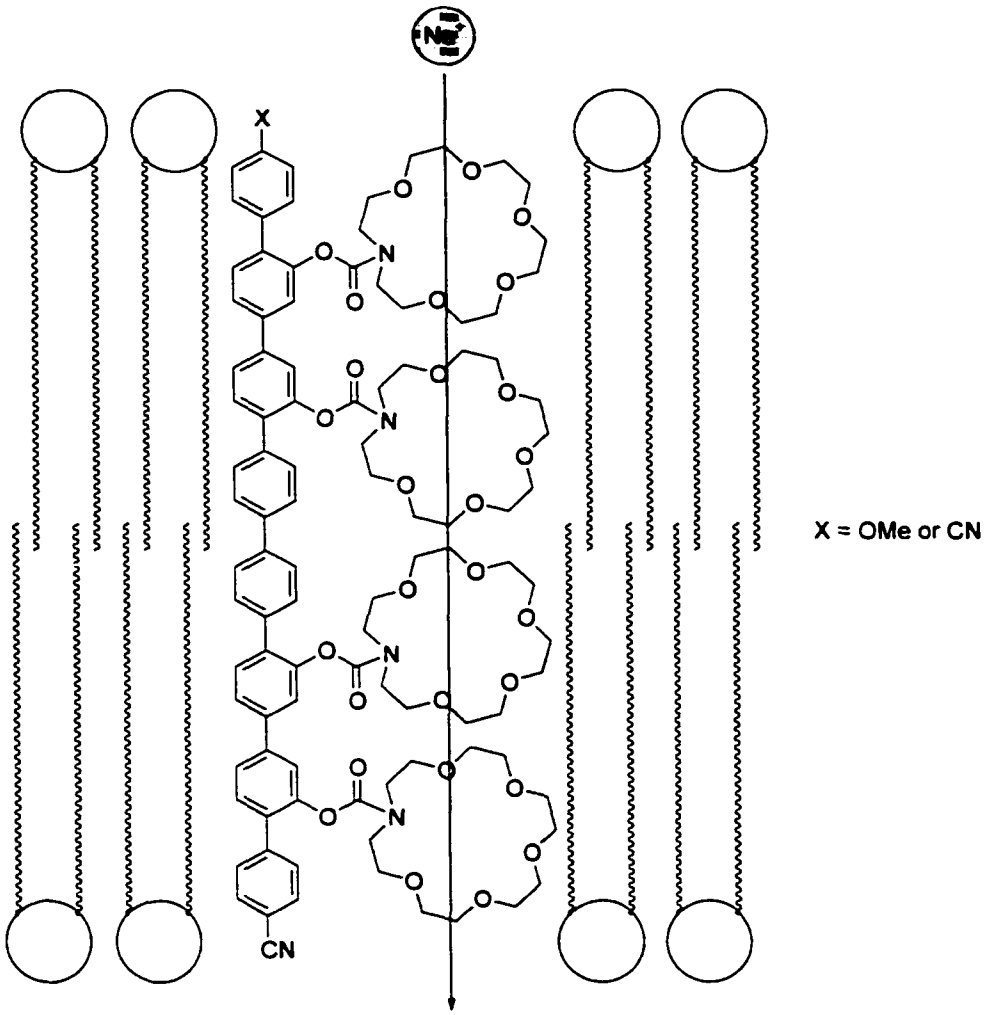

Figure 1-8. Schematic of an oligo(*p*-phenylene) derivative and its proposed insertion orientation in a lipid bilayer.

rigid, therefore minimizing conformational complexity. As well, it acts as an extended fluorophore to monitor local environments. Off the rigid rod are crown ethers, which permit a continuous column of water to traverse the lipid bilayer and conduct ions as illustrated in Figure 1-8. The substitution of different terminal groups, labeled as either X or CN in Figure 1-8, allows a modular approach to systematically alter the permanent dipole moment along the rod. It is commonly accepted that introduction of a permanent dipole in a lipid spanning molecule will produce non-linear current-voltage behavior. Vesicle experiments clearly show the methoxy-derivative channel (X = OMe) is conductive under asymmetric conditions whereas the cyano-derivative (X = CN), which

has no permanent dipole, is inactive under symmetric conditions. This suggests that a permanent molecular dipole is necessary to orient the channel before it can conduct ions.

Similar crown ether membrane spanning structures, which are termed hydraphile channels, by Gokel[23,44-46] have been investigated. The general structure of Gokel's family of compounds is shown in Figure 1-9. Gokel's recent work has focused on determining the location and orientation of the crowns with respect to the lipid bilayer. He uses fluorescence resonance energy transfer (FRET) to determine the location of covalently bound fluorescent tags with respect to specifically placed quencher molecules. Placement of a quencher group along various positions of the phospholipid tails gives an

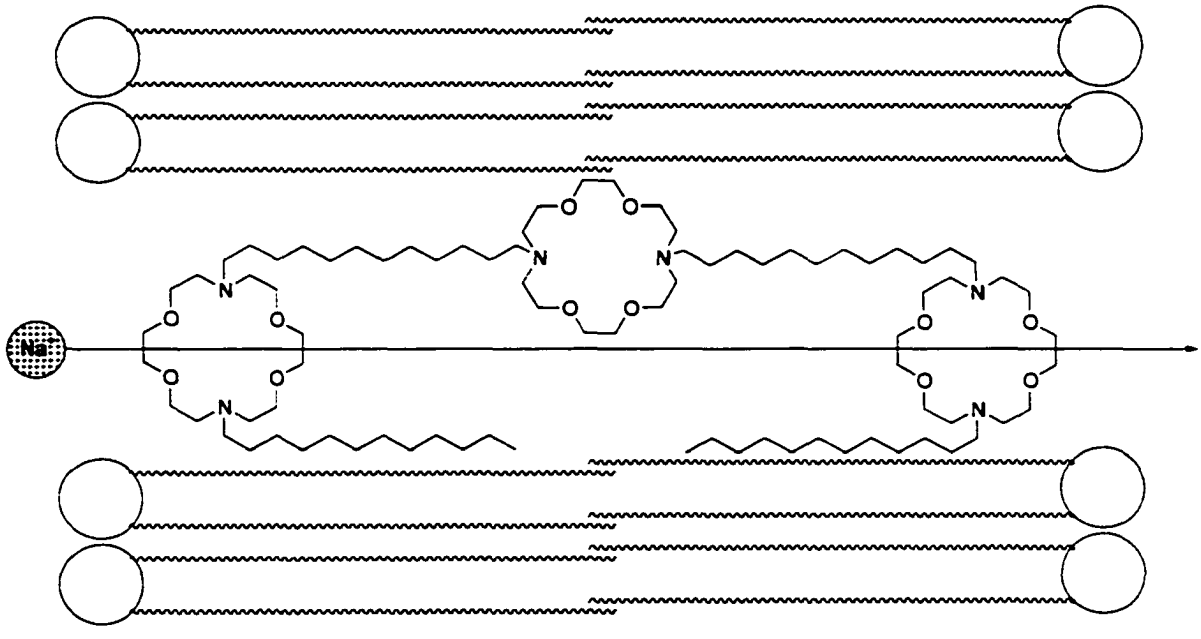

Figure 1-9. Schematic of a hydrphile channel in a bilayer.

indication of how deep a probe molecule penetrates the bilayer thus providing information about the location of the tag. The work is a good example of determining the structure of a system with so many degrees of freedom in a lipid environment. The problem of synthetic efficiency persists in the Gokel system, and as a result structural modifications do not deviate too far from the structure shown in Figure 1-9.

A more modular approach to ion-channel synthesis is needed that incorporates the ability to test the structural features deemed necessary as requirements for ion transport. The work done by the Fyles[24,47-49] group in the past has sacrificed efficiency for structural properties as the compounds were highly active channels. Macrocycles were believed to

be necessary for the activity and were assumed to affect ion selectivity. Macrocyclic components cannot lead to high-yielding reactions and are often plagued by solubility issues. In recent years, the motivation in the Fyles group has been to break from the synthetic constraints imposed by macrocycles and probe whether they are necessary for ion-transport. As a result, the following compounds in Figure 1-10 were synthesized.

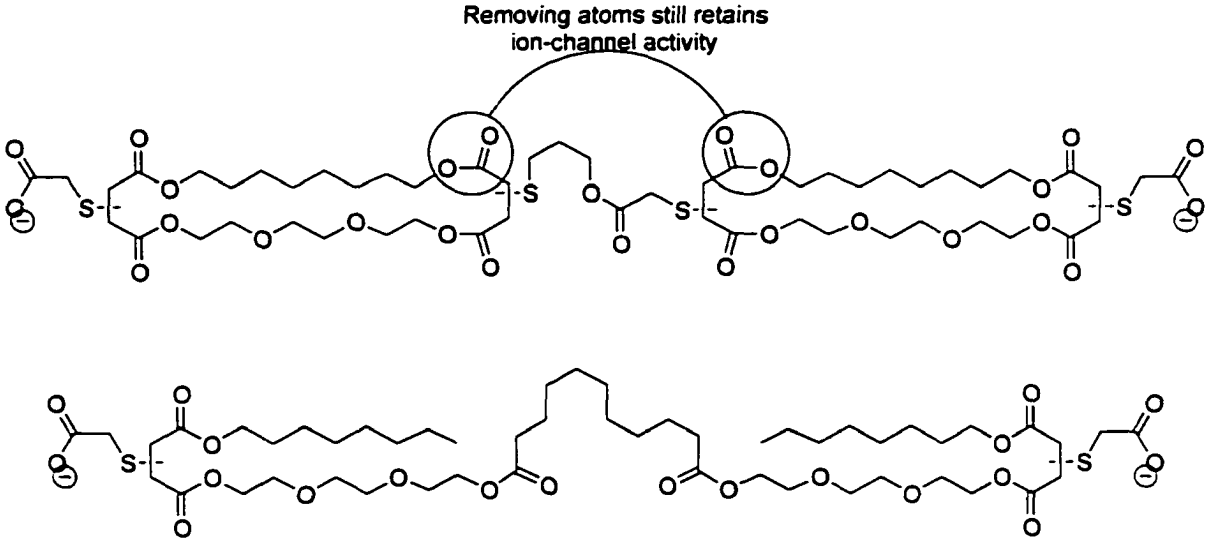

Figure 1-10. A bis-macrocyclic pore former and the acyclic compound derived from it.

To summarize the results, the acyclic compounds do form ion-channels, they are ion selective and their activity is not voltage-dependent. In essence, the acyclic compound is indistinguishable from the related bis-macrocycle. A major synthetic gain has been achieved by replacing the macrocycles with linear fragments containing the same functional groups from 0.1% yield[48] for the bis-macrocyle of Figure 1-10 to an unoptimized 50% yield for the acyclic compound. Kinetic data for the top compound indicates the active channel forming structure is a dimer. Whether the dimer is composed of two rod-like bilayer-spanning molecules or two U-shaped molecules spanning each leaflet is unknown. The acyclic compound is believed to operate in the same fashion, but kinetic data is not clear at this time. Nevertheless, a leakage assay of the acyclic compound has proven the linear analog is not a membrane-disrupting agent. The Fyles group has produced one bis-macrocyclic voltage-gated channel, (shown below in Figure 1-19), and its behaviour was attributed to its electrostatic asymmetry, as supported by Matile's findings described above. The synthesis of such asymmetric structures usually comes at the cost of overall efficiency. In recent work, a synthetic methodology has been

developed to synthesize channels in a non-symmetric, modular fashion using solid-supported synthesis[50]. Final products were just coming to fruition at the commencement of this writing but preliminary results look promising for a steady supply of channel compounds with relatively modest synthetic investment.

1.2 Ionic Signal Propagation in Nature

1.2.1 Neurons and Ion-channels

Ionic signal propagation in animals, such as the signaling to muscles or to other nerves, is accomplished by several biochemical structures working as a system in concert. In animals, including *homo sapiens*, a class of cells called neurons performs electric signal transduction. Within the class of mammalian neurons, there are three general sub-classes: multipolar interneurons, motor neurons and sensory neurons[5]. Multipolar neurons transmit signals between neurons and have heavily branched dendrites, which permit a large capacity for connectivity. Motor neurons conduct electrical pulses to muscle tissue. They have branched dendrites for multiple inputs but only one propagation pathway that is heavily insulated to stop signal dissipation. Sensory neurons are a direct insulated connection from receptor cells to multiple axon terminals. Neuron anatomy has the following general structure. The dendrites are at the origin of the signal propagation. An external event must trigger this part of the cell in order for the signal to be created. The signal, once created, is propagated through the axon to the terminus appropriately called the axon terminus. At junctions between the neurons lie the synapses. The synapse is the gap between neurons where neurotransmitters are released. These diffuse across the synapse to receptors on a following cell that allow the signal to continue[5].

The signal propagated is a wave of membrane depolarization called the action potential. The action potential arises from differences in concentrations of ions on either side of a lipid bilayer. The core of the signal propagation issue lies in the controlled permeability of the lipid bilayer to ions, which is in turn controlled by ion-channels in the membrane. The concentrations and locations of the ions in a cell at rest (not undergoing

signal propagation) are sketched in Figure 1-11. The ionic composition is kept in this

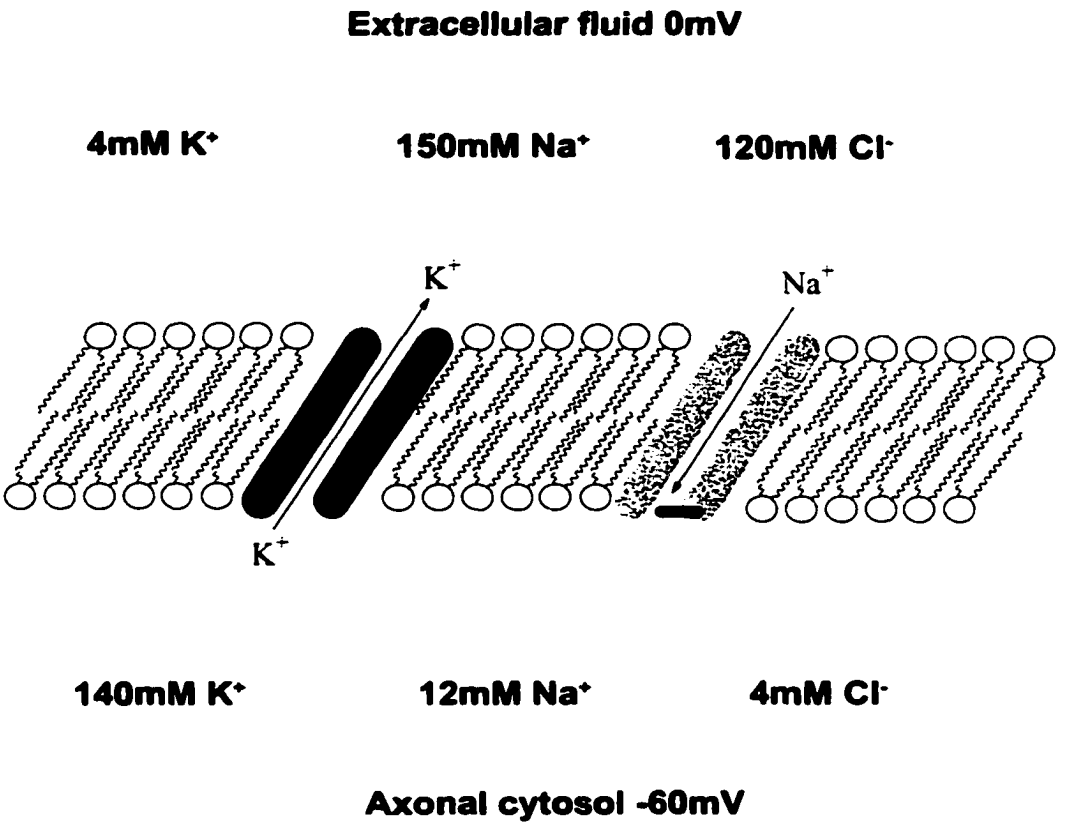

Figure 1-11. The origin of the resting potential in a neuron. The two channels represented are selective for each of the cations shown. The K^+ channel is always "on" whereas the Na^+ is gated.

state away from equilibrium by actively exchanging internal Na^+ for external K^+ with the expenditure of ATP.

The membrane of a neuron contains two types of channels, namely a Na^+ selective channel and a K^+ selective channel. The K^+ family of channels always exhibits a slight leakage of K+ ions and is thus mainly responsible for establishing the resting membrane potential. Under resting conditions the Na^+ channel is closed, thus the resting potential is established by the K^+ concentration gradient at approximately –60 mV. Note that the ionic flux always occurs down the chemical potential gradients of the individual ions enabling a much faster and larger response compared to actively generating a depolarization by ion pumps. The gate on the Na^+ channel is potential sensitive and has a unique current-voltage relationship that is critical in its use for action potential

generation. Several important characteristics[1] of an intact neuron can be seen from Figure 1-12.

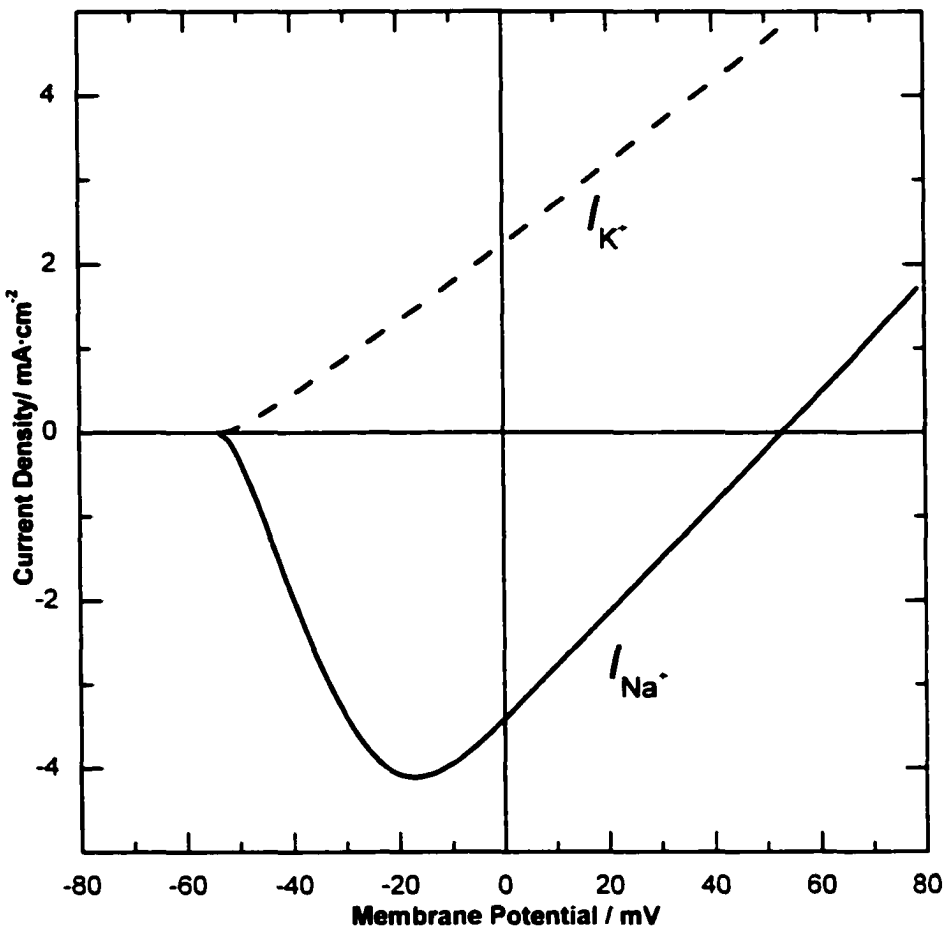

Figure 1-12. Current-potential relationship of a neuron.

A negative current, by definition with respect to cations, is the result of cations entering the cell. The I_{Na} line implies that at potential more positive than –50 mV, Na^+ ions begin to flood into the axonal cytosol and as potential is stepped more positive, the Na^+ ion flood ceases and it actually reverses its flow direction at potentials greater than +50 mV. At this point, a balance is struck between the Na^+ ions following the concentration gradient and the Na^+ ions following the electric field gradient resulting in no net flux at +50 mV. Neither channel is in the open state at potentials more negative than –50 mV. This potential is more positive than the resting potential of the neuron therefore little energy is needed to maintain the Na^+-K^+ concentration levels even while

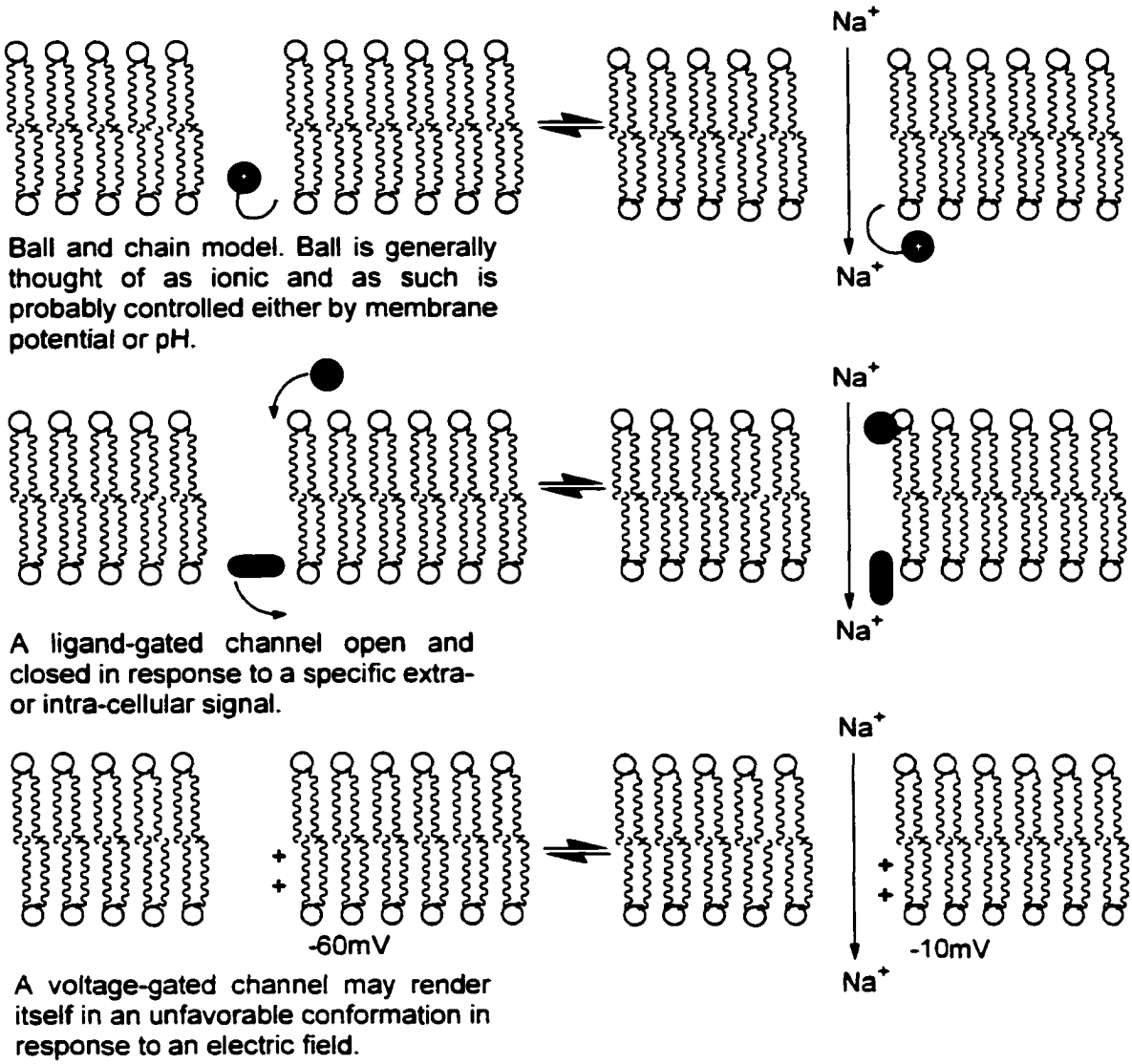

Figure 1-13. Schematic representation of ion-channel gating models.

the K^+ channels continually leak. The molecular details of exactly what causes the gating of the Na^+- and K^+-channels remain elusive. However there are several conceptual models[5] to explain the gating process, some of which are shown in Figure 1-13. All the presented models have three parts: a selectivity filter, a voltage sensor, and a physical gating mechanism. The selectivity filter is the part of the channel that discriminates between ions (Na^+ or K^+) and either allows passage of the ion through the water filled pore or not. Recent crystal structures of an ion channel[6-8] show an area of restriction where the specific ions are partially dehydrated and organized before they are flushed through the channel in an assembly-line fashion. In this channel, the selectivity of Na^+

over K^+ is a direct result of the physical dimensions of the pore. The voltage sensor in an ion-channel monitors its surrounding and acts alone, or communicates information to a gate structure. If the sensor acts alone then the channel consists of only two parts, where one plays the double role of sensor and gate. Little information is known regarding the sensing abilities of ion-channels. Sensors can respond to chemical, electrical or mechanical stimuli as indicated in Figure 1-13. The gate can be a physical plug that stops ion transport or it may be a conformational change in the ion-channel itself that renders it less effective to ion permeation[51].

1.2.2 Creation of an Action Potential

Placing Na^+- and K^+-channels in a lipid bilayer and setting the solutions as described in Figure 1-11 gives a resting potential of –60 mV^{-1} but no action potential: an initiator stimulus is needed. Membrane potential has a sign and magnitude comprising two components, ionic permeability and ionic composition. It is simpler to use a conductivity term to describe current flux, as the sign becomes irrelevant. Consider the permeability changes that would follow an electrical stimulus provided by an electrode current pulse towards a positive membrane potential. By definition, the application of the current pulse is considered time zero. Less than one millisecond after the stimulus the Na^+-channel gates open in response to the depolarization and the Na^+ rushes down its concentration gradient producing the upswing portion of the membrane potential[1] shown in Figure 1-14. The positive deflection in potential is caused by the Na^+ permeability increase as shown in Figure 1-14. This allows the Na^+ concentration gradient to dominate the overall membrane potential. The Na^+ conductance drops off markedly after one millisecond because a local equilibrium is established such that the Na^+ gates are still open but no net charge is flowing. Because of the increasingly positive potential, the K^+ channel gates are opened to allow a flood of K^+ ions, which restores the net negative polarity of the membrane. This closes both the K^+ channels and the Na^+ channels. At this point, the ion-channels are in a refractory period where they are unable to fire again until the Na^+ and K^+ concentrations are re-established. The original K^+ and Na^+ ion

concentrations are reestablished by Na^+- K^+-ion pumps with the consumption of ATP.

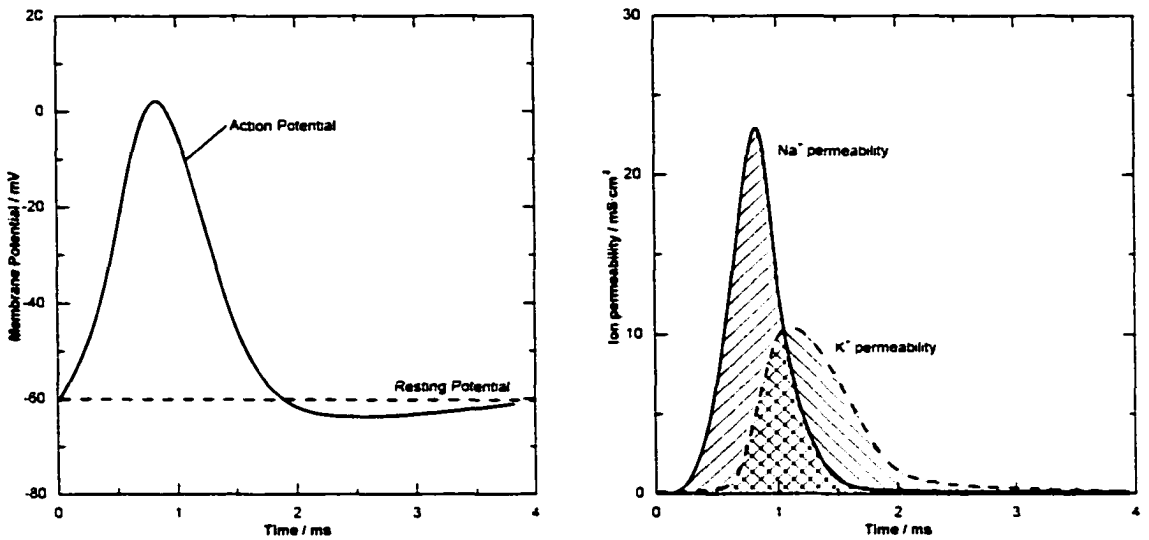

Figure 1-14. General shape of an action potential and Na^+ and K^+ permeability as a function of time during an action potential.

The changes in membrane potential are created by moving a very small percentage of the total Na^+ and K^+. The potential change is not generated from a change in the bulk concentration levels as this would cost too much energy and propagate too slowly. In fact, only one K^+ ion per 300 000 in the cytosol is exchanged for extracellular Na^+ to generate the membrane polarity reversal. The ATP-driven ion pump maintains the bulk concentrations but inhibitory studies have shown that without the pump the neuron can undergo thousands of action potentials before the bulk concentrations are equilibrated.

1.2.3 Propagation of Action Potential

The propagation of the action potential is accomplished by the radial passive diffusion of ions adjacent to the membrane. Consider an electrophysiology experiment[5] sketched in Figure 1-15.

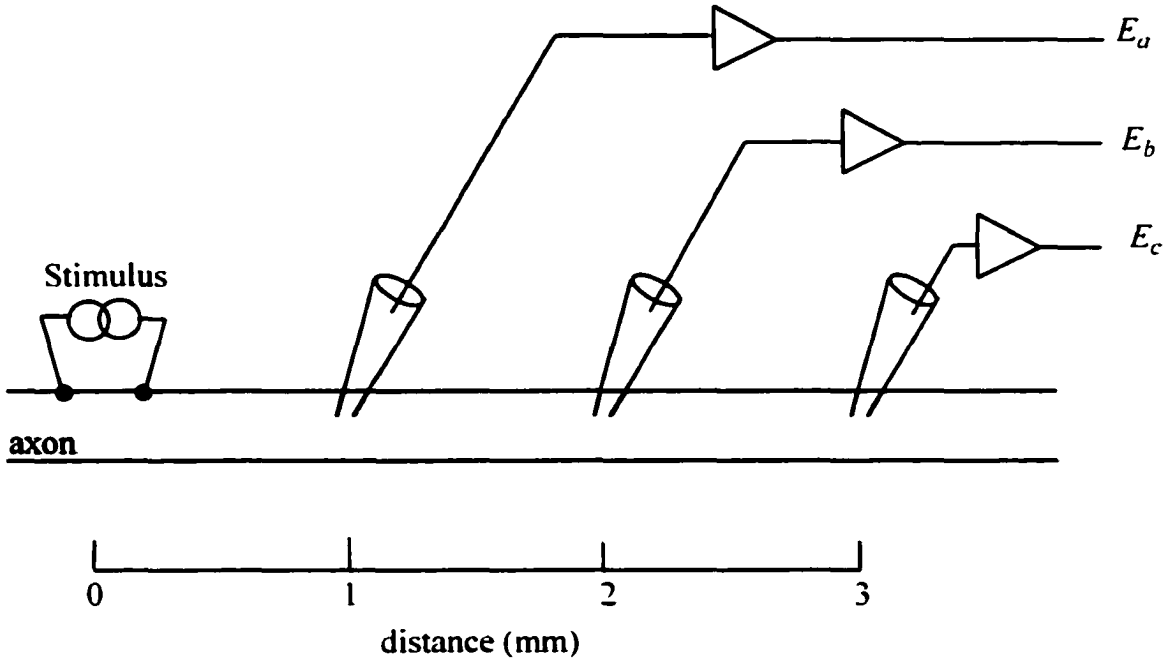

Figure 1-15. Electrode placement to record time-based signal propagation in an axon.

The axon is placed in an electrolyte bath attached to virtual ground and several microelectrodes are placed a set distance away from the current, or stimulus, source. Figure 1-16 outlines the observable events and their effects on membrane potential chronologically. Time zero of Figure 1-16 corresponds to the pulse recorded at E_a whose location is shown in Figure 1-15. Once the stimulus has depolarized the membrane, the Na^+-channels open and the potential reverses opening the K^+-channels. The potential peak reaches its maximum value one millisecond after stimulus, corresponding to the flood of Na^+ ions. At this moment, the membrane is in a depolarized state where the inside is positive relative to the outside. The ions that created this imbalance in charge begin to passively diffuse along the inner membrane surface inducing adjacent channels to begin their depolarization events. The ability of the Na^+-channel to be closed and inactivated for a short period ensures unidirectional signal propagation since the depolarization due to excess Na^+ that is passively spread from the open channel site would be just as likely to propagate in both directions. At the original site of depolarization the Na^+ conductance is arrested and the K^+ permeability is increasing resulting in the pulse returning to the resting potential.

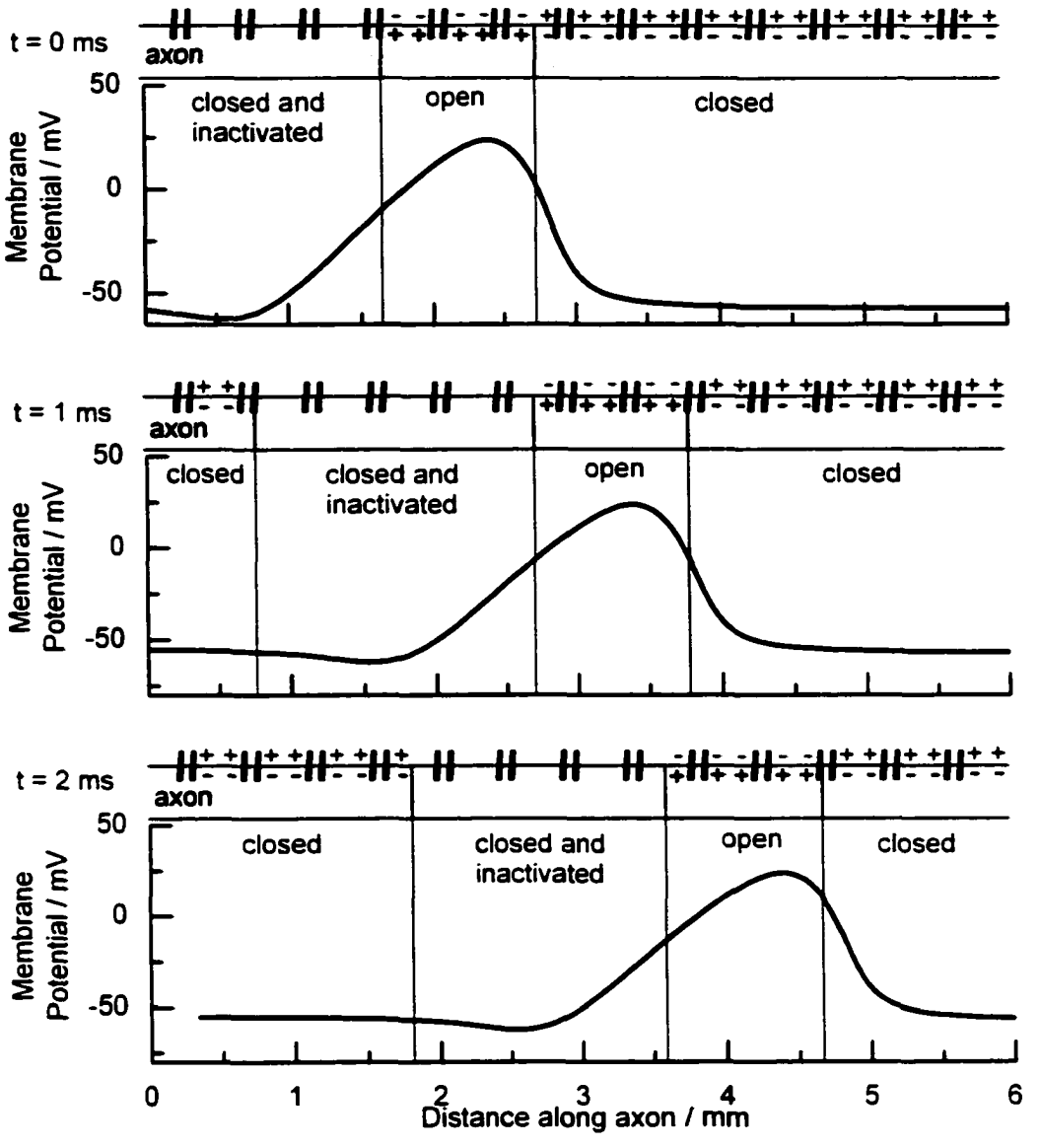

Figure 1-16. The time course of events during signal propagation. The positive and negative signs on opposing sides of the axon membrane represent the potential at the specific time periods of signal propagation. The vertical bars represent the membrane-bound voltage-gated ion-channels.

Experiments have established that the Na^+ channels are not only closed at this point but also temporarily inactivated. This implies that the Na^+ channel actually contains two gating devices; one closes it at negative potentials and another closes it at positive potentials. The continuation of the pulse along the axon is sustained by the same depolarization-repolarization mechanism and passive diffusion along the membrane surface. This mode of signal propagation allows an electric signal to propagate without a

decrease in signal intensity. In fact, the signal is propagated with the same signal intensity at all points because it is a threshold-based firing system. A low flow of Na^+ ions through the open ion channels would result in the near neighbour channels not experiencing enough of a depolarization to open and the signal would terminate. Above the threshold, however, the signal propagates with no attenuation at each point. The propagation of an ionic signal is an all-or-nothing mechanism under control of passively diffusing Na^+.

An additional feature is critical in myelinated axon signal propagation, shown in Figure 1-17. Myelination increases the velocity[4] of signal propagation to about 100 $m \cdot s^{-1}$ as compared to unmyelinated axons, along which the signal travels at speeds of about one $m \cdot s^{-1}$. Myelin is a specialized membrane sheet that coils itself around axons in a structure known as the myelin sheath. Each region of myelin is separated from the next by a small section of bare axon termed the node of Ranvier that is exposed to the extracellular fluid.

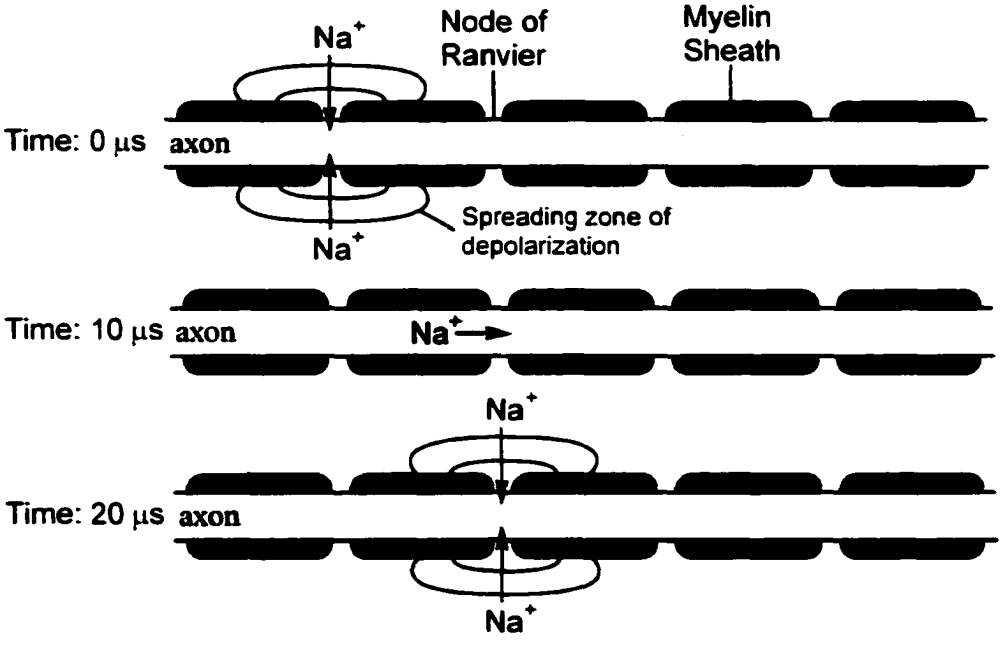

Figure 1-17. Myelination of axons and the nodes of Ranvier.

The myelin sheath, which coils around the axon 50-100 times, produces an insulating layer preventing the transfer of ions through the axon membrane thus forcing all electric activity to occur at the nodes of Ranvier. The local concentration of ion-channels at the nodes is much higher compared to unmyelinated neurons, thus enabling a larger zone of depolarization. The distance dependence of depolarization magnitude is illustrated in

Figure 1-18. Clearly shown is the great effect the myelination has on the distance the signal is propagated. The unmyelinated neuron requires restimulation, or more ion-channels opening to propagate the signal, every 0.5 mm. In contrast, the myelinated neuron only requires a new set of ion-channel openings every 2 mm. Nodes of Ranvier have been found in some vertebrates to be as far as 5 mm apart[5].

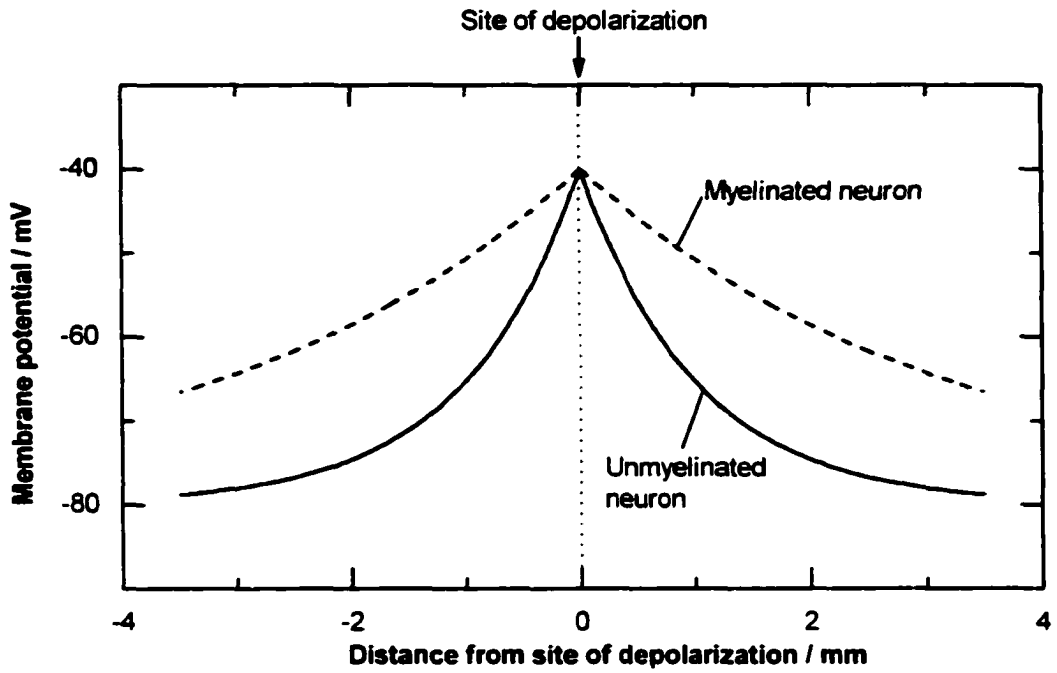

Figure 1-18. The size of the depolarization zone depends on the degree of myelination.

1.3 Requirements for Mimicking Signal Propagation

Using nature as a model of ionic signal conduction, this section focusses on how to reduce the natural system to the essential components necessary to achieve signal propagation in a synthetic system.

1.3.1 Functional Aspects: Na^+ and K^+ Channels

Two channels with complementary selectivity are needed. The more difficult component of a signal propagation system is the Na^+-channel. As discussed above, the biological Na^+-channel has three features that lend itself to propagating signals: it is Na^+

ion selective, it turns itself off at negative potentials and it has an additional blocking mechanism that renders it inactive after a short period of ion transport. The latter behaviour, which renders the channel inoperable during the refractory periods, is an adaptation to transmit an action potential unidirectionally. This requirement, although found in nature, is not strictly necessary at the rudimentary signal propagation level because a radially propagating signal would be equally as functional.

Ion selectivity is required to maintain an ionically imposed resting potential difference across the membrane. Much research during the eighties was focussed on cation recognition in the area of supramolecular systems[52]. Applications and extensions from those findings have resulted in several synthetic ion-transporters that have selective cation permeability[53-59]. The goal is to employ strategies that allow binding of one ion over another, but the association constants cannot be too large otherwise the ion will remain bound inside the channel instead of flowing through. Finding middle ground between selectivity and ion-transport rate has been the focus of Fyles research for the last decade.

The ideal models to follow are those in nature where the selectivity is an artifact of the pore size. Natural channels are believed to act by dehydrating the ion and passing the ion through a water filled pore to the other side of the membrane. This provides both a steric barrier and an energetic barrier to ion transport. The channels synthesized in the Fyles group have generally had the selectivity trend of $Cs^+ > K^+ > Na^+$, which implies the hole is not size selective but rather dependent on energies of dehydration. However, in a synthetic signal propagation system, the conditions do not have to be the same as in biology. Pairs of cations other than K^+ and Na^+ would be permitted. The goal is to produce a pair of channels that are complementarily selective to one cation in the presence of the other. To model the biological system more accurately, each channel also needs to differ in conductivity. That is, the channel selective for ion one (Na^+) must have a higher specific conductance than the other channel has for ion two (K^+). This enables the large conductance channel to open causing a rapid depolarized state and permits equilibrium to be established quickly. This is necessary because a time delay is required for the opposing channels to open; otherwise, the channels would simply flood ions back and forth too quickly causing no net change in membrane potential until concentration

equilibrium is established.

At least one of the two channels must have voltage dependent conductivity, however, very few synthetic ion-channels have voltage dependent properties. Fortunately, the Fyles group has synthesized a family of compounds that have the ability to turn off ion permeability at positive potentials. An ideal artificial ion-channel would have a current-voltage relationship of the Na^+ channel curve shown in Figure 1-12. The compound that produces a similar I-V profile to the K^+ channel curve of Figure 1-12 is shown in Figure 1-19. The synthesis and mechanistic details of the ion-channel can be found in Zhou's[60] and Looke's[61] dissertations. The compound has now become a model to build on. The main difference between this compound and the other synthetic channels that do not show voltage-gated properties is the lack of centro-symmetry. A possible origin of a channel possessing voltage-gated property lies in the orientation of an inherent molecular dipole with respect to membrane potential. A channel that is symmetrical about its centre can have no net dipole moment. The dipole of the

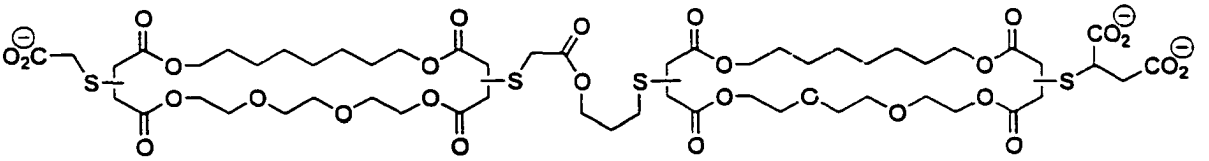

Figure 1-19. Structure of an artificial voltage-gated ion-channel.

compound shown in Figure 1-19 is due to its dianionic charge at one end and monoanionic charge at the other. In this molecule the charged head groups are necessary to orient the channel into a conducting state in the bilayer. The charged groups try to be in the aqueous environment whereas the hydrophobic, inner macrocycles tend to partition to the lipid portion of the bilayer creating an orientation favorable for ion conduction. The use of a permanent dipole is deemed a critical feature to creating new voltage-gated channels. The channels shown in Figure 1-20 orient themselves at negative potentials resulting in ion channel formation and when stepped to more positive potentials disorder prevails resulting in little ion-conduction.

On a practical side, the above compound poses significant synthetic challenges. The amount of labour is too high, overall yield is poor and cost of materials is too great to continue pursuing macrocyclic systems such as this. The pursuit of non-macrocyclic ion-

channels has resulted[49] in a more facile, and easily tunable system to systematically study ion-channels. The new synthetic methodology is also innately unsymmetrical because it is done on solid supports. The synthesis of ion channels is not directly a focus of this thesis, but it is pursued by others in the research group. I assume that channels with suitable functionality will soon be available from synthesis.

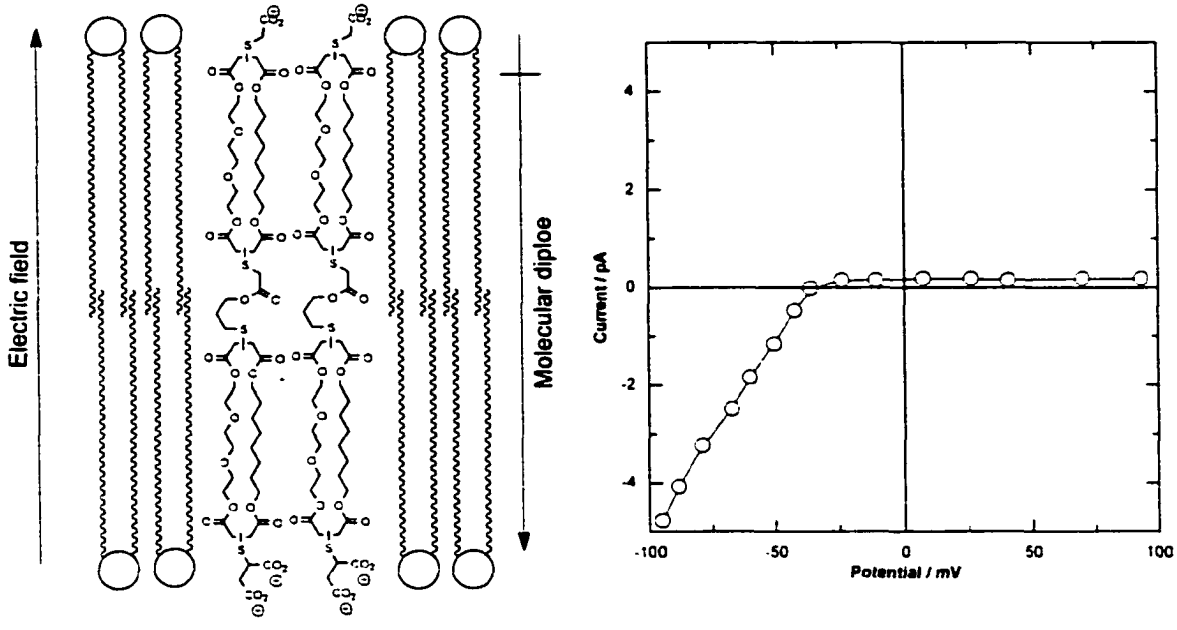

Figure 1-20. Schematic representation of rectification manifested by a permanent molecular dipole placed in an electric field.

To summarize: the functional requirements of the two channels are paramount to ionic signal transmission. For the voltage-gated channel, the shape of the I-V relationship should be similar to either curve of Figure 1-12. It would be possible to produce signal propagation in a system where the I-V relationship of the two channels is virtually identical as will be explained in the next section. In addition, complementary ion-selectivity is necessary to maintain the resting potential. Finally, the conductance of the first open channels must be larger than the second open channels to allow a time lag to occur.

1.3.2 Physical Requirements of Signal Propagation System

Biology has a tremendous architectural framework to place proteins in various locations. For example, a cell is able to place an ion-channel in a membrane and ensure

that all channels have the correct orientation. None are permitted to undergo a flip-flop thus reversing their action potentials. This inversion of an ion-channel would be catastrophic because the action potential would be in a continual "on" state and only until a depolarization event occurred would the channel close. In a model laboratory system, such fine molecular control over channel inversion is not yet possible since the common method to insert channels into a bilayer is by injection of channel compound adjacent to the bilayer. Often this results in bilayer destruction. Once the bilayer has ruptured, all asymmetry is lost; thus, all voltage-gated properties are gone.

A more sophisticated insertion method for ion-channel insertion is required. Not only must the insertion occur to preserve bilayer integrity and channel orientation, it must also control the amount of material inserted. This means that only a few molecules will be inserted. A solution to this issue, explored in this thesis, resides in the properties of an Au-S bond. Thiols spontaneously adsorb to Au surfaces producing a covalent linkage with bond strength[62] of 45 kcal·mol^{-1}. Subsequent electrochemical reduction can release the bound species, presumably the thiolate. This sequence suggests that one could place a thiol-modified ion-channel onto a gold microelectrode, place the electrode next to a planar bilayer, and release the ion-channel electrochemically. This system would solve many of the problems associated with the injection method. First, the injection method is extremely wasteful of compound. A typical experiment injects between 10^{10} and 10^{12} molecules and yet only records the activity of 10 or so of those molecules. The use of an electrode in replacement of the syringe would potentially allow a much greater control of the amount of material injected and the location of the injection.

From an electrochemical point of view, the adsorption[63-79] and reduction[80-99] processes have been extensively studied in the literature. However, no work has been done regarding the identification of the organic fragment resulting from the cleavage. Chapters 3 and 4 describe the experiments that led to the identification and quantification of an organic fragment released from an Au surface by means of fluorescence HPLC. The use of Au as a support for ion-channels also has some obvious limitations because very few ion-channels contain sulfur. Thiol adsorption is also a spontaneous process, so newly cleaved channels may simply re-adsorb.

Conventional methods of ion-channel insertion rely on a fast volume injection in hopes of disrupting the bilayer system just enough to incorporate an ion-channel. The electrochemical method is a potentially gentler and more precise technique to achieve ion-channel insertion. Figure 1-21 demonstrates the positioning of the Au electrode modified with thiol-linked ion-channels. The *cis* and *trans* notation refer to two sides of the bilayer chambers with the *cis* side usually the side of channel injection and the *trans* side at virtual ground. The pictorial representation of the bilayer and channel compounds is grossly out of scale. The actual dimension of bilayer thickness is 40-60 Å and the channel compounds usually are at least the length of the bilayer. The surface area of the

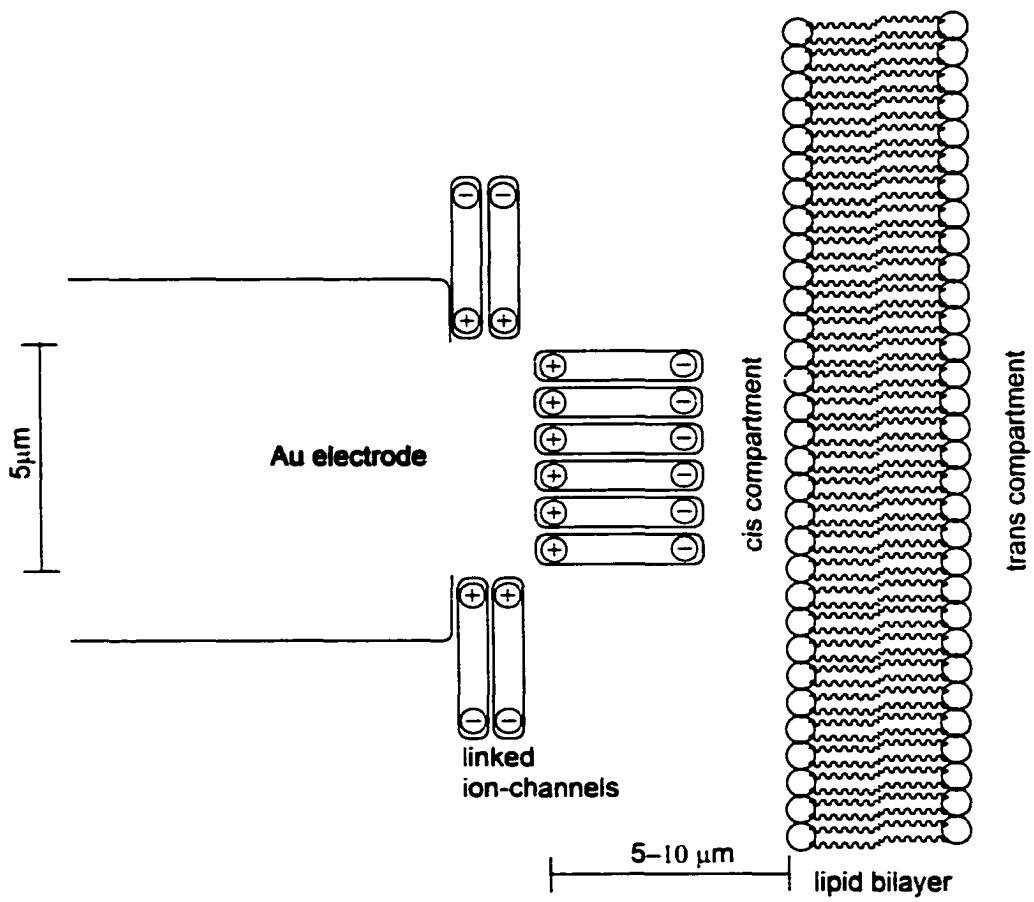

Figure 1-21. Concept sketch of a method to inject ion-channels into one face of a lipid bilayer.

freestanding bilayer is usually about .02 mm^2 and the area of the gold microelectrode is 8×10^{-5} mm^2. The area of the gold electrode will limit the dosing of the channel. The theoretical limit for packing of an ion-channel on the Au surface is not known since it is unknown how the channel will position on the Au surface (i.e. vertical columns as shown

or lying flat). The orientations of the molecules are needed before predictions regarding the amount of material can be made. The loading of ion-channels onto an Au surface could be done quantitatively by electrochemistry by binary system adsorption[79], the deposition of ion channels is accompanied by another inactive (mercapto-hexadecane) thiol in much greater concentration than the ion-channel. The resulting monolayer from a binary system will provide a monolayer-protected surface that is sparsely populated with covalently bound ion-channels. As a result, concentrations of ion-channels can be greatly reduced to the point where controlled-release of tens to hundreds of molecules could in principle be achieved. Several studies[68,71-73,80,84,100] have shown reproducible and predictable quantities of adsorbing species. The released channel will diffuse, with the help of an electric field, to the lipid bilayer and partition itself into the bilayer in an asymmetric fashion.

1.4 Goals of Thesis

The thesis is organized in a component-by-component approach such that each chapter will be an independent aspect of a system required to propagate ionic signals. The first section deals with the gold thiol chemistry and electrochemistry. This has a direct effect on creating the asymmetric distribution of channels within the bilayer, which is necessary for propagation of action potentials. It answers the questions regarding how much material will be dosed. Can the dose be controlled by some means? Was the compound altered in the cleavage process? Included in this section will be some instrumentation details, particularly in reference to recording fast events. The next part of the thesis involves testing ion-channels for properties such as ion selectivity, conductance, current-voltage relationships and survivability statistics. These tools enable the identification and analyses of single-molecule activity. This data is required because many supramolecular properties of the target ion-channels are needed before a study involving several ion-channels working in concert can be undertaken. The culmination of these two parts into the actual physical transfer of ion-channels comes as the last section. This section describes the spatial and temporal control by placing the natural ion-channel, gramicidin into a lipid bilayer without syringes. The final section of the

thesis will project the types of devices and experiments required to complete the challenge of ionic signal propagation in an artificial system.

Chapter 2 Synthesis and Characterisation of a Fluorescent Thiol

2.1 Requirements for Analytical and Electrochemical analysis

The purpose of this section is to document and design the synthesis of a compound that is suitable for electrochemical analysis and is easily detectable at trace concentrations. The detection limit requirements can be calculated from the theoretical surface coverage on monocrystalline gold surfaces using 10^{14} molecules·cm^{-2} as a model[62] of total surface coverage. Assume an electrochemical cell with an Au electrode area of 1.5 cm^2, releasing all of its bound thiol into 1.0 mL of solution. This yields a concentration of 10^{-7} M. Electrospray mass spectrometry was explored as the detection system with 11-mercaptoundecanoic acid as the probe molecule. The synthesis and characterisation are not included because it is now a commercially available compound. However, the presence of molar quantities of electrolyte is not compatible with the electrospray technique and this approach was abandoned. Another technique that will allow identification of a compound and lies within the detection limits imposed by the electrode area, is liquid chromatography in conjunction with fluorescence detection. Liquid chromatography is more capable of handling samples with high salt concentrations than mass spectrometry.

The target compound(s) needed to fulfill three criteria: synthetically feasible, electrochemically inert and fluorescent. A linear saturated group placed between the attaching thiol and the fluorescent label can achieve electrochemical inertness. An undecyl chain was chosen because literature[101-104] has shown a minimum nine carbon spacer group is necessary to act as an insulator. The requirements of the fluorescent label were that it must have detection limits of at least 10^{-8} M and small enough such that it can pack tightly into a surface monolayer. Biphenyl or 2-naphthyl were the fluorescent labels chosen which fit these criteria. Coupling of a fluorescent marker to an alkyl thiol can be done through ester or ether functionalities. Only the ether synthesis was pursued because the carbonyl group adjacent to fluorescent group of the esters would add a non-radiative decay pathway thus reducing fluorescent quantum yields.

2.2 Probe synthesis and Liquid Chromatography (LC) Analysis

The synthesis outlined in Scheme 2-1 was carried out. The synthesis of all compounds was a straightforward process with procedures for all steps available from the literature for similar compounds.

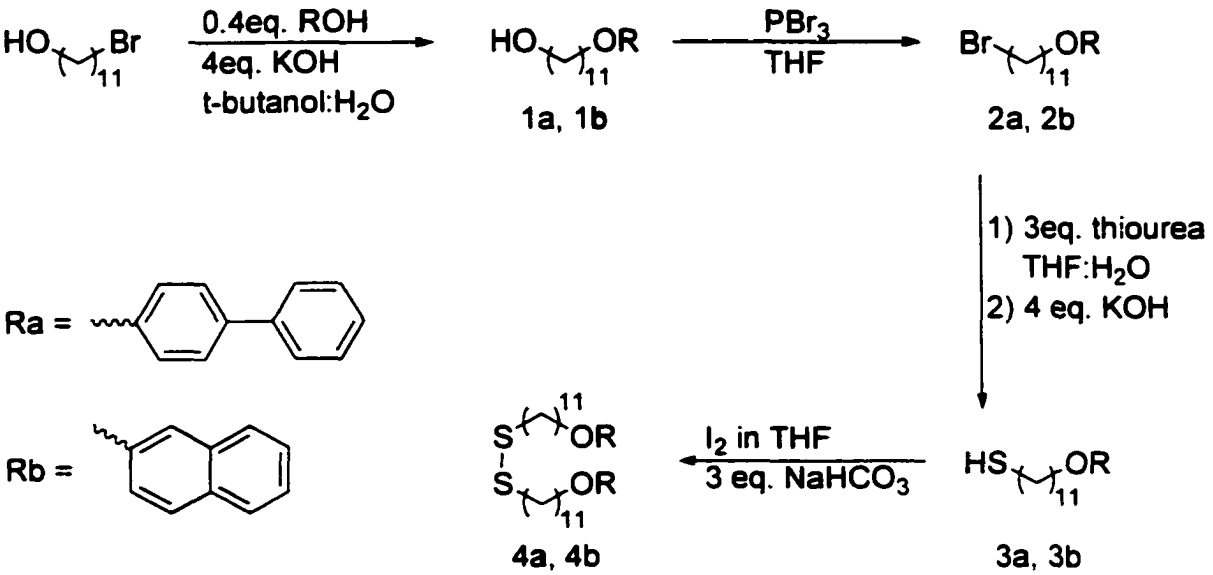

Scheme 2-1. Synthesis of target compounds 3a, 3b, 4a and 4b.

The synthesis of **1a** and **1b** follows a Williamson ether synthesis with modified solvent system[105] where the phenol in the presence of base acts as the nucleophile to displace the bromide. The second step yielding **2a** and **2b** involves the bromination of a primary alcohol via slow addition of phosphorous tribromide. The synthesis of **3a** and **3b** was a two-step process where the primary alkyl bromide is displaced by thiourea to produce the isothiouronium salt. Although the salt could be isolated at this point, it was not, and KOH was added directly to hydrolyse the isothiuronium to produce urea and the thiolate where subsequent acidification gave **3a** or **3b**. The final step involves the oxidation[106] of the thiol to the disulfide by slow titration with iodine in the presence of base, which gave **4a** and **4b**. The most common oxidant used to form disulfides is H_2O_2 but in this situation, the crude products, analysed ^{1}H-NMR, of the hydrogen peroxide reaction generally appeared to be over-oxidized. No attempts were made to identify or

isolate these over-oxidation products. Although iodine is a weaker oxidizing agent than H_2O_2, rapid addition of excess I_2 also produces the over-oxidation products.

The basic synthetic transformations were most easily followed by the characteristic ^{1}H-NMR chemical shift of the α- and ω- methylene protons of the undecyl chain as shown in Table 2-1. All products were fully characterized.

Table 2-1. ^{1}H-NMR chemical shifts of α and ω methylene protons of undecyl chain ($XCH_2(CH_2)_9CH_2Y$)

Compound	X	Y[†]	Multiplicity[‡]	δ(CH_2X) (ppm)	δ(CH_2Y) (ppm)
1a	OH	ORa	t	3.62	3.98
1b	OH	ORb	t	3.62	4.06
2a	Br	ORa	t	3.40	3.99
2b	Br	ORb	t	3.41	4.07
3a	SH	ORa	t	2.51	4.00
3b	SH	ORb	q	2.51	4.06
4a	S-S	ORa	t	2.67	3.98
4b	S-S	ORb	t	2.68	4.06

[†]Ra = biphenyl, Rb = naphthyl; [‡] t = triplet, q = quartet

The chromatograms of **3a** and **4a**, shown in Figure 2-1, clearly demonstrate discrimination between compounds under the operating conditions of the HPLC. The

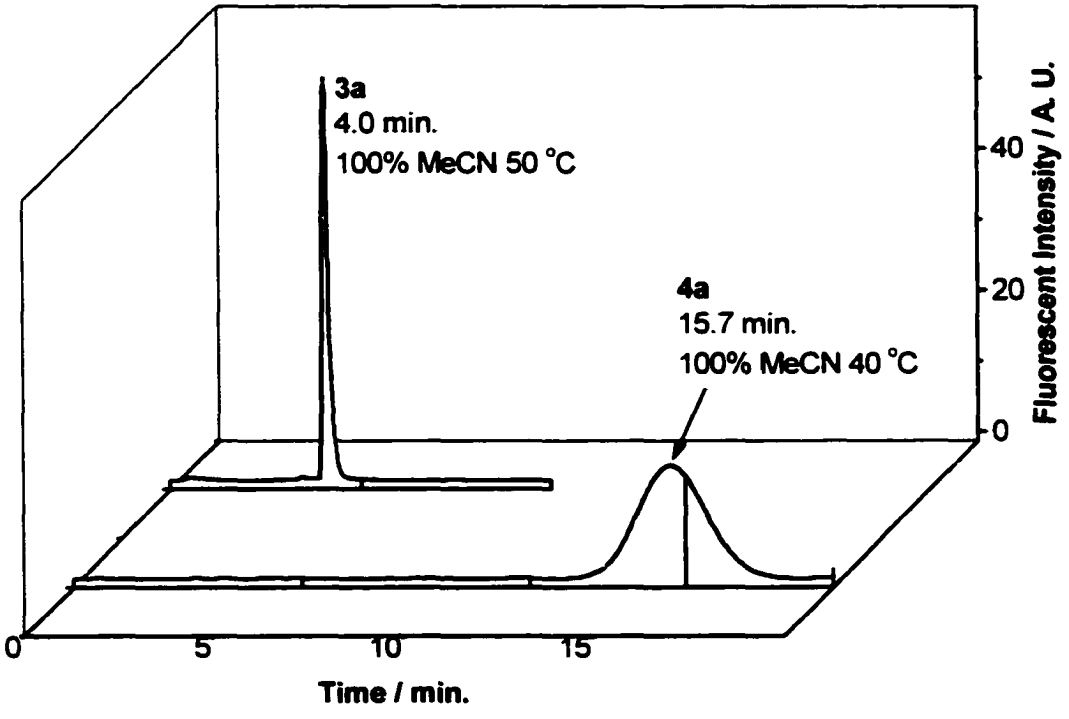

Figure 2-1. Retention times of 3a and 4a at different temperatures in 100% MeCN monitored at 330nm.

HPLC analysis was done to determine the detection limits of **3a** and **4a** and produce a calibration curve of detector response. Figure 2-2, shows absorption and emission spectra of **3a** as it was eluted from the HPLC. In addition, it demonstrates the fluorescent capability of **3a** to produce a large detector response at micromolar concentrations. The detection limit of the instrument, shown in Figure 2-3 and Figure 2-4, was assessed by serial dilutions of standard concentrations until no discernible peaks could be seen. The

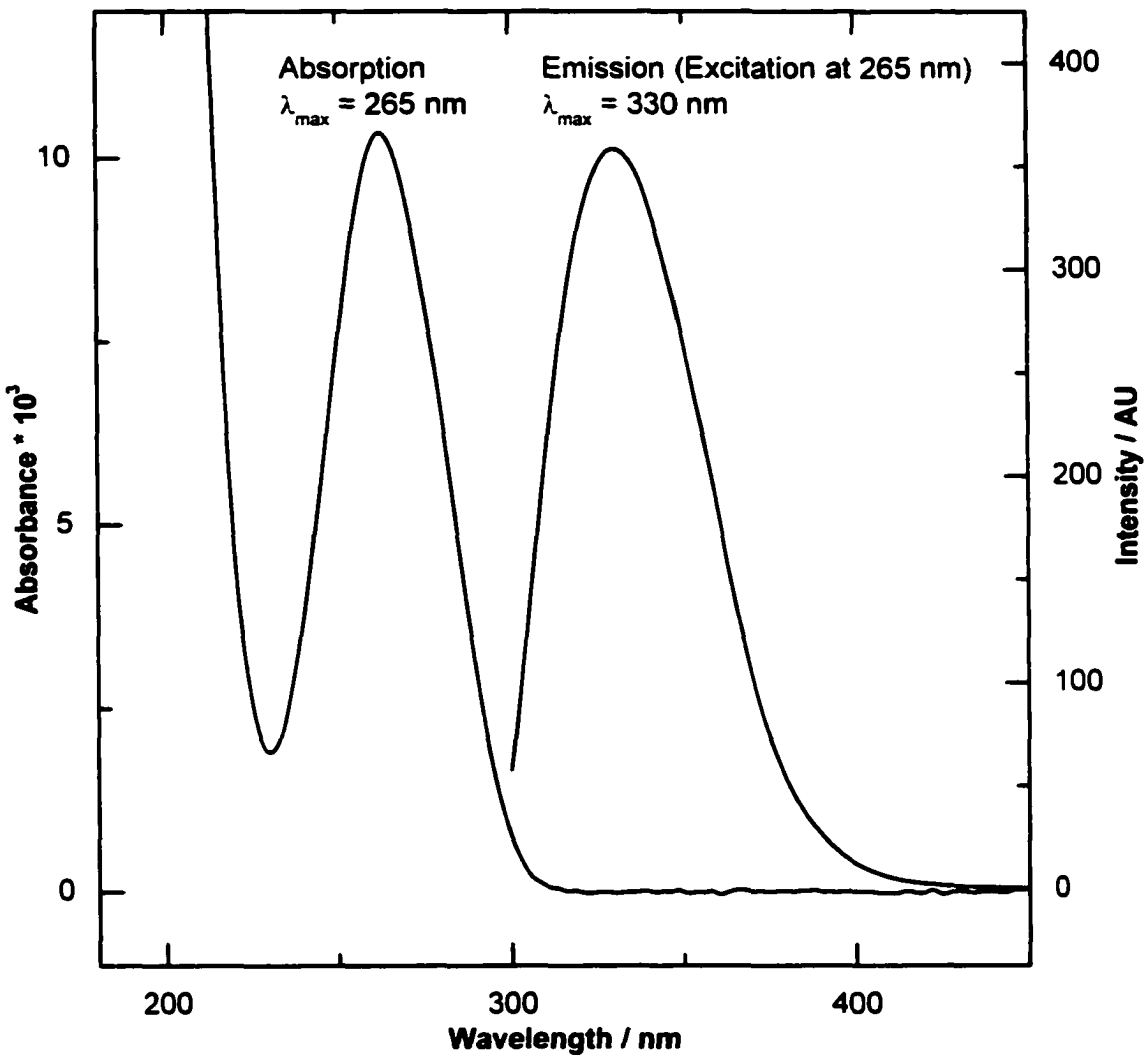

Figure 2-2. Absorbance and emission spectra of 7.29 μM solution of 3a in MeCN.

detection limit of **3a** was found to be one half the limit of **4a**. This implies the dimerisation of **3a** has neither a detrimental nor an enhancing effect on the total fluorescence intensity. The results show a detection limit of about 10^{-9} M for **3a** with a

linear detector response over six orders of magnitude. These results are promising for the use of **3a** and **4a** as candidate release and capture agents, as the analytical requirements of the design were achieved.

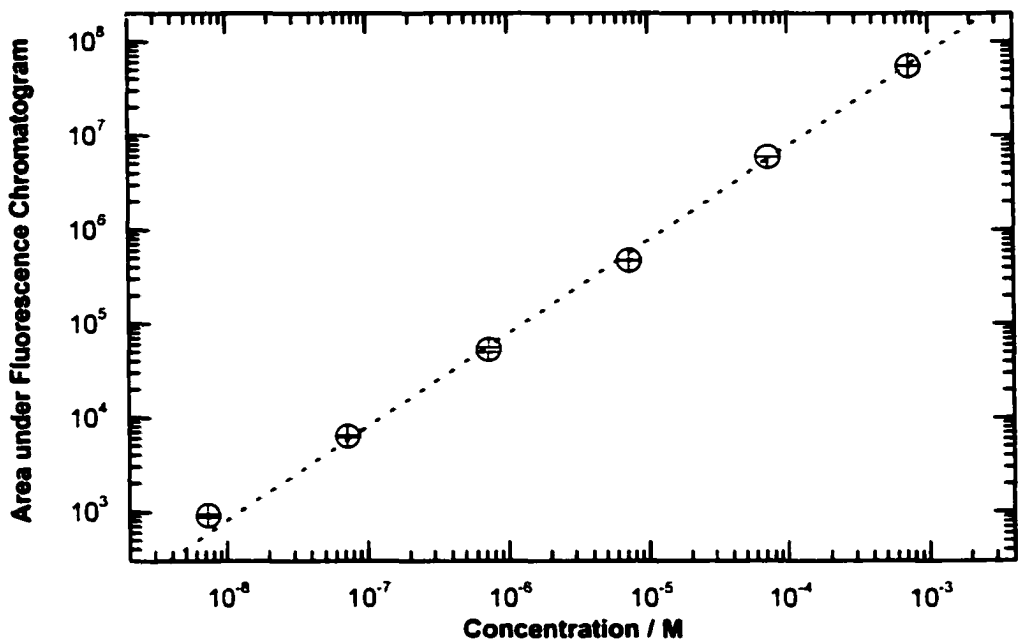

Figure 2-3 Log-log plot of HPLC fluorescent detector response to varying concentrations of 3a.

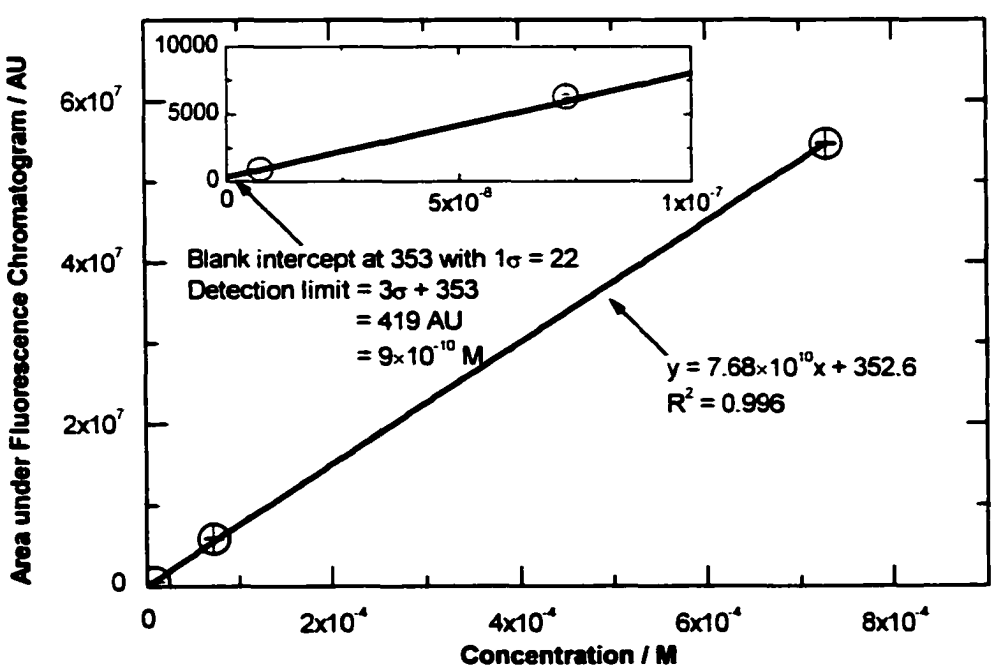

Figure 2-4. Detection limit calculation.

2.3 Experimental

2.3.1 Synthesis

Proton NMR were recorded with a Bruker AC300 (300 MHz) in $CDCl_3$ where all spectra were referenced to the solvent line (δ 7.24 ppm for $CDCl_3$ relative to TMS). Carbon NMR were recorded with Bruker AC300 (75.47 MHz) in $CDCl_3$ referenced to the central solvent line (δ 77.0 ppm relative to TMS). The spin multiplicities are reported as follows: s, singlet; d, doublet; t, triplet; q, quartet; qn, quintet. EI-HRMS spectra were recorded with a Kratos Concept-H instrument. Melting points were taken with a Reichert hotstage microscope. TLC was carried out using Eastman Kodak silica gel on polyester sheets with fluorescent indicator. All solvents were used as purchased through Aldrich. Solutions of organic solvents were dried with Na_2SO_4 and then concentrated using a rotary evaporator under reduced pressure.

General Procedure for Phenolic Ether Synthesis

To a suspension of KOH (4 eq.) in 25:3 (tert-butyl alcohol:H_2O) (250 mL for 10.0 g of compound), 11-bromo undecan-1-ol (2.5 eq.) and the phenol (1 eq.) were added and refluxed for 3 hours. The crude cooled slurry was filtered and the residue was dissolved in $CHCl_3$ which was then washed with water (3 × 50 mL), dried over Na_2SO_4, and solvent removed under reduced pressure yielding a white solid.

General Procedure for Primary Alcohol Bromination

To a solution of primary alcohol (1 eq) in THF (50 mL, 50 °C for 8 g of compound) PBr_3 (3 eq.) was slowly added over 10 minutes. After 50 more minutes of refluxing the solution was brought to room temperature where water was added to quench excess PBr_3. The solution was extracted with CH_2Cl_2 (3 × 20 mL) and the combined organics were dried over Na_2SO_4. Removal of solvent under reduced pressure produced a yellow solid. The yellow solid was washed with warm pentane to yield a white solid.

General Procedure for thiol formation via thiourea

The primary alkyl bromide (1 eq.) was combined with thiourea (3 eq.) in a 9:1 mixture of THF:H_2O (100 mL, for 3 g of compound) and refluxed for 48 hours. The mixture was cooled and KOH (4 eq.) was added and the reflux continued for another 8 hours. The mixture was cooled then acidified with 1.0 M HCl until pH 2, then extracted with CH_2Cl_2 (3 × 20 mL). The combined organics were dried over Na_2SO_4 and the solvent was removed under reduced pressure producing a white solid. Note: sometimes this procedure produced a mixture of thiol and disulfide.

General Procedure for thiol formation via disulfide reduction

Disulfide (1 eq.) was dissolved in THF (7 mL for 100 mg of compound) and Zn (10 eq.) and HCl (30 eq.) was added. The mixture was refluxed for 16 hours, cooled, then extracted with CH_2Cl_2 (3 × 10 mL). The combined organics were washed with 10 mL of 10% $NaHCO_3$ then H_2O (2 × 10 mL), dried over Na_2SO_4 then the solvent was removed under reduced pressure producing a white solid. The solid was dissolved in a minimum amount of hot 95% EtOH and slowly cooled. The solid product was filtered and rinsed with cold EtOH to yield a white powder.

General Procedure for disulfide formation via thiol oxidation

A saturated solution of I_2 (3 g) in THF (10 mL) was added dropwise to the thiol (1 eq.) dissolved in THF (5 mL, 50 °C for 110 mg of compound) containing $NaHCO_3$ (3 eq.) until a yellow color persisted for 30 minutes. THF was removed under reduced pressure, H_2O (10 mL) was added and the solution was extracted with CH_2Cl_2 (3 × 10 mL). The combined organics were dried over Na_2SO_4, CH_2Cl_2 was removed under reduced pressure producing a yellow solid. The crude product was dissolved in a minimum amount of hot 100% EtOH that was then slowly brought to room temperature producing a white precipitate. The residue was filtered and washed with cold 100% EtOH to give the final product.

(1a) 11-(1,1'-biphenyl-4-yloxy)-1-undecanol

The general procedure for phenolic ether synthesis was followed based on the following amounts: 11-Bromo-undecan-1-ol (10.0 g, 40mmol) and biphenyl-4-ol (17.02 g, 100 mmol, 2.5 eq.)and KOH (9.0 g, 160 mmol, 4 eq.) Yield: 9.25 g, 68%.

^{1}H NMR 300 MHz ($CDCl_3$): δ = 7.54 (m, 4H), 7.40 (t, 7.4Hz, 2H), 7.28 (t, 7.4 Hz, 1H), 6.95 (m, 2H), 3.98 (t, 5.9Hz, 2H), 3.62 (t, 6.6Hz, 2H), 1.79 (qn, 7.4Hz, 2H), 1.4 (m, 17H).

^{13}C NMR 75.47 MHz ($CDCl_3$): δ = 158.7, 140.9, 133.5, 128.7, 128.1, 126.7, 126.6, 114.8, 68.1, 63.1, 32.8, 29.6, 29.6, 29.5, 29.4, 29.4, 29.3, 26.1, 25.7.

EI Exact Mass: calculated for $C_{23}H_{32}O_2$: 340.2402, Found: 340.2402.

(1b) 11-(2-naphthyloxy)-1-undecanol

The general procedure for phenolic ether synthesis was followed based on the following amounts: 11-Bromo-undecan-1-ol (10.0 g, 40 mmol) and 2-naphthol (14.3 g, 100 mmol, 2.5 eq) and KOH (9.0 g, 160 mmol, 4 eq) Yield: 8.47 g, 67%.

^{1}H NMR 300 MHz ($CDCl_3$): δ = 7.73 (m, 3H), 7.41 (m, 1H), 7.31 (m, 1H), 7.13 (m, 2H), 4.06 (t, 6.6 Hz, 2H), 3.62 (t, 6.6 Hz, 2H), 1.84 (qn, 6.6 Hz, 2H), 1.4 (m, 17H).

^{13}C NMR 75.47 MHz ($CDCl_3$): δ = 157.1, 134.6, 129.3, 128.9, 127.7, 127.6, 126.7, 126.3, 123.5, 119.1, 109.4, 106.6, 68.0, 63.1, 32.8, 29.6, 29.6, 29.5, 29.4, 29.3, 26.1, 25.8.

EI Exact Mass: calculated for $C_{21}H_{30}O_2$: 314.2246, Found: 314.2245.

(2a) 1,1'-biphenyl-4-yl 11-bromoundecyl ether

The general synthesis of primary alcohol bromination was followed based on the following amounts: 11-(1,1'-biphenyl-4-yloxy)-1-undecanol (9.25 g, 27 mmol). Yield: 2.95 g, 27%.

^{1}H NMR 300 MHz ($CDCl_3$): δ = 7.53 (m, 4H), 7.40 (m, 2H), 7.29 (m, 1H), 6.96 (m, 2H), 3.99 (t, 6.6Hz, 2H), 3.40 (t, 6.6Hz, 2H), 1.82 (m, 4H), 1.4 (m, 14H).

EI Exact Mass: calculated for $C_{23}H_{31}BrO$: 402.1558, Found: 402.1555.

(2b) 11-bromoundecyl 2-naphthyl ether

The general synthesis for primary alcohol bromination was followed. The amounts of reagents used were as follows: 11-(2-naphthyloxy)-1-undecanol (8.43 g, 26.8 mmol). Yield: 3.97 g, 39%.

^{1}H NMR 300 MHz ($CDCl_3$): δ = 7.73 (m, 3H), 7.41 (m, 1H), 7.31 (m, 1H), 7.13 (m, 2H), 4.07 (t, 6.6Hz, 2H), 3.41 (t, 6.6Hz, 2H), 1.86 (qn, 6.6Hz, 4H), 1.4 (m, 14H).

^{13}C NMR 75.47 MHz ($CDCl_3$): δ = 157.0, 134.6, 129.2, 128.8, 127.5, 126.6, 126.2, 123.4, 119.0, 106.5, 67.9, 34.0, 32.8, 29.5, 29.4, 29.4, 29.3, 29.3, 29.2, 28.7, 28.1, 26.0.

EI Exact Mass: calculated for $C_{21}H_{29}BrO$: 376.1402, Found: 376.1402.

(3a) 11-(1,1'-biphenyl-4-yloxy)-1-undecanethiol

The general synthesis of thiol via thiourea was followed based on the following amounts: 1,1'-biphenyl-4-yl 11-bromoundecyl ether (2.95 g, 7.3 mmol). Yield: 2.36 g, 90%. Melting point: 65-66 °C.

^{1}H NMR 300MHz ($CDCl_3$) δ= 7.55 (m, 4H), 7.42 (m, 2H), 7.32 (m, 1H) 6.96 (m, 2H), 4.00 (t, 6.6Hz, 2H), 2.51 (q, 7.4Hz, 2H), 1.80 (qn, 6.6Hz, 2H), 1.60 (qn, 7.4Hz, 2H) 1.3-1.55 (m, 15H).

^{13}C NMR 75MHz ($CDCl_3$): δ = 158.8, 141.0, 133.6, 128.8, 128.2, 126.8, 126.7, 114.9, 68.2, 34.2, 29.7, 29.6, 29.5, 29.4, 29.2, 28.5, 26.2, 24.8

EI Exact Mass: calculated for $C_{23}H_{32}OS$: 356.2174, Found: 356.2177. Reference spectrum included in appendix.

(3b) 11-(2-naphthyloxy)-1-undecanethiol

The general synthesis of thiol via thiourea was followed based on the following amounts: 11-bromoundecyl 2-naphthyl ether (7.55 g, 20 mmol). Yield: 3.12 g, 47%. Melting point: 32-32 °C.

^{1}H NMR 300MHz ($CDCl_3$) δ = 7.75 (m, 3H), 7.45 (m, 1H), 7.33 (m, 1H) 7.15 (m, 2H), 4.06 (t, 6.6Hz, 2H), 2.51 (q, 7.35Hz, 2H), 1.83 (qn, 6.6Hz, 2H), 1.3-1.58 (m, 17H).

^{13}C NMR 75.47MHz ($CDCl_3$) δ = 157.26, 134.78, 129.43, 129.03, 127.77, 126.81, 126.40, 123.57, 106.71, 68.14, 34.18, 29.68, 29.64, 29.54, 29.40, 29.20, 28.52, 26.25, 24.79

EI Exact Mass: calculated for $C_{21}H_{30}OS$: 330.2017, Found: 330.2014. Reference spectrum included in appendix.

(4a) bis[11-(1,1'-biphenyl-4-yloxy)undecyl] disulfide

The general procedure for disulfide formation via thiol oxidation was followed based on the following amounts: 11-(1,1'-biphenyl-4-yloxy)-1-undecanethiol (110 mg, 0.31 mmol). Yield: 80 mg, 40%. Melting point: 109-111 °C.

^{1}H NMR 300MHz ($CDCl_3$): δ = 7.55 (m, 4H), 7.42 (m, 2H), 7.32 (m, 1H) 6.96 (m, 2H), 3.98 (t, 5.9Hz, 2H), 2.67 (t, 7.4Hz, 2H), 1.79 (qn, 8.1Hz, 2H), 1.66 (qn, 7.4Hz, 2H) 1.3-1.60 (m, 15H).

^{13}C NMR 75MHz ($CDCl_3$): δ = 158.8, 141.0, 133.6, 128.8, 128.2, 126.8, 126.7, 114.9, 68.2, 39.4, 29.7, 29.7, 29.6, 29.5, 29.5, 29.4, 28.7, 26.2

EI Exact Mass: calculated for $C_{46}H_{62}O_2S_2$: 710.4191, Found: 710.4198. Reference spectrum included in appendix.

(4b) bis[11-(2-naphthyloxy)undecyl] disulfide

The general procedure for disulfide formation via thiol oxidation was followed based on the following amounts: 11-(2-naphthyloxy)-1-undecanethiol (100 mg, 0.3 mmol). Yield: 75 mg, 38%. Melting point: 66 °C.

^{1}H NMR 300MHz ($CDCl_3$) δ = 7.75 (m, 3H), 7.45 (m, 1H), 7.33 (m, 1H) 7.15 (m, 2H), 4.06 (t, 6.6Hz, 2H), 2.68 (t, 6.6Hz, 2H), 1.84 (qn, 8.1Hz, 2H), 1.67 (qn, 7.4Hz, 2H), 1.3-1.60 (m, 16H).

^{13}C NMR 75MHz ($CDCl_3$): δ = 157.3, 134.8, 129.4, 129.0, 127.8, 126.8, 126.4, 123.6, 106.7, 68.2, 39.4, 29.7, 29.7, 29.6, 29.5, 29.4, 29.4, 28.7, 26.3.

EI Exact Mass: calculated for $C_{42}H_{58}O_2S_2$: 658.3878, Found: 658.3887. Reference spectrum included in appendix.

(3b) 11-(2-naphthyloxy)-1-undecanethiol

The general procedure for thiol formation via disulfide reduction was followed based on the following amounts: bis[11-(2-naphthyloxy)undecyl] disulfide (100 mg, 0.3 mmol). Yield: 62 mg, 63%. Melting point: 65-66 °C.

^{1}H NMR 300MHz ($CDCl_3$) δ= 7.55 (m, 4H), 7.42 (m, 2H), 7.32 (m, 1H) 6.96 (m, 2H), 4.00 (t, 6.6Hz, 2H), 2.51 (q, 7.4Hz, 2H), 1.80 (qn, 6.6Hz, 2H), 1.60 (qn, 7.4Hz, 2H) 1.3-1.55 (m, 15H).

^{13}C NMR 75MHz ($CDCl_3$): δ= 158.8, 141.0, 133.6, 128.8, 128.2, 126.8, 126.7, 114.9, 68.2, 34.2, 29.7, 29.6, 29.5, 29.4, 29.2, 28.5, 26.2, 24.8.

EI Exact Mass: calculated for $C_{23}H_{32}OS$: 356.2174, Found: 356.2177. Reference spectrum included in appendix.

2.3.2 Liquid Chromatography of Compounds

All liquid chromatography (LC) was done on an Agilent series 1100 liquid chromatograph equipped with an UV-Visible and a Fluorescence detector. Data acquisition and manipulation was done through Agilent's ChemStation software and hardware interface. Separation was accomplished with an RP-C18 column (250 mm × 2 mm ID) purchased from Macherey-Nagel with a 20 µl injection loop. The solvent system used for **3a** and **4a** was 100% CH_3CN at 50 °C, 40 °C or 30 °C. Note that all solvents used had 0.1% trifluoroacetic acid (TFA) added. At 50 °C under the above solvent conditions, **3a** eluted at 4.0 minutes and **4a** at 11.0 minutes. At 40 °C **3a** eluted at 7.7 minutes and **4a** at 15.7 minutes. The eluent was monitored by fluorescence using the λ_{max} of **3a** (265 nm) as the excitation wavelength and monitoring its emission peak (330 nm). The fluorescence and UV-Visible spectra in Figure 2-2 were recorded using Agilent's software package.

Chapter 3 Electrochemistry of Gold Monolayers

The goal of this section is to describe the electrochemical experiments which lead to the formation of Au-thiol self-assembled-monolayers (SAMs) and the characterisation of the SAMs. Reductive release from the SAMs will be discussed in Chapter 4.

3.1 Instrumentation

The instrumentation required for electrochemistry consists of three components: a potentiostat, a function generator and a data acquisition device. The function generator was purchased from Gage-Applied Instruments and the data acquisition was done through a digital oscilloscope purchased from Pico Technology Limited, UK interfaced through a PC running PicoScope software. The potentiostat was a custom-built instrument optimised for measuring fast current jumps built in collaboration with Harrington, Labayen and Dean.

3.1.1 Potentiostat Design

At its most basic level, the potentiostat is simply an operational amplifier with the configuration shown in Figure 3-1. Notice that the working electrode is connected directly to ground. This design was experimentally tested by Labayen[107] and proved to give the best performance in regards to fast measurements. For the purpose of our

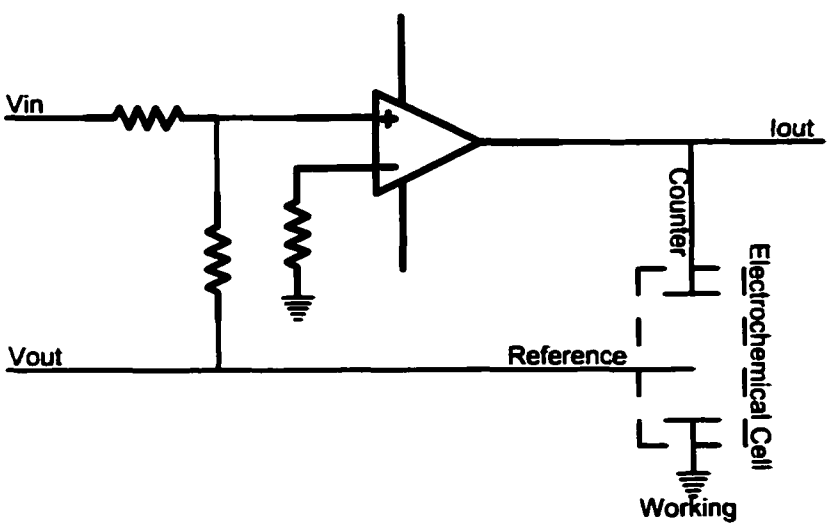

Figure 3-1. General potentiostat schematic.

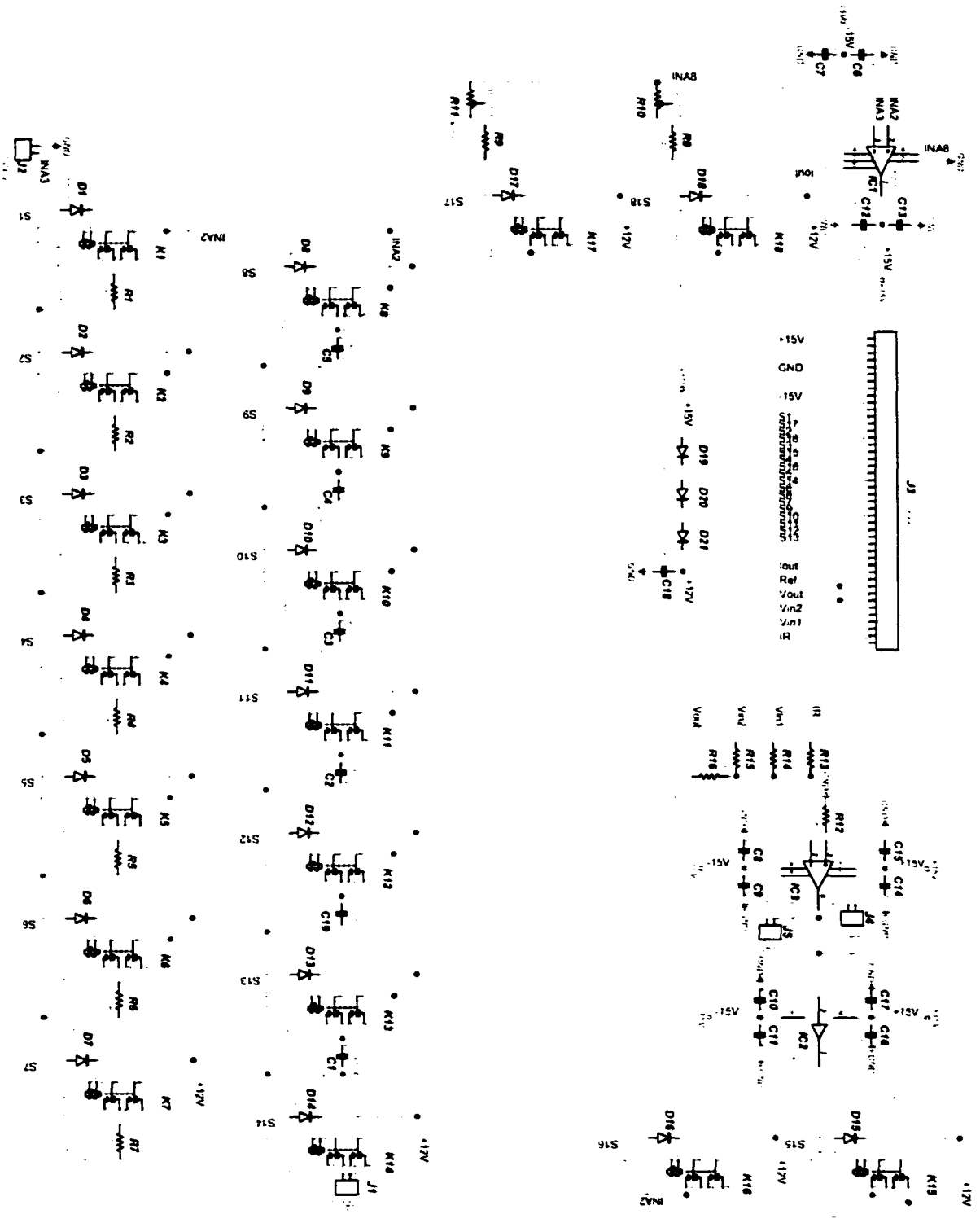

Figure 3-2. Detailed schematic of potentiostat.

experiments, the definition of fast measurements means a potentiostat and acquisition system capable of responding and recording currents in the microsecond time domain.

The performance specifications are summarized in Table 3-1 as reported by Labayen[107]. Although only an operational amplifier is required, the practical potentiostat requires a filter, amplifier and a booster to increase its current output. In addition, a voltage follower was used in the reference to limit current leakage down unwanted pathways. While these additions give the potentiostat a more useful range of operation conditions, they have the effect of slowing the response. With much optimising and component selection, a bread-board potentiostat with satisfactory specifications was created.

From this prototype, a schematic drawing was created, as shown in Figure 3-2. It was then necessary to convert the schematic drawing to a Printed Circuit Board (PCB) image shown in Figure 3-3. Both the schematics and PCB layout were drawn using Ivex software suite. The PCB's purpose was to decrease noise, and hence increase sensitivity, by having shorter wire trace lengths and more shielding. To accomplish this, not

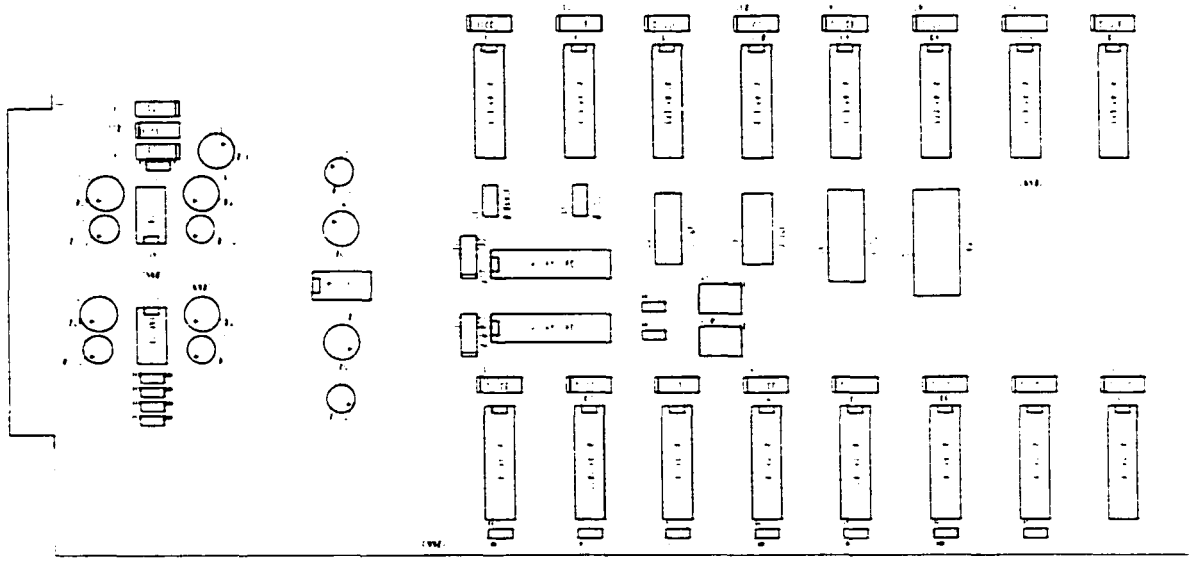

Figure 3-3. The component layout image of the potentiostat for the PCB.

only was the wire trace length minimized but the top face of the board was grounded with a copper mesh. This latter request was impossible to meet with only one surface to work with since every optimisation had a minimum of 20 wire crossings. A compromise was struck that had the bulk of the top surface mounted on a ground plane with the remaining components grounded from the bottom face. An image of the component layout is shown in Figure 3-3 to illustrate that the operational amplifiers were placed on the board as close

to the outputs as possible to minimize wire length and hence lower

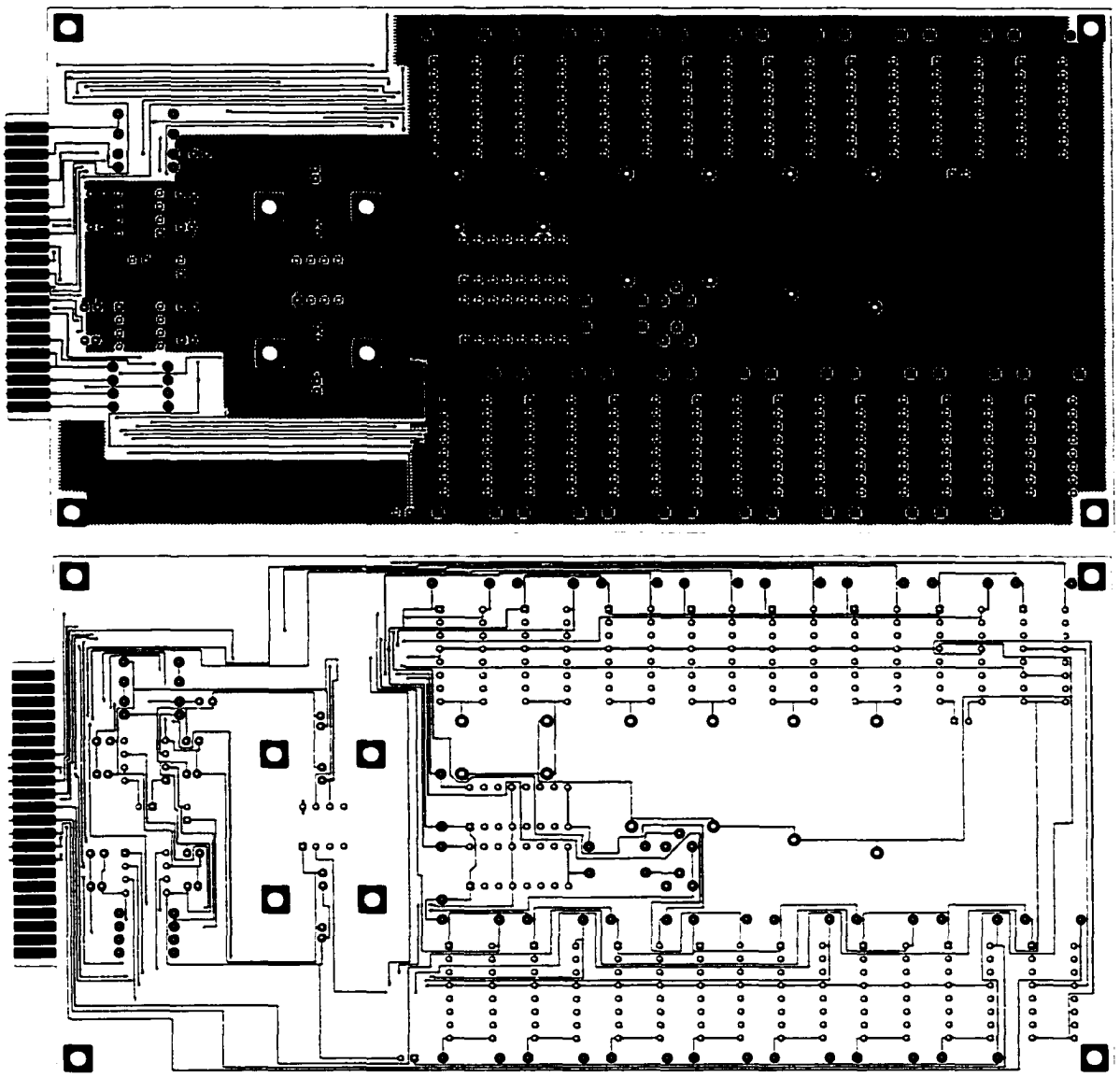

Figure 3-4. PCB images of the top side and bottom side of the potentiostat PCB after wire trace optimisation.

antennae effects. The actual dimensions of the PCB are 20 cm by 10 cm. For completeness sake, and troubleshooting, the traces of both the top and bottom layers are included in Figure 3-4. The top view shows how the copper ground plane nearly covers the whole board, providing more shielding than the prototype model.

In total, five circuit boards were printed, populated and assembled into five functional potentiostats that have the performance specifications listed in Table 3-1.

Table 3-1. Performance specifications of home built potentiostat.

Power Amplifier	
Compliance Voltage	15 V
Max current without booster	10 mA
Max current with booster	300 mA
Rise time for potential step (from 0 to 0.5V.vs.RHE step in 0.5M H_2SO_4, 0.1cm^2 Pt electrode)	90% rise time: 2 μs time to stabilize: 4 μs
Current Measurements	
7 Ranges: Decades	1 A/V, 0.1 A/V, 10 mA/V, 1 mA/V, 0.200 mA/V, 0.1 mA/V, 10 μA/V or user supplied external resistor
6 Ranges of Filter Capacitors	0.068, 0.15, 1.5, 2.2, 4.7, 6.6 μF
13 Gain Ranges	×1, ×2, ×5, ×10, ×20, ×50, ×100, ×200, ×500, ×1000, ×2000, ×5000, ×9000
Voltage follower accuracy	± 0.1 mV (± 0.1%)
Voltage input impedance	100 kΩ

3.1.2 Electrochemical Cell Design

The primary consideration in the design of the cell was that it had to perform conventional three-electrode electrochemistry. In addition, a balance was needed between the following points: the largest possible gold surface area, the smallest possible cell volume, highly reproducible gold surface areas, and easily cleaned to trace contaminant levels. Many attempts were made to increase surface area using high surface area gold substrates such as gold mesh, gold powder and planar gold foil. Gold powder was extremely difficult to clean, and gave erratic release results so it was abandoned as a candidate surface. Gold mesh was also discarded as a potential surface because it was too fragile and consequently its surface area was not reproducible. The most success came from gold foil (0.5 mm thick), which produced clean electrochemical behaviour. However, with gold foil, the analytical requirements were not met. The cleavage results were irreproducible most likely due to a changing surface area after each cleaning cycle. It was not until gold-coated glass slides (purchased from EMF, Albany New York) were used that reproducible areas were obtained. In addition, these slides are

sufficiently inexpensive that they can be single use. The electrochemical cell is shown in Figure 3-5 and Figure 3-6. The cell body itself is made of Teflon which has the

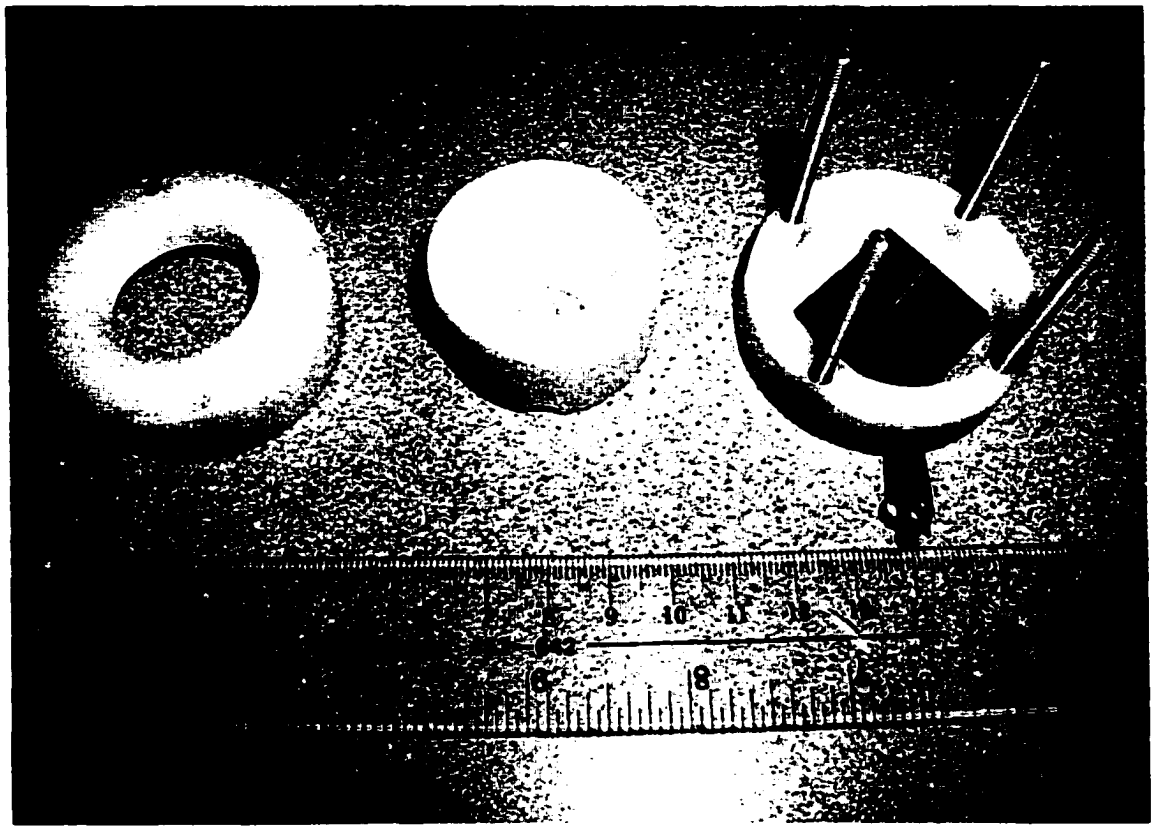

Figure 3-5. Electrochemical cell disassembled.

Figure 3-6. Top and side views of assembled electrochemical cell.

advantage of being slightly pliable thus able to form a tight seal with a glass surface without the aid of an O-ring. A reproducible area is only possible if the Teflon piece abutted to the glass is polished with 1500-grit silicon-carbide sandpaper to prevent leakage and gold surface scratching. In addition, Teflon is an excellent insulator so

leakage current is not an issue and it is relatively inert thus opening a large range of reagents that can be used for cleaning. However, Teflon has the disadvantage of O_2 permeability, which can have dramatic effects on the electrochemistry. To circumvent the oxygen diffusion problem, an argon blanket was used before and during the experiment. The cell volume compartment is an interchangeable cylinder of Teflon that allows different exposed surface area experiments to be conducted once it is clamped to the gold-glass slide. The theoretical minimum of electrode area for a 1.0 mL volume, based on the detection limit determined for **3a** and coverage of 10^{14} molecules·cm^{-2}, is 0.1 cm^2. The interchangeable Teflon sleeves permit surface areas ranging from 0.5 cm^2 to 1.5 cm^2.

3.2 Self-Assembled Monolayer (SAM) formation

There are two methods to prepare SAMs. The first is the standard methodology developed by the early work in this area[103,108-111] whereby Au substrates are placed in ethanolic thiol solutions under open circuit conditions. The spontaneous process of monolayer (ML) formation generally takes about 24 hours for tightly packed monolayers but is dependent on head group functionality[112] and concentration of thiol solution[113]. SAMs constructed from disulfide adsorption are reported to be indistinguishable from SAMs made from thiols[106,114]. This does not mean the adsorption kinetics of the adsorption process are the same but the resulting ML is identical at atomic resolution. The structure and properties of the resulting MLs have been extensively studied[64,67,77,78,101,104,114-138]. Lennox[79] reported in 1998 that a slightly positive potential applied to the Au electrode during the deposition reaction dramatically accelerated the deposition of thiols on Au surfaces. Not only does it reduce the monolayer formation time from 24 hours to 15 minutes but it also produces better-insulating monolayers[79]. The potential-controlled deposition is a leap forward compared to the open-circuit method employed by most other groups. During the deposition of a monolayer under open-circuit conditions, the potential immediately goes negative as electrons are released in concert with thiol adsorption. Then, slowly the potential climbs to almost neutral over the 24-hour period indicating monolayer formation is complete. The fate of the hydrogen

during the adsorption process has not been definitively solved but most evidence[77,78] points to the hydrogen coupling with itself forming H_2. Unfortunately, the potential-assisted adsorption reaction only works with thiols, not disulfides, so the open-circuit method cannot be abandoned altogether. The explanation of why thiols work with this method and disulfides do not work with this method, lie in the redox process of adsorption, shown in Figure 3-7. Under slightly positive potentials the electron build up can be consumed by the electrode and allow thiols in bulk solution to freely diffuse to the Au surface instead of being repelled by the negative charge build up.

$$Au + RSH \longrightarrow Au\text{-}SR + H^+ + e^-$$
$$Au + RSSR \longrightarrow 2Au\text{-}SR$$

Figure 3-7. Thiol and disulfide redox reaction with Au.

The mechanism of SAM formation under open-circuit conditions has been a debated topic since the early 1980s. Definitive mechanistic evidence is still lacking. The proposed mechanisms are shown in Figure 3-8. Reactions (a) and (b) describe thiol adsorption and reactions (c) and (d) describe disulfide adsorption. Reaction (a) is proposed by Ulman[77] and Brust[139] while reaction (b) proposed by Ulman[77], Bard[65] and Schlenoff[136]. Reaction (a) proposes an oxidative addition to Au forming thiolate and hydride. The hydride subsequently reacts with Au to form a metal-hydride covalent bond leaving and an electrostatic RS^--Au^+ bond. Reaction (b) is the reduction of RSH to form

(a) $RSH + Au_{(s)} \rightleftharpoons [RS^- Au^{2+} H^-] \cdot Au_{(s)} \rightleftharpoons [RS^- Au^+] + \frac{1}{2}H_2 \cdot Au$

(b) $RSH + Au_{(s)} \rightleftharpoons RS\text{—}Au + \frac{1}{2}H_2$

(c) $RSSR + 2Au_{(s)} \rightleftharpoons RSSRAu_{2(s)}$

(d) $RSSR + 2Au_{(s)} \rightleftharpoons 2RSAu_{(s)}$

Figure 3-8. Proposed mechanisms for thiol and disulfide chemisorption to Au.

a covalent Au-S bond and hydrogen leaves as H_2 gas. Reaction (a) has the strongest evidence by Brust who reported direct observation of the Au-H hydrogen by ^{1}H-NMR on Au nanoparticles. It is necessary to point out that the formation of the Au-H was only observed under some conditions and cannot be applied to all systems. All other evidence in favor of reaction (b) is based on an unobservable event. No group has found H_2 gas

leaving the surface or any Au-H bonding characteristics. The mechanism for disulfide forming monolayers is under less scrutiny. The two scenarios presented for disulfide adsorption are included to show the continual development of this field. Reaction (c) is described as a chemisorbed species with the disulfide remaining intact upon adsorption. In contrast, reaction (d) results in the cleavage of the disulfide upon adsorption yielding a monolayer the same as reaction (b) describes. As recently as 1995, reaction (c) was presented as a feasible mechanism[136] whereby the adsorbed disulfide kept its disulfide bond distance upon adsorption. Structural evidence on monocrystalline Au surfaces had indicated the S-S bond distance was 2.2 Å. At the time, it was surprising because others were not able to detect any physical difference between monolayers formed from thiols or disulfides. In 1997, Ishida[140], published a convincing argument that the S-S bond was cleaved upon Au chemisorption and the earlier results were misinterpreted by not accounting for the tilt angle of the monolayer.

As expected, thiols **3a** and **4a** form Au-SAMs under both open-circuit and controlled-potential (**3a** only) conditions. Under controlled-potential adsorption, the current trace is the same for every glass slide used, so a representative trace is shown in Figure 3-9. Notice the integrated area of 3.4 $mC \cdot cm^{-2}$ which corresponds to 6.4×10^{16} electrons. As Figure 3-7 describes a one-electron adsorption process, an electrode of area 1.5 cm^2 and a coverage of 10^{14} $molecules \cdot cm^{-2}$, the total number of electrons should be only 1.5×10^{14}. The disparity between numbers is rationalized by the current contributions to the trace. The trace in Figure 3-9 is the sum of both capacitive and faradic currents and no attempts were made to differentiate between the two contributors. The noise present in the trace is caused by the bubbling of argon used to deoxygenate and stir the deposition solution. For a concise comparison of open-circuit versus potential-assisted monolayer formation see the Lennox[79] paper. The results from thiol **3a** and disulfide **4a** are directly comparable to Lennox.

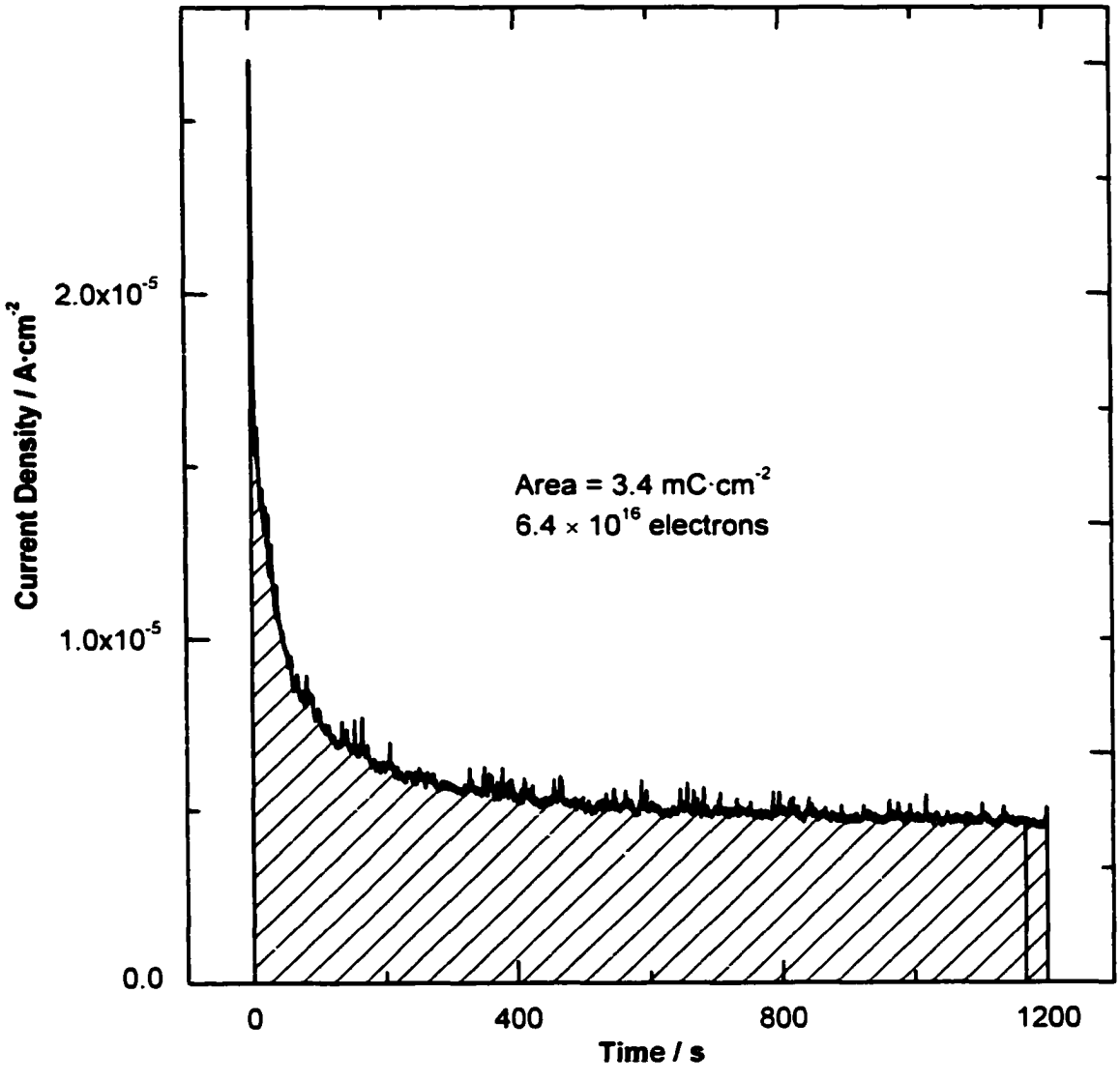

Figure 3-9. 3a adsorption profile under controlled-potential deposition conditions (+0.6 V vs Ag/AgCl).

3.3 Monolayer Characterisation

3.3.1 Cyclic Voltammetry

A standard method[110,141-143] to probe monolayer integrity is to use the Au-SAM as the working electrode in a cyclic voltammetry experiment in a solution containing a redox active species, specifically $Fe(CN)_6^{3-}$. $Fe(CN)_6^{3-}$ was chosen because it is water

soluble and it is has a reversible one-electron redox process in a potential zone where neither electrolyte nor solvent compete for electrons. For a reversible one-electron process, the following expression is valid for cyclic voltammetry; E_{pc} and E_{pa}

$$E_{pc} - E_{pa} = \frac{58mV}{n} \text{ at } 25\ ^{\circ}C$$

are the cathodic and anodic peak potentials respectively and n is the number of electrons passed in reduction. The position of E_{pc} and E_{pa} are unaltered by scan rate but the resulting current (i_{pa} and i_{pc}) increases as the square root of scan rate. Since all experiments were done at 100 $mV \cdot s^{-1}$ the relationship with scan rate was unexplored.

Cyclic voltammetry is the standard method to probe SAM integrity because it is sensitive to defect sites and allows immediate response to detrimental changes in the monolayer structure. Figure 3-10 illustrates the three scenarios encountered in monolayer integrity interpretation. The left column of Figure 3-10 is a molecular representation of the bulk properties seen in the right column. In the first scenario (a), the voltammagram clearly shows anodic and cathodic peaks resulting from Fe(III) being reduced to Fe(II) on the forward wave and the oxidation on the reverse wave. The area of the anodic peak is the same as the area of the cathodic peak implying a completely reversible process under these conditions. In addition, the difference between E_{pa} and E_{pc} is 58 mV implying a one-electron process. Note the magnitude of the peaks as compared to the other scenarios. On a clean, bare Au electrode, the redox active species has direct contact with the electrode surface allowing efficient electron transfer to occur. The only problem to plague this measurement is that insufficient cleaning results in a decreased peak height. Scenario (b) represents an Au electrode completely covered with alkyl thiol groups. The difference is a complete blocking of the redox active probe to the Au electrode. The insulating properties of an Au surface modified by alkyl thiols have been studied and show length dependence[102]. Alkyl chains shorter than nine carbons result in leakage current to the redox active species even while the monolayer is intact. It was proposed that this effect is caused by electron tunneling[103,144]. The last scenario (c) is the intermediate case where defects in the monolayer allow the redox probe to penetrate and make contact with the Au electrode producing a dampened current response as compared

to the bare Au response. Note that there is not a linear relationship between monolayer coverage and i_{pc} or i_{pa}. The non-linear response enables the voltammagrams to be good indicators of monolayer integrity because the current response to small defects is

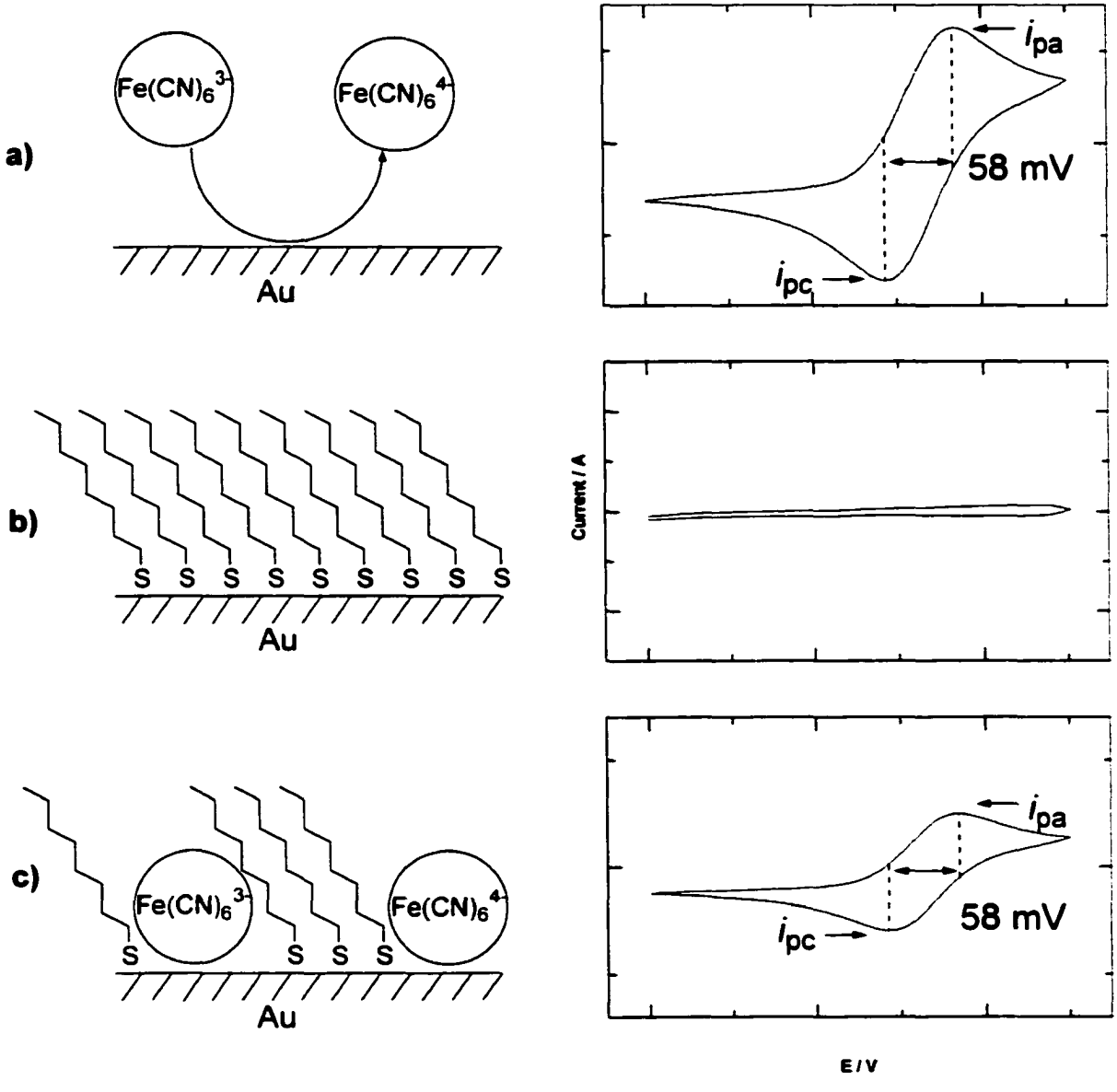

Figure 3-10. Schematic representing three scenarios found in monitoring monolayer integrity. a) The voltammagram recorded for a freshly cleaned Au surface. b) The voltammagram of a monolayer with complete coverage. c) A voltammagram of a monolayer that is partially cleaved or contains defect sites.

proportionally larger than the response to large defects[79]. The surface coverage to peak height relationship was not investigated because it requires an instrument to directly measure coverage, which is currently unavailable.

3.3.1.1 Butanethiol Monolayers

Although monolayers on Au of butanethiol are able to form highly stable, tightly packed monolayers[85,93,96,124], these are unable act as an insulating layer like their longer

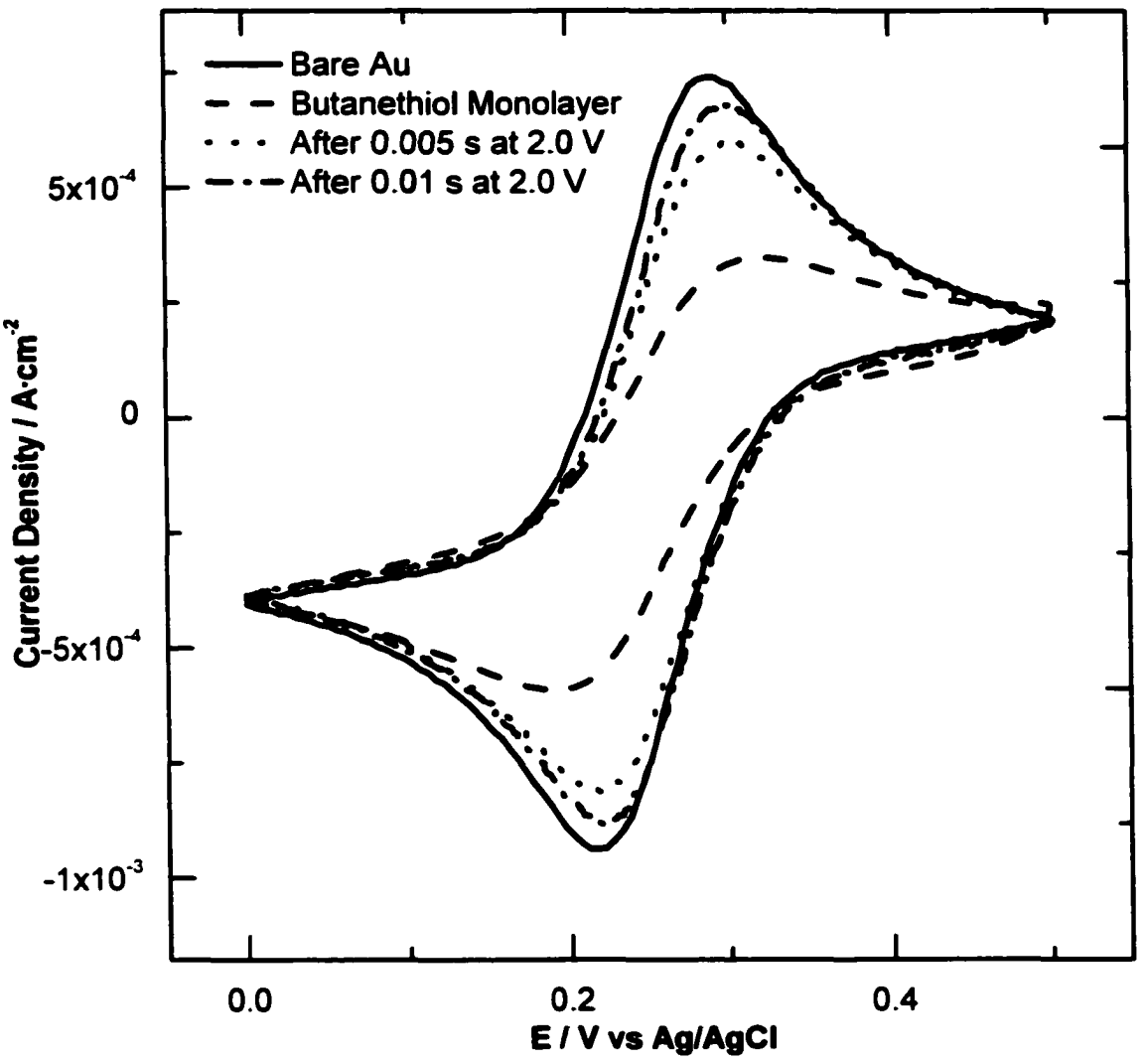

Figure 3-11. Cyclic voltammetry as a tool to probe the surface the surface integrity following two cycles of reductive desorption.

alkyl chain cousins[104]. Nevertheless, studies of butanethiol's redox blocking abilities do provide insight into the molecular structure on the monolayer. Figure 3-11 shows the cyclic voltammagrams of bare Au, the monolayer protected Au and an Au surface following partial desorption by monolayer reduction. The methodology of the reductive

desorption will be detailed in Chapter 4. In Figure 3-11, the time of applied potential, stated as 5 ms, is not an accurate representation of what occurred but rather this was the time resolution of the instrument then available. It was because of the limit of the time scale resolution that the decision was made to build a potentiostat capable of recording events on the microsecond time scale. Figure 3-11 clearly illustrates that the Au surface is becoming more "unprotected", as evidenced by the increasing i_{pa} height, with successive reductive desorption events taking place. Note, the i_{pa} peak heights after the last desorption event are approximately 80% of the original bare Au value but, this does not imply that 80% of the surface is thiol free.

The initial work on butanethiol produced several conclusions and new directions. First, a longer alkyl spacer group was needed to effectively block current passivation and as a result the synthesis was forced to incorporate the longer alkyl spacer. This was not only confirmed here but also by several papers studying the effects of chain length on monolayer stability. Second, cyclic voltammetry is an easy and sensitive way to assess monolayer integrity. Finally, the release of covalently bound thiols at an applied potential provides a tool to release a small amount of compound under potential control.

3.3.1.2 Multistep Synthesis on Gold Supports

From the perspective of an organic chemist, spontaneous adsorption of thiols on Au and reductive release resembles a conventional protecting/deprotecting step. Thus an Au surface has potential to act as a support for multistep synthesis. Numerous groups[142,144-178] have now done multistep solid-phase synthesis on Au surfaces opening a large growth area for surface modification. Although this area of research was not explored thoroughly, it is worthwhile mentioning the process and results since they pertain to the use of cyclic voltammetry as a diagnostic tool to follow the synthesis. Cyclic voltammetry allows the use of an external redox couple, Fe(II)/Fe(III), to monitor changes in SAM. The synthetic scheme is outlined in Scheme 3-1. After each synthetic step the Au surface is interrogated by cyclic voltammetry in the presence of 10 mM $Fe(CN)_6^{3-/4-}$. The voltammagram of the bare Au wire is recorded as the starting point since each electrode may have a slightly different surface area that is reflected by the i_{pa}

value. The next voltammagram, of the mercaptoacetic acid monolayer, is indistinguishable from the bare Au, which is a result of the short chain length. After

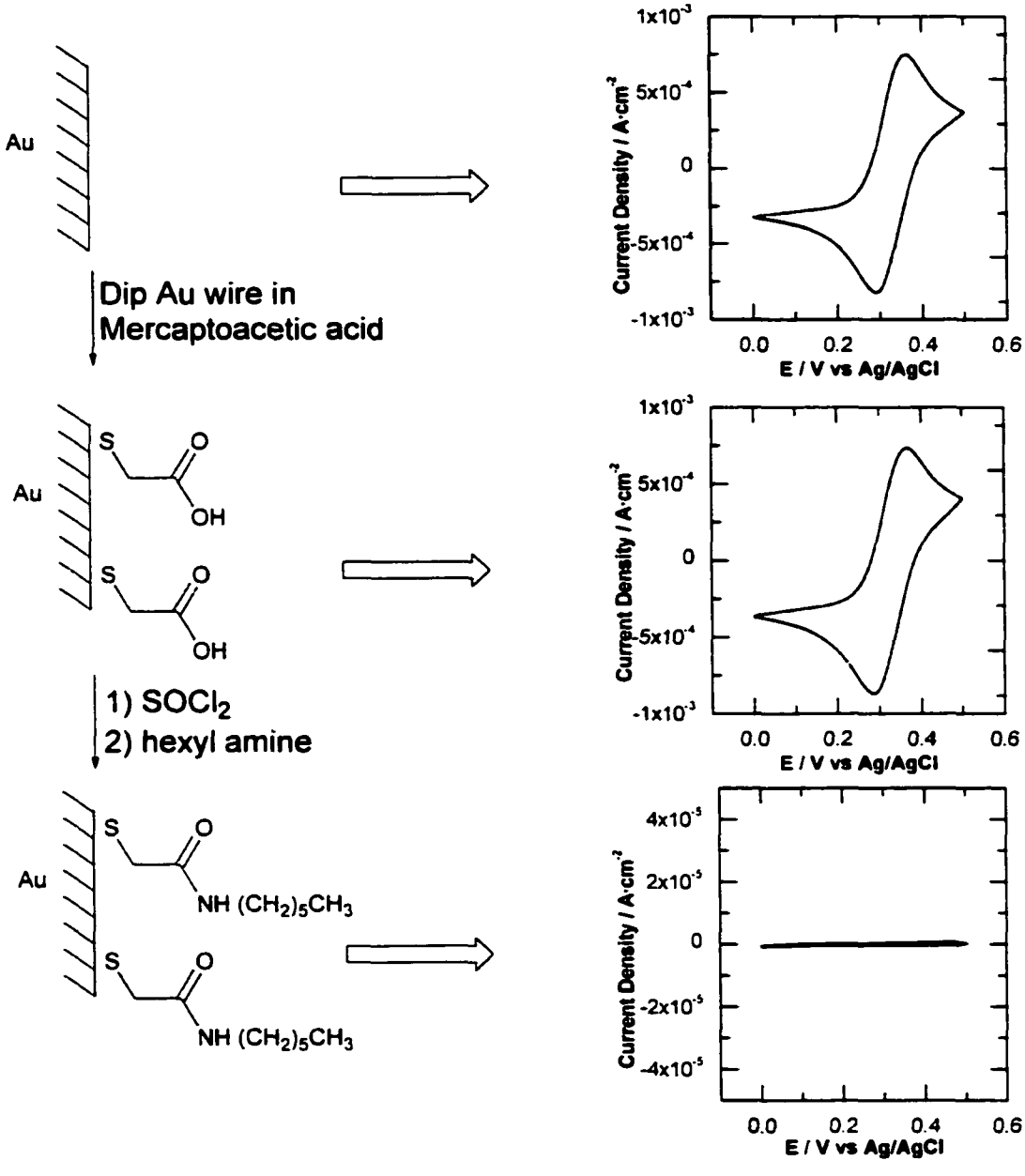

Scheme 3-1. Synthesis of N-hexyl mercaptoacetamide with Au as a solid support.

formation of the acid chloride surface and reaction with hexyl amine the i_{pa} value is greatly attenuated indicating a sufficiently insulating monolayer to block the Fe(II)/Fe(III) couple. This experiment does show the shortcomings of using cyclic voltammetry as the only tool to monitor reaction progress because a complete reaction

and non-reaction, in the case of short chain thiols, produce indistinguishable results. The blocking of current passivation to the redox probe could be enhanced by the intermolecular hydrogen bonding of the amide moiety. Hydrogen bonding in monolayers has been shown to enhance monolayer stability and hence its insulating properties by several groups[128,179-184]. While the synthesis is very simple, it does illustrate two points. First, Au can be used as a possible alternative to polymeric supports and second, cyclic voltammetry is a good tool to monitor reaction progress.

3.3.2 Capacitive Measures of Monolayer Integrity

The cyclic voltammetry method to monitor monolayer integrity does not lend itself to subsequent trace analysis of released compound because of the added redox probe. In contrast, a potential step experiment provides some information about the capacitance of the working electrode[185] and it does not require an external probe like the cyclic voltammetry method. The capacitance method relies on the properties of the double layer at the electrode/electrolyte interface to provide some information about the monolayer. However, the capacitance method is not as sensitive to defect site detection as the cyclic voltammetry method and it is sensitive to changes in electrolyte and solvent.

3.3.2.1 Capacitance of **3a** Monolayers in Differing Media

SAMs were formed from **3a** using the controlled-potential deposition method on Au-glass slides as described in section 3.2. Capacitance of the double layer was derived by fitting the first 60 μs of a current response to a potential step[96] to the equations in Figure 3-13. The experiment involved a step of 100 mV (from 0 V to 0.1 V) and both the current and potential were recorded every 667 ns. The potential range chosen for the step is in a region that only diffusion processes are occurring and no surface modification is expected. The potential step and current response are illustrated in Figure 3-12. The expression represents the solution to the equivalent circuit illustrated in Figure 3-13. In

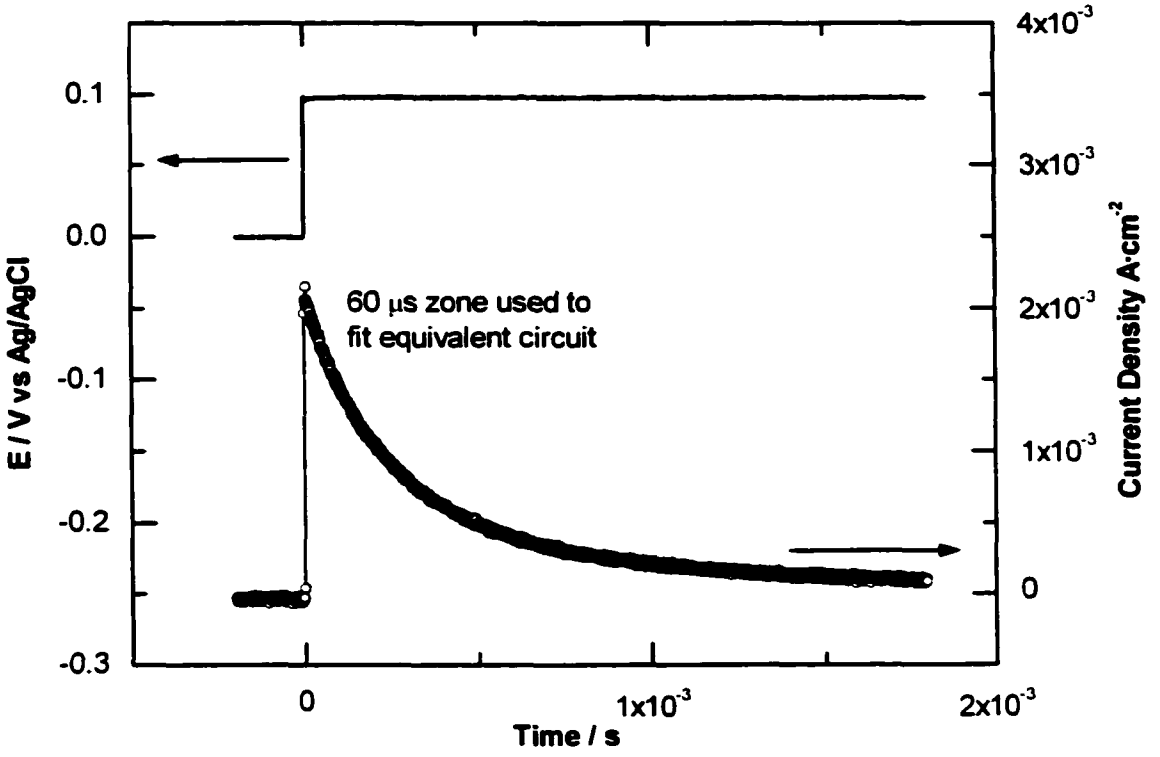

Figure 3-12. Current response to a voltage step from 0 V to 0.1 V in MeCN and 1 M Bu_4NPF_6.

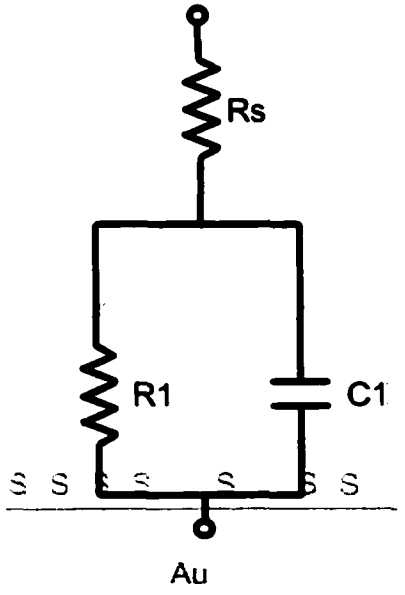

(a) $$i = \frac{E_0}{Rs + R1} \bullet \exp\left(-\frac{t}{\tau}\right)$$

$$\tau = Rp \bullet C1 \qquad Rp = \frac{R1 \bullet Rs}{R1 + Rs}$$

(b) $$i = \frac{E_0}{R1} \bullet \exp\left(-\frac{t}{\tau}\right) \qquad R1 > Rs$$

Figure 3-13. Equivalent circuit and equations used to fit chronoamperometric data and its associated physical interpretation.

addition, Figure 3-13 shows the physical interpretation of how the equation relates to the monolayer.

The Au surface is represented by the source (open circle) at the bottom of the circuit overlay. The resistor, R1, and capacitor, C1, in parallel represent the leakage and capacitance of the monolayer respectively. A monolayer with defect sites is shown. Rs is necessary to account for the voltage drop that occurs for the distance spanned from the monolayer to the reference electrode denoted by the open circle at the top of Figure 3-13. Equation (a) is the theoretical current response to a potential jump to the equivalent circuit. E_0 is the magnitude of the potential step in volts. Rs is the resistance of the solution, R1 is compensation for a leaky capacitor. At time zero, the peak current is given by the magnitude of the potential jump divided by Rs and R1 in series. τ is the decay time constant as the system returns to equilibrium at the new potential with units of seconds. The τ-term consists of Rp·C1 where Rp is the sum of R1 and Rs in parallel. However, fitting of equation (a) failed because there were too many parameters and as a result, equation (b) was used to fit the current trace. The assumption made in the simplification of equation (a) to (b) was that R1 > Rs.

Typical current traces are shown in Figure 3-14 and a summary of the fitting results is given in

Table 3-2. The capacitive measurements provide insights into the monolayer that were not available through cyclic voltammetry. The three media water, acetonitrile and DMF have very different properties relating to ion solvation. The central question is how well these solvents solvate the ions and permit monolayer penetration.

Table 3-2. Summary of capacitance fitting results* in different solvents and electrolytes under controlled-potential adsorption conditions.

Solvent	Electrolyte (1M)	Bare Au		Monolayer Au		After 0.5s at –2.0V	
		τ(s)	$R_1(\Omega)$	τ(s)	$R_1(\Omega)$	τ(s)	$R_1(\Omega)$
H_2O	$LiClO_4$	8.40×10^{-4}	19.6	7.34×10^{-5}	25.0	1.75×10^{-4}	23.8
CH_3CN	$^{\dagger}LiClO_4$	2.75×10^{-4}	15.9	2.61×10^{-4}	15.1	3.04×10^{-4}	22.3
CH_3CN	Bu_4NPF_6	2.59×10^{-4}	23.7	7.43×10^{-5}	27.8	3.16×10^{-4}	30.6
DMF	Bu_4NPF_6	1.41×10^{-4}	16.4	7.72×10^{-4}	21.1	1.32×10^{-4}	12.5

***All curve fitting had R^2 values greater than 0.997. †1.25μM 12-crown-4 was added as an ion carrier.**

The data are clearest in the case of aqueous solutions containing $LiClO_4$ electrolyte. The accepted model of a monolayer is that it is hydrophobic, tightly packed and lies in a semi-crystalline array[62,157,186]. In the case where a monolayer is placed in an aqueous medium,

well-solvated ions are unable to penetrate the monolayer and this results in a large difference between τ of the bare gold and τ of the monolayer-protected gold.

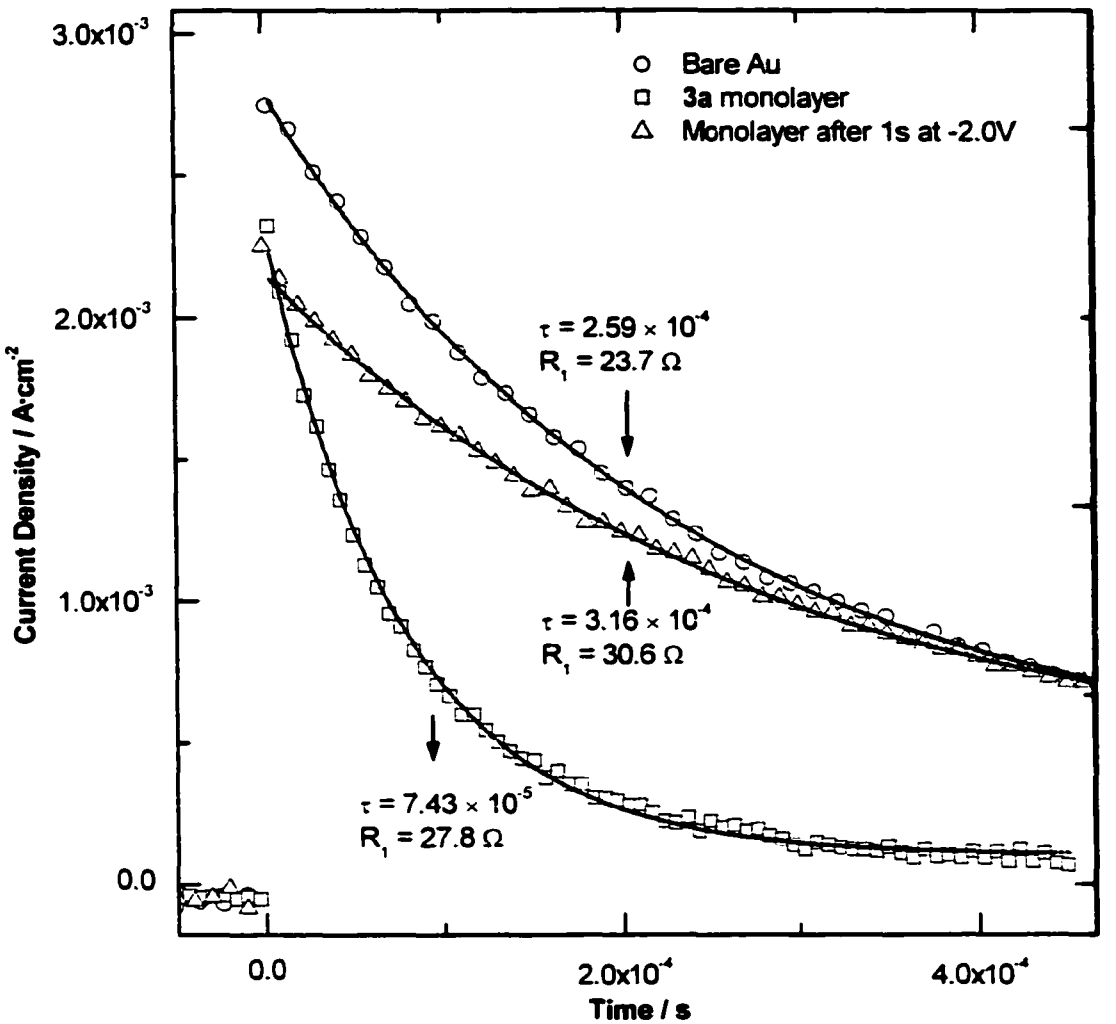

Figure 3-14. Typical current-time trace for a potential step experiment in MeCN containing 1 M Bu_4NPF_6 with the fitting result for Bare Au (○), 3a monolayer (□) and a partially desorbed monolayer (△).

The second last column of

Table 3-2 shows τ of the monolayer following 0.5 s of applied reductive potential (-2.0 V vs. Ag/AgCl). The τ increases after the reductive cleavage to a point intermediate between bare Au and monolayer protected Au. The implication is that defect sites have been opened in the monolayer by releasing compound to solution. Although

qualitatively, as expected the release in water also revealed other problems to be discussed in Chapter 4.

It was proposed that a more reproducible cleavage and capacitance measure would be obtained if the electrolyte ions could have access to the electrode[130]. Acetronitrile, more hydrophobic than water, was employed to allow ion penetration and hopefully electrochemical characterization of the cleavage. As it turns out, CH_3CN does allow ion penetration better than water as shown by τ's in

Table 3-2. In the case of tetra-butylammonium hexafluorophosphate, a very hydrophobic ion, the τ of bare gold is different than monolayer covered gold by a factor of 3.5. However, with $LiClO_4$ in the presence of 12-crown-4, a known Li^+ carrier, the τ values are similar suggesting complete ion penetration.

DMF has the best solvating properties out of the selected solvents to do a release of **3a**. Unfortunately, as evidenced by the small differences in τ values, the electrochemical handle to monitor cleavage progress is gone. DMF is hydrophobic enough to allow ion penetration to the electrode while still able to solvate a released **3a** or **4a**. By extrapolating from the cleavage results in water and acetonitrile and applying them to the DMF case, it is thought that the monolayer must still behave the same, just that the monitoring system is unable to detect the changes.

In summary, water and acetonitrile both provide a good capacitive change to monitor monolayer integrity. However, DMF renders capacitance measurements useless as bare Au is indistinguishable from monolayer protected Au. The combination of results from all solvents and both techniques has given confidence to pursue the release and capture experiments even without the ability to directly monitor the monolayer integrity at each step. Nevertheless, the loading of thiols and disulfides onto an Au surface is highly reproducible so starting conditions in all cases are very similar.

3.4 Experimental

3.4.1 Gold Monolayer Formation:

All aqueous solutions were made from Nano-pure™ water with a resistivity of 18 MΩ·cm. Concentrated H_2SO_4, H_2O_2, KCl, AgCl, KNO_3, CH_2Cl_2, EtOH, tetra-butylammonium hexaflorophosphate, $K_3Fe(CN)_6$, $LiClO_4$, MeCN and DMF were purchased from Aldrich and used as supplied unless noted otherwise. Compound **3a** and **4a** were deemed pure by ^{1}H-NMR and fluorescent analysis and thus used without further purification.

3.4.1.1 Au Cleaning Procedure

The gold surface was cleaned in freshly prepared piranha solution (70% H_2SO_4: 9% H_2O_2) by submersion for 30 minutes with periodic agitation to free surface bound bubbles. *Caution: piranha solution is a powerful oxidizer. can react violently with organics and should be stored in containers that prevent pressure build up.* After extensive rinsing (5 × 10 mL of water followed by 5 × 10 mL of EtOH) the gold was dried with a stream of nitrogen.

3.4.1.2 Electrochemical cell

A schematic diagram of the cell, Figure 3-16, is included for better representation of dimensions than the photographs in Figure 3-5 and Figure 3-6. The securing posts are long screws made of copper because sufficient pressure was needed on the Teflon housing to ensure a leak-free contact with the Au surface. An O-ring was also placed under the Au-glass slide to compensate for surface deformities in the underlying Teflon that could potentially crack the glass under pressure. The geometric exposed surface area was 1.5 cm^2 in a cell volume of 1.0 mL. Electrical connection to the Au-glass slide was made by a small, flat-nosed alligator clip. Resistance between the lead and the surface Au was verified with an ohmmeter before each experiment and any slide measuring greater than 1 Ω resistance was discarded.

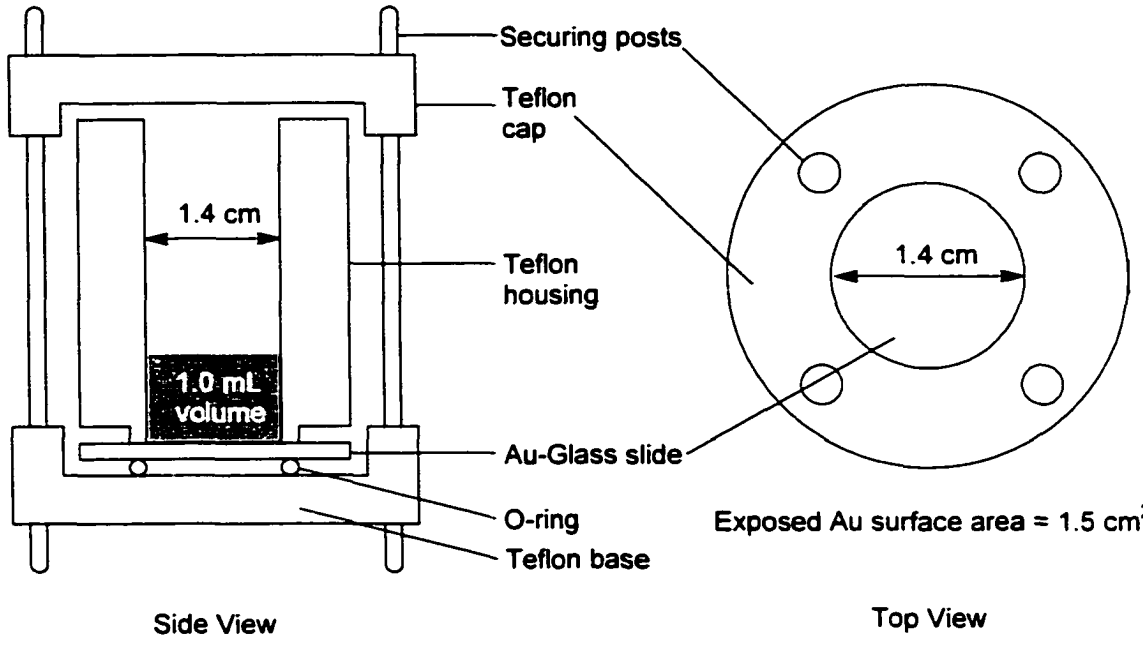

Figure 3-16. Top and side schematics of the electrochemical cell.

3.4.1.3 Open-Circuit Incubation Method

The thiol or disulfide was dissolved in ethanol to a concentration of 1 mM. If EtOH did not dissolve the dislufide (or thiol) to a sufficient concentration, CH_2Cl_2 was used as a substitute solvent. The gold surface was then allowed to sit in the thiol solution at room temperature with periodic, gentle stirring for 24 hours to establish a monolayer. After 24 hours, the gold was removed, rinsed (5 × 10 mL CH_2Cl_2 then 5 × 10 mL EtOH and finally 5 × 10 mL Nano-pure™ H_2O) and dried with a stream of nitrogen. At this point, the gold can be stored in a cool dark place under an inert atmosphere for a period of up to one week.

3.4.1.4 Potential-Assisted Deposition

This method only applies to thiols and is documented by Lennox[79]. A 1 mM thiol solution containing 1 M $LiClO_4$ or 1 M tetra-butylammonium hexaflorophosphate electrolyte was placed in a conventional three-electrode electrochemical cell. It is important to not have any contaminating halides in the deposition chamber since halides[129,130], especially chloride, are known to interfere with the formation of a complete

monolayer. The working electrode was the gold-glass slide, the counter-electrode was a platinum mesh and the reference electrode was an Ag/AgCl wire in 1 M KCl. The reference solution made ionic contact with the deposition solution via a 1% agar filled U-tube containing 2 M KNO_3. A potential of +0.6 V versus Ag/AgCl was applied for 15 minutes while the solution was stirred by a stream of nitrogen gas. The resulting monolayer was rinsed in the same manner as the above incubation method. Additionally, it was found that storage in water for 24 hours immediately after monolayer formation yields a more insulating monolayer[164].

3.4.2 Gold Monolayer Characterisation:

3.4.2.1 Cyclic Voltammetry

The gold surface is placed into a conventional three-electrode electrochemical cell (Pt mesh counter electrode, Ag/AgCl in 3M KCl reference and the gold wire working electrode, diameter 0.5 mm, geometric area 0.17 cm^2). The electrolyte was 1 M KCl containing 10 mM $K_3Fe(CN)_6$. Voltamagramms were performed by a PAR 273A (Option 97) potentiostat that was controlled by CorrWare™ software (Scribner and Associates) running on a 486 personal computer. The input triangle waveform had vertex positions at 0.0 V and 0.5 V versus the reference. Typically, five cycles were run at a rate of 100 $mV \cdot s^{-1}$ where only the last cycle was recorded. Data files were plotted using CorrView™ software (Scribner and Associates). Monolayer integrity was established by measuring the current passivation to the bulk solution containing a redox active probe ($Fe(CN)_6^{3-}$) during a standard cyclic voltammetry experiment. Monolayer coverage was established by taking the ratio of i_{peak} of oxidation (+0.3 V vs. Ag/AgCl) of bare gold to i_{peak} of oxidation of monolayer-covered gold. Typically, values of 80 or greater are sufficient to claim monolayer integrity.

3.4.2.2 Capacitance Measurements

The electrolytes used were 1 M $LiClO_4$ in H_2O, 1 M $LiClO_4$ and 1M tetra-butylammonium hexaflorophosphate in CH_3CN and DMF. The H_2O was Nano-pure™

(18 MΩ·cm resistivity), the acetonitrile was distilled over 4Å molecular sieves and the DMF was distilled from a CaH_2 slurry and stored over 4Å molecular sieves. The tetra-butylammonium hexaflorophosphate was used as purchased while the $LiClO_4$ was three times recrystallised from H_2O before use. All chemicals were purchased from Aldrich and used as received unless otherwise noted. All electrode metals, Ag, Au and Pt, were purchased from Alfa Aesar (>99.99% purity). The gold surface is placed in its custom Teflon housing and electrical contact is made by a small alligator clip. The reference is an Ag/AgCl wire in 1 M KCl that makes contact with the cell electrolyte by a 1% agar-filled U-tube containing 2 M KNO_3. The Ag/AgCl wire was made by melting AgCl in a crucible and dipping an Ag wire to coat the outside of the wire. Once the Ag wire tip was suitably coated in AgCl it was stored in a 1 M HCl solution in the dark. The counter electrode is a gold wire; area of 0.2 cm^2. The experiment uses a 100 mV potential step in a potential region where only diffusion processes are occurring for durations of 1 second. In this case, the step is from –0.1 V to 0.0 V. The resultant current jump and relaxation yields information about the monolayer integrity. The curve fits were done to the equivalent circuit shown in Figure 3-13 modeled within Origin 6.1 (OriginLab Corporation). All measurements were recorded in a grounded Faraday cage; the computer monitor was also encased in a faraday cage to directly eliminate most noise from this source.

3.4.3 Washing

During the course of the trace analysis it became apparent that extensive washings between experiments was essential. Eventually this extended to the point where all the components involved in the release experiment were disposable except the Teflon housing and counter electrode. The Teflon housing and counter electrode were rinsed in 10 volumes of CH_2Cl_2 and then boiled in Nano-pure™ H_2O for 2 hours with two water changes then placed in a heated sonication bath of 100% ethanol for 10 minutes. This extensive washing procedure was necessary because of the poor solubility of **3a** and **4a** and their particular affinity for glass.

Chapter 4 Analysis of Reductive Cleavage

The purpose of this chapter is to identify and quantify the product(s) released from the Au-thiol SAM following electrochemical reduction. Electrochemical methods will probe the reduction process and the electrode surface produced, and HPLC-fluorescence will detect and quantify the released organic product.

4.1 Electrochemical Analysis of Reductive Cleavage

The reductive cleavage of Au-S SAMs is accomplished by applying a –2.0 V potential for a specific duration of time. At this potential, the covalently bound thiol is known to undergo one-electron reduction followed by release of the organic fragment from the Au surface[89,98]. The mechanism of thiol reduction from an Au surface is not under the same scrutiny as the adsorption mechanism because all published work[85,87-89,94,96-99] is in agreement. The main technique used to determine the thiol reduction is linear sweep voltammetry (LSV). The experiment scans to progressively more negative potentials to a point where reduction occurs in concert with an increase in current. The attraction of this technique lies in its ability to detect the exact potential the thiol is reduced. The increase in peak height is cause by the Faradic current to reduce the monolayer. The constant current up to the point before reduction is the current necessary to the charge the double layer. In these experiments the current used to keep the double layer charged is assumed to be constant throughout the potential sweep region. Thus, the Faradic current can be subtracted from the capacitive current producing the number of electrons necessary to reduce the monolayer. LSV voltammetry[87,94,99] is often used in conjunction with an alternative method to determine monolayer integrity. For example, infrared reflectance spectroscopy[88,97] monitors the C-H stretching regions of monolayers where differences of peak intensities of adsorbed versus free thiolate methylenes are observed. In addition, quartz crystal microbalance (QCM) has been employed[98] to detect small mass changes as a result of reductive desorption. Chronoamperometry[85,89,96] has been used to provide experimental evidence to support mathematical models of

desorption. However, all the evidence provided regarding the identification of the released compound has come from the electrochemical point of view: one electron per sulfur atom is consumed. Characterisation of the released compound from an organic chemist's point of view is absent in the literature. It is usually assumed the product is the thiolate or the thiol but, apart from a "thiol odour", no detection of the products has been reported. As a result, the goal of this chapter is to identify and quantify the compound(s) released from an Au surface monolayer.

At such a large reductive potential the selection of solvent and electrolytes becomes limited as either may be consumed resulting in current not solely due to the Au-S reduction. For this reason water, CH_3CN and DMF were chosen as the solvents. Although water undergoes reduction at this potential, it was thought that the only by-product would be hydrogen gas, which would not present a problem for the subsequent trace analysis. The electrolytes that do not undergo any electrochemical reaction at -2.0 V were $LiClO_4$ and tetra-butylammonium hexaflorophosphate. Fortunately, both of these electrolytes were soluble in each solvent to appreciable concentrations. The following sections discuss the reduction results for several solvents and several fixed-period applied potential durations. In each solvent a reductive step of 0.5 s duration was applied and the current was integrated during the pulse period to give the total charge passed for the reductive event. The amount of charge passed is directly correlated to the number of electrons that were involved and thus an efficiency of the number of electrons required to release one molecule can be calculated. The products were determined by the HPLC analysis using the conditions discussed in Chapter 2. The number of molecules released is calculated from the fluorescent peak area of the chromatogram.

A study undertaken by Schlenoff[136] probed the surface roughness of various Au substrates. Roughness factor, *R*, is defined as the actual surface area/geometric surface area. Various techniques are available for Au substrate preparation, including evaporation, sputtering and mechanical polishing. Methods for determing *R* for Au include using electrochemistry of adsorbed iodine[187], surface oxide electroactivity[188] and under potential deposition of silver or copper[189]. Table 4-1 is a reproduction[136] indicating the roughness factor of various Au substrates. Note that sputtered Au on glass was used in all experiments and as a result, all calculations used a roughness factor of 2.0. This

defines the theoretical number of electrons required for a complete release from a known geometric area.

Table 4-1. Roughness factors of various Au substrates

Substrate	Roughness Factor
Polished Au	1.44 ± 0.1
Polished Au with annealing	1.20 ± 0.05
Evaporated Au on mica	1.70 ± 0.1
Evaporated Au on mica with annealing	1.15 ± 0.05
Sputtered Au on Glass	2.00 ± 0.1
Sputtered Au on Plastic	2.00 ± 0.1

4.1.1 Chronoamerometry of Reductive Cleavage in H_2O

The reductive cleavage in water with KCl as the electrolyte produces the trace shown in Figure 4-1 where the integrated area sums to 6.7×10^{16} electrons. This implies

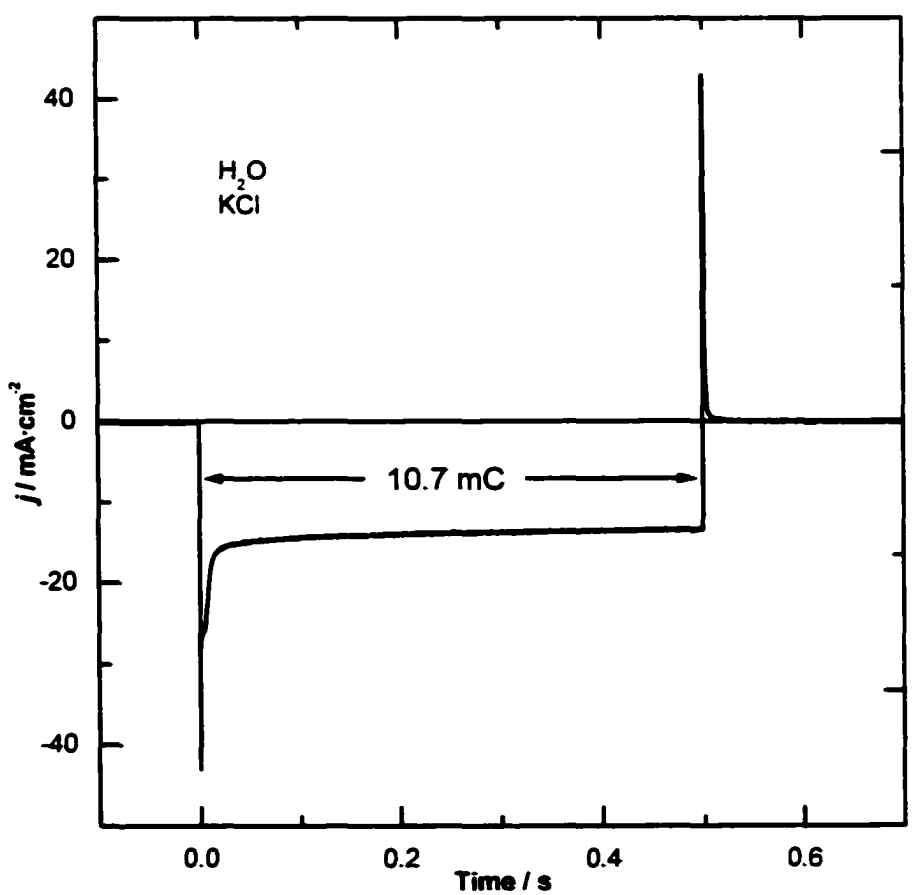

Figure 4-1. Reductive desorption of 3a in H_2O with KCl as the electrolyte.

that 450 times more electrons were passed than were need to cleave one monolayer based on 1.5 cm^2 at a coverage of 10^{14} molecules $\cdot cm^{-2}$. The excess of electrons is attributed the reduction of water to form H_2 as mentioned above but also a chemical reaction is seen to take place as the Au surface changes to a blue color. The identity of the origin of the blue color has not been pursued. It is proposed that the Au, at reductive potentials, is reacting with the chloride ions to give a blue color over the surface of the electrode. The proposal is supported by the same experiment done in $LiClO_4$, where it is known that no subsidiary reactions take place. The trace in $LiClO_4$ is shown in Figure 4-2. There is a small decrease in current passed. The difference in the two traces can arise from two factors,

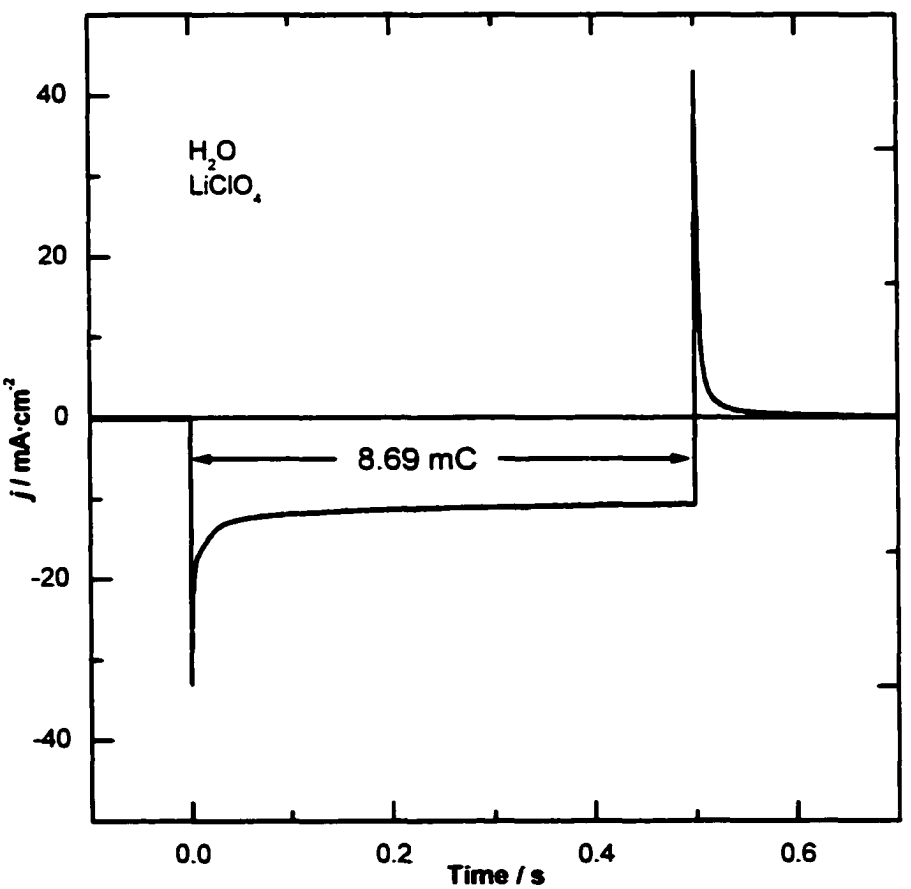

Figure 4-2. Reductive desorption of 3a in H_2O with $LiClO_4$ as the electrolyte.

electrode area and electrolyte. While the two experiments were conducted on two different glass slides, the difference due to area is negligible (5%). Consequently, the differences in total charge are assumed to be related to the electrolyte.

The main difference between Figure 4-1 and Figure 4-2 owes to the use of KCl, which as described above causes a chemical reaction to take place, thus consuming electrons on Au electrodes at negative potentials. The difference in the number of electrons for the two processes is 1.1×10^{16} electrons, accounting for an 18% decrease in electron consumption.

4.1.2 Chronoamperometry of Reductive Cleavage in Acetonitrile

The case in acetonitrile, shown in Figure 4-3, integrates to 2.84 mC of charge. Although the current consumed in this trace is less than the two aqueous cases described above, it is still a factor of 110 times more than required by theory for a monolayer. These results support the previous assumption that the removal of water from the solvent

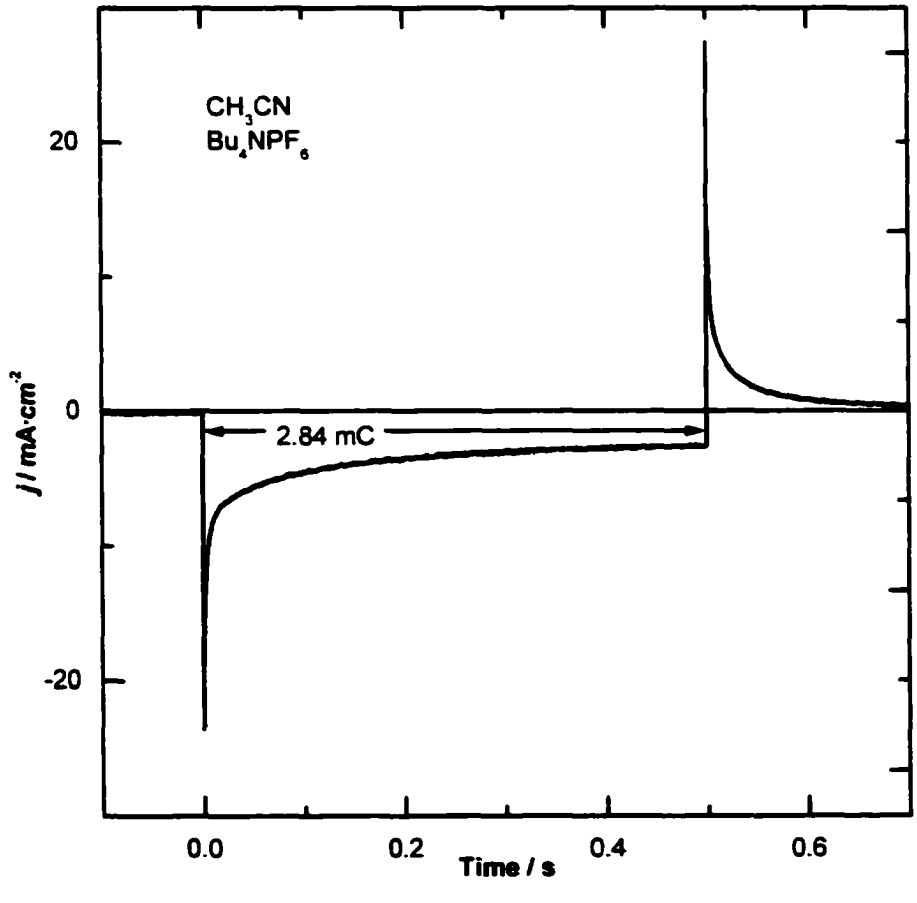

Figure 4-3. Reductive desorption of 3a in MeCN with Bu_4NPF_6 as the electrolyte.

limits the currents due to reactions other than thiol cleavage and capacitive charging. The capacitive current in this trace, where efforts were particularly stringent to keep water out of the system, must be the main contributor and the faradic current plays a minor role.

4.1.3 As a Function of Potential Duration

Although only cleavage times of 0.5 seconds have been shown for each of the cases in this section, each has another dimension of the duration of applied potential. An example of varying the duration of applied potential is shown in Figure 4-4. The reductive desorption traces look very similar and little information other than bulk electron counts can be obtained. Figure 4-4 is included because it will be used in the cleavage efficiency calculation explored in section 4.2.

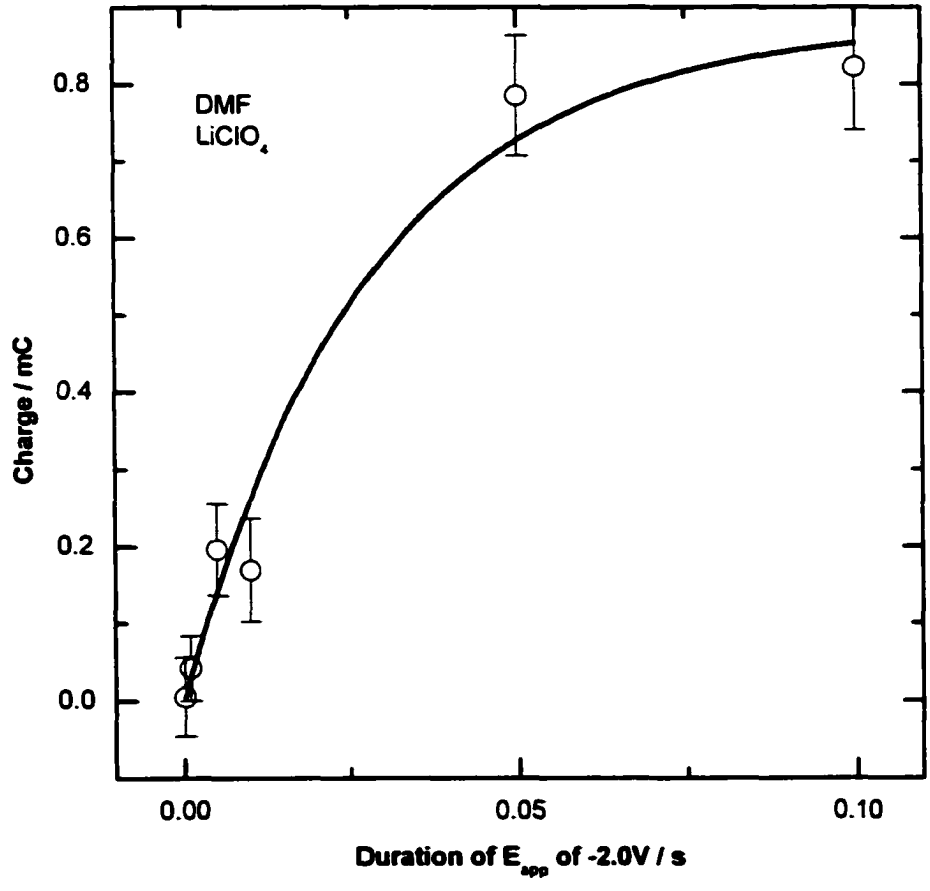

Figure 4-4. Reductive desorption of 3a in DMF containing 1M $LiClO_4$ as a function of varying applied potential duration. The line is added to aid in visualization and is of no physical significance.

4.2 Analysis of the Products of Reductive Cleavage in various media

The reductive cleavage was carried out as described above and the liquid chromatography (LC) was done on an aliquot taken from the reductively cleaved solution containing trace amounts of compound **3a/4a** or other reduction products. The chromatograms in this section will have retention times that vary slightly from those reported in Chapter 2 because the solvent system was changed several times to maximize the separation and peak sharpness. In addition, the nature of the electrolyte has an effect on retention time, especially in the case of tetra-butylammonium hexaflorophophate. Nonetheless, the peaks for **3a** and **4a** were identified in each solvent system.

4.2.1 Trace analysis of products released in H_2O

The reductive release of SAMs from **3a** in water gave the most promising results when followed by electrochemistry but the actual released quantities tell a different story. Analysis of the products by LC showed detectable amounts of **3a** at its detection threshold, but no peak that could be identified as **4a**. The release was done on a single sheet of **3a**-covered gold. The reductive step was applied in successive durations labeled in Figure 4-5 and after each pulse an aliquot was removed, the cell was rinsed and the process was repeated. A few conclusions can be drawn from Figure 4-5 regarding the feasibility of water as a release solvent. First, the only detectable product was the thiol (retention time 7.7 min at 40 °C in 100% MeCN); no disulfide was detected in the reduction. However, the amount of thiol released is near the detection limit where the precision of the method is poor. The release profile follows the general trend that the largest release concentration come in the earliest samples and gradually decrease as repeat samples are taken. This is attributted to the fact the electron transfer rate is much greater than the diffusion rate. Thus, the largest release concentration should come in the earliest samples. This is generally observed although the quantitative aspect is poor.

The first point of Figure 4-5, when duration of applied potential is 0.5 s, was expected to have been much larger since by this point a hundred-fold excess of electrons had been supplied to the system. The mass balance for the experiment is poor since only

8% of the available material was released, representing 1.3×10^{13} molecules, spread over several 750 μL aliquots.

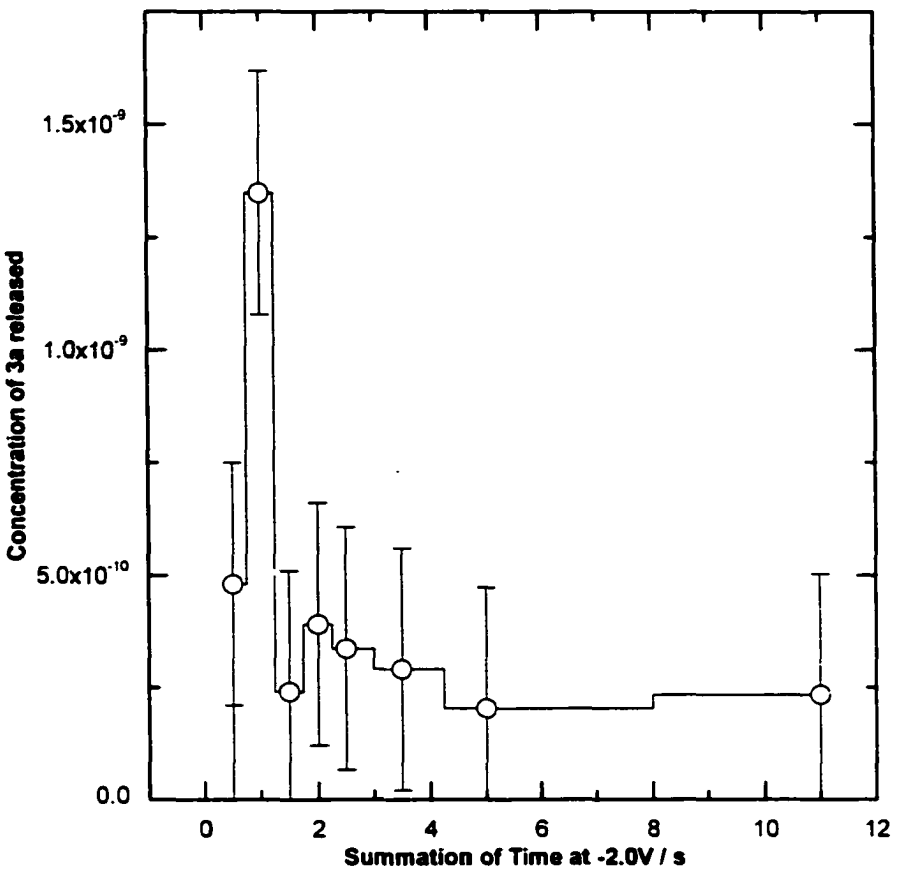

Figure 4-5. The concentration of 3a released from successive reductive periods applied to the same Au surface in aqueous $LiClO_4$.

The rationalization for the low cleavage was that **3a** is insoluble in water. It is very unlikely that electron transfer was retarded to a time scale of seconds, so after the first reduction cycle, all of the monolayer must have reduced Au-S bonds. Once the covalent linkage breaks, the monolayer is situated in an ordered hydrophobic environment where the energy required to solvate the thiol is too great and consequently little product is observed. The 8% of material that did "escape" this hydrophobic region is attributed to thiols that resided on edge sites of the Au where the freshly cleaved thiolate was accessible for solvation by the water. The evidence for the solubility issue comes from the physical observation of crystals growing on the electrode following a reductive event. These crystals are low melting (<30 °C compared to 60 °C for pure **3a**)

and the identity is unknown because there is too little material to do conventional identification assays such NMR or IR. The crystalline layer was visible to the eye, so must include more material than a single monolayer. One possibility is a mixed crystalline layer of organics, electrolyte and solvent.

4.2.2 Trace analysis of products released in MeCN

The situation in MeCN is not much more appealing, as both the release reliability and yield is low. The same procedure was followed as described above for reductive release into water. The chromatograms shown in Figure 4-6, illustrate the identification of the **3a** eluting at 4.4min (100% MeCN, 50 °C) and the difficulties regarding solvent and electrolyte purity. No peaks corresponding to **4a** were detected. The integrated areas and subsequent quantification reveals that the monolayer is only 20% cleaved from the Au surface after 1.2 s. The same arguments apply to the MeCN case as were applied in water: Compound **3a** is either too insoluble or the solvent system is not strong enough to disrupt the hydrophobic network created once it is reduced from the surface. It was thought that tetra-butylammonium hexaflorophosphate would increase the yield of release because it is hydrophobic enough to penetrate the monolayer where it can electrostatically couple with the thiolate and allow a neutral species to dissociate from the surface. However, as far as yield is concerned, no significant difference arose between $LiClO_4$ and tetra-butylammonium hexaflorophosphate as electrolytes. The difference between solvents only showed itself in the chromatogram because the tetra-butylammonium hexaflorophosphate salt had more impurities than the $LiClO_4$. In contrast to the release profile in water, the MeCN case does not go into solution in the beginning pulses but rather slowly dissolves producing more material with longer applied potentials.

4.2.3 Trace analysis of products released in N-,N-Dimethylformamide

Reductive release into DMF was tested because the solvent is known to be stable to the potential range used in desorption and it is able to dissolve **3a** and **4a** to higher

concentrations than either MeCN or H_2O. In addition, a new procedure was established to get larger signal concentrations. The Au-glass slides are known to provide reproducible areas between independent experiments and as such, a fresh Au-surface could be used for each reductive desorption. This experiment involved creating

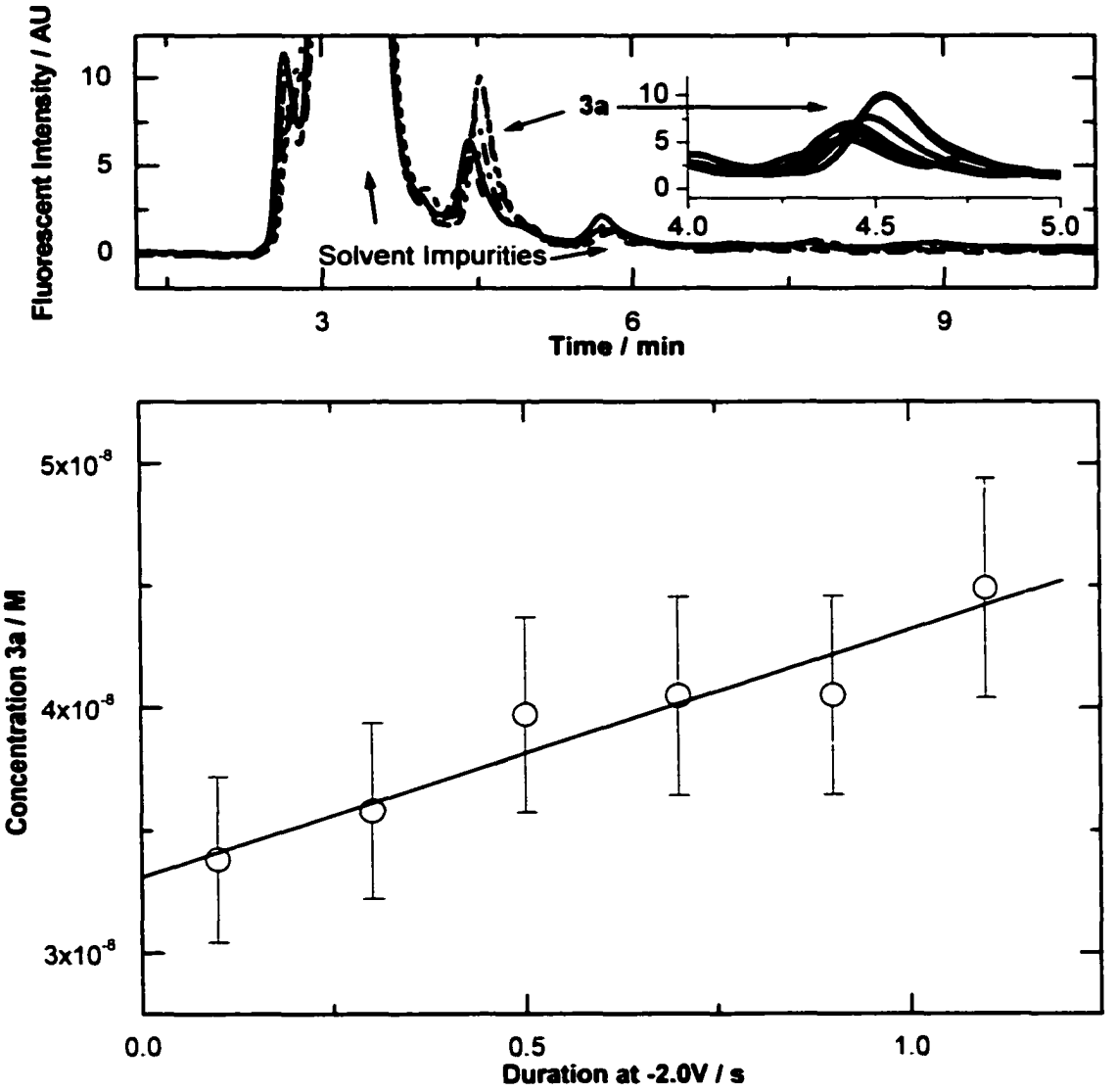

Figure 4-6. Chromatogram of 3a release in MeCN with either $LiClO_4$ and Bu_4NPF_6 as the electrolytes. The multiple traces are different durations of applied potentials. 3a retention time = 4.4 min. 4a retention time = 11 min. The line is added for visualization purposes and serves no physical meaning.

eight monolayers of **3a** on eight separate Au-glass slides by controlled-potential adsorption. Five Au slides were held at a different durations of reductive potential. The

remaining three Au surfaces were used as duplicate measurements for a determination of reproducibility.

Reductive release into DMF gave the best yield and the most reproducible results (Duplicate measurements agreed within 10% of one another). The chromatograms are

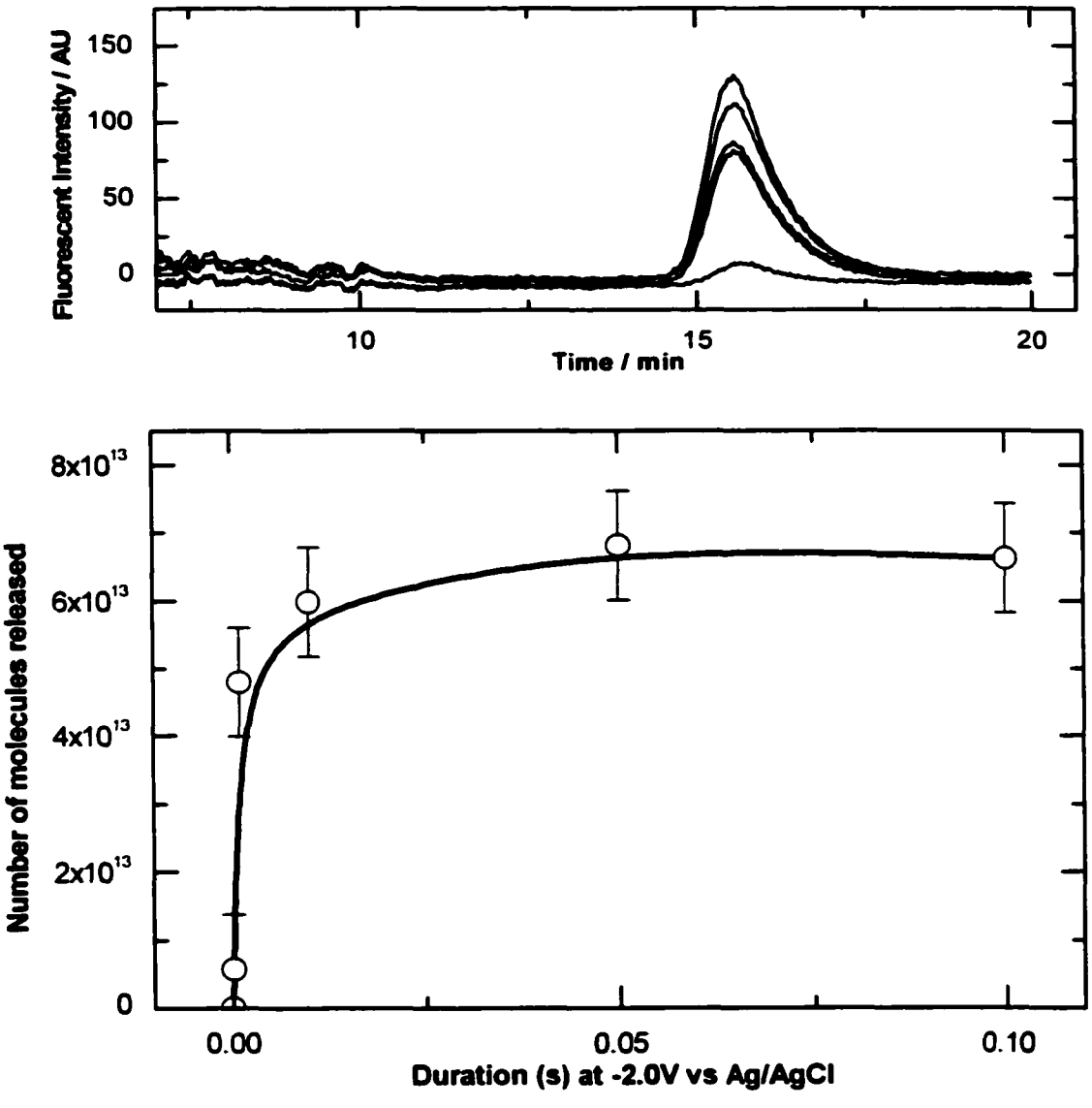

Figure 4-7. Number of molecules of 4a released from an Au surface as a function of duration of applied potential in DMF containing Bu_4NPF_6 or $LiClO_4$.

summarized in Figure 4-7; only **4a**, the disulfide, is the detected product. From a quantitative perspective, the cleavage reaches a plateau value at 6×10^{13} molecules released. If this were truly the total available from the surface, this would imply a packing density of 3×10^{13} molecules·cm^{-2} (330 Å^2 per molecule), a factor of ten less

dense than suggested by conclusive experimental evidence on monocrystalline gold. This is clearly not the case because the low packing levels are contradictory to the blocking ability of the monolayer. A second scenario assumes that not all of the monolayer was released to solution. An important distinction between release from the Au-surface and release to solution is required, as it is firmly believed that all of the Au-S bonds were reductively cleaved but not liberated to the solution. This would be consistent with the weight of numerous electrochemical studies in the literature[82,84-89,94-99].

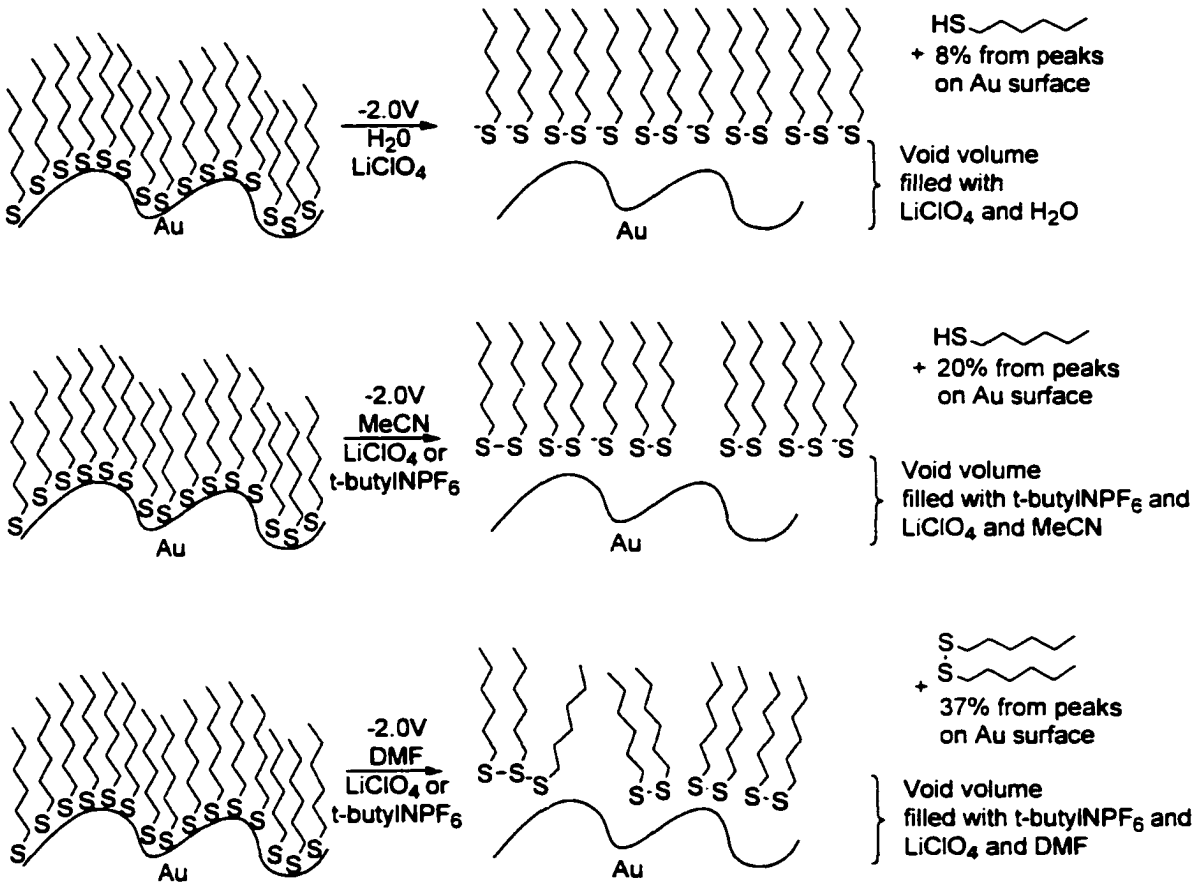

Figure 4-8. Deductions from LC results regarding the structure of the monlayer after cleavage in H_2O, MeCN and DMF.

Figure 4-8 outlines possible explanations for the results obtained in each of the solvents. In DMF, after the cleavage, there is no visible crystallization over the electrode surface, which is represented by the disordered layer of thiolates and disulfides. A possible mechanism of each of the products formed is outlined in Figure 4-9. Reductive cleavage of thiols from Au surface is well-studied electrochemically with the community in agreement that the process involves cleaving the Au-S bond in an one-electron

transfer[96-99]. The work done here illustrates that there is the possibility that other redox processes may be occurring at a distance away from the electrode. It is our theory that monolayer is cleaved as all others have stated, by a one-electron reduction process. Yet, this reduction creates a suspended monolayer structure when the alkyl chains are long enough to allow strong intermolecular attractive forces to dominate over dissolution of the monolayer. This suspended, ordered monolayer is poised to undergo

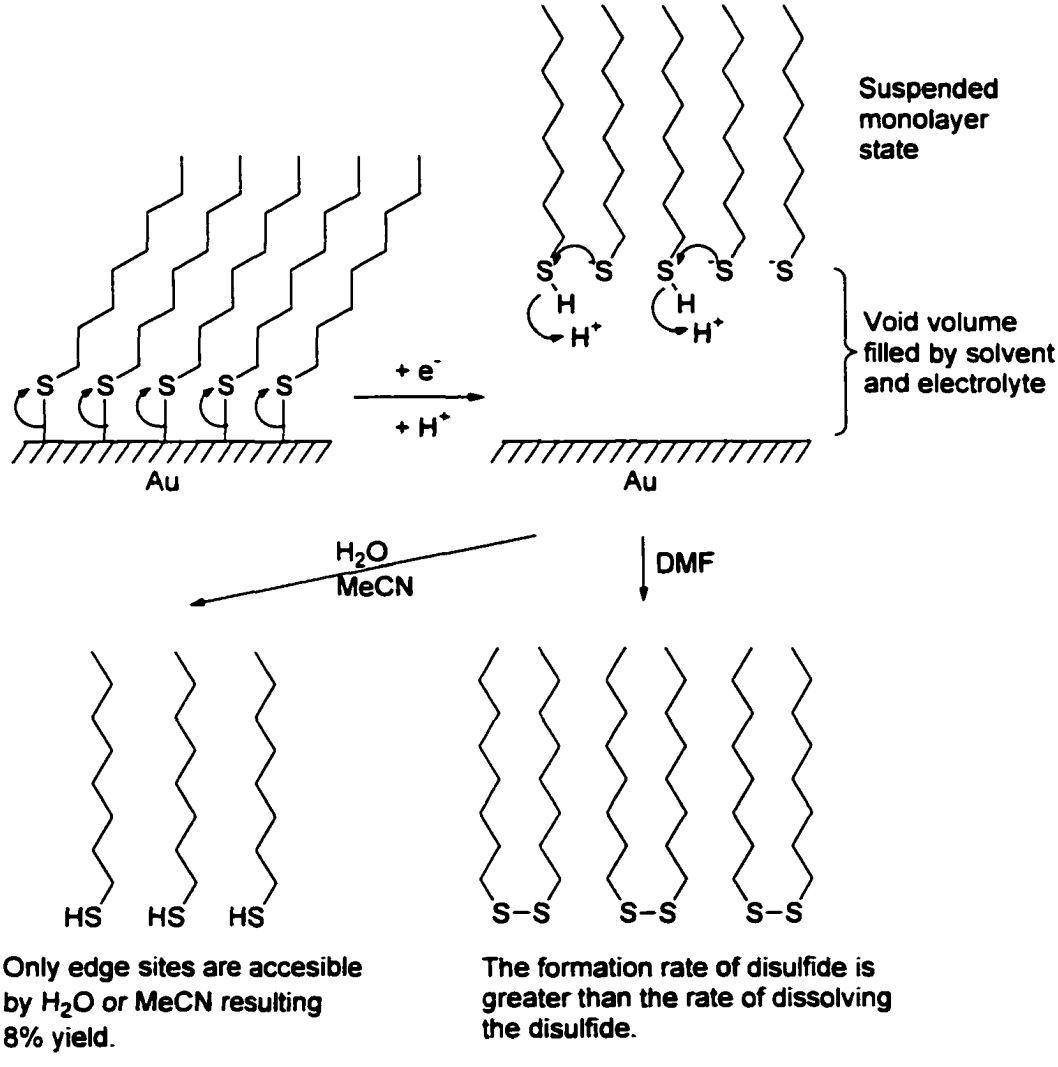

Figure 4-9. Reductive mechanisms which support LC and electrochemical data.

well-known thiol oxidation to yield disulfides. The rate of disulfide formation must be much faster than the rate of thiol/disulfide dissolution because no thiol was present in the DMF case. In contrast, in H_2O and MeCN the same suspended monolayer forms but only

the thiols that escape the hydrophobic layer are solvated. The lack of thiols in DMF could be caused by an enhanced rate of intermolecular disulfide formation.

The issue with respect to efficiency is summarized in Table 4-2. The table clearly shows that if the process is an one-electron reduction, a more rigorous experiment is needed to isolated Faradic currents from capacitive currents.

Table 4-2. Summary of 4a cleavage efficiencies in the DMF release experiment shown in Figure 4-7.

Δt_{app} (ms)	Charge (C)	No. of electrons	No. of molecules	Efficiency e^-/Molecule
100	8.23×10^{-4}	5.1×10^{15}	6.62×10^{13}	77
50	7.85×10^{-4}	4.9×10^{15}	6.81×10^{13}	71
10	1.69×10^{-4}	1.1×10^{15}	5.98×10^{13}	19
1	4.18×10^{-5}	2.6×10^{14}	4.79×10^{13}	5
0.1	5.09×10^{-6}	3.2×10^{13}	5.73×10^{12}	6

The formation of disulfides in DMF could also be the result of oxidation at the counter electrode or trace amounts of O_2 in the system. However, the counter-to-working-electrode separation is about 0.5 cm and assuming a diffusion rate of 10^{-5} $cm^2 \cdot s^{-1}$ and no convection it would take 1.3×10^4 s to reach the counter electrode. Following electrochemical reduction the aliquot containing the trace organics was removed within 10 seconds thus, ruling out direct oxidation of thiols at the counter electrode as a feasible explanation of disulfide formation. The working and counter electrodes could not be separated because volume was a critical issue regarding trace analysis and a 2-compartment cell could not meet the concentration limits imposed by the fluorescence detection.

The significance of the findings related to the reductive release and subsequent quantification is that the Au-S bond cleavage is an efficient method to release material. Solubility issues plague the material that is released since the local concentration of material is so high. To work around these issues, a more water-soluble probe is needed and to reduce the local concentration effects a mixed monolayer could be formed whereby the compound of interest is only deposited in low abundance. The remaining Au sites could be filled with an inactive compound that is very soluble such as cysteine.

This method would permit blockage and move away from the problematic suspended monolayer issues.

4.3 Summary of SAMs Experiment Results

The theoretical number of thiols that can be placed on an Au-surface is dependent on many factors, such as, surface morphology, size of molecule and functional groups of the molecule. For all of the experiments a theoretical number of 10^{14} molecules·cm^{-2} has been used based on monocrystalline studies involving alkyl thiols. The Au-glass slides are made by sputtering Au on a clean glass slide in a low-pressure chamber. This manufacturing process[136] produces Au-surfaces with roughness factors of 2 with variation between surfaces areas of less than 5%. The electrochemical release requires many more electrons than is necessary for a one-electron process suggesting either an inefficient cleavage process or a very low estimation of surface coverage. The latter is unlikely since that would require a roughness factor of about 200. On the other hand, the LC results show too little material is released. This result confirms the lack of non-specific adsorption of thiols since blank experiments in DMF revealed no peaks. In addition, non-specific adsorption would not consume electrons as faradic current but could result in an increase in capacitive current. Regardless, the results indicate incomplete removal of less than one monolayer of material from an Au surface.

Accepting the theoretical amount argument above applies to polycrystalline Au with a roughness factor of 2, why were so many electrons consumed in the reduction process? The capacitive current is unlikely to consume the excess of electrons because the capacitive trace is over in about 100 μs as compared to the applied reductive potential for 0.5 s. The likely candidate is the faradic current due to solvent impurities like water. Nonetheless, even if other electrochemical processes are occurring, the Au-S bond is first to break before any other processes can occur. In any event, the final electron count is immaterial as release concentrations will be controlled by electrode area and the use of mixed monolayer systems.

Immediately following the application of a reductive potential, all the Au-S bonds are cleaved to produce a suspended monolayer. If the original Au thiol interaction is

covalent, the reduction could result in homolytic bond cleavage producing a thiol radical, which would result in disulfide formation. Alternatively, if the Au thiol interaction were electrostatic in nature, the reduction would produce an Au atom and the thiolate. At negative potentials the electrostatic repulsion of the Au surface and a thiolate would be a much stronger force than the sum of the non-covalent interactions holding the monolayer in place resulting in a large amount of material released. The most likely explanation is a combination of both scenarios depending on the amount of water present, surface morphology and local ion permeability. Perhaps there is more disulfide produced in well-ordered regions with thiols abundant at defect or edge sites. However, the local concentrations of released material is high so the suspended monolayer is not "dissolved" by the end of the 0.5 s reductive pulse. Some material will have escaped to be detected by LC, which is best reflected in the release into DMF as a function of applied potential duration (Figure 4-7).

At the end of the reductive pulse, the potential is returned to 0 V. The processes that occur at this time are assumed the same as the adsorption mechanism described in Chapter 3. If the suspended monolayer is mainly disulfides and has not diffused too far from the electrode, recombination to the Au surface is likely. Instead, if the monolayer were a thiolate instead of a disulfide then recombination is even more likely. In both cases solvent and/or electrolyte would have to be "squeezed" from between the surface and the suspended monolayer. It is possible that the low release quantities found could be caused by the fast kinetics of re-adsorption. Although re-adosrption is a feasible justification in DMF, it is clearly not the case in water since the reductive potential causes a reorganized state that does not return to Au-S SAMs.

In conclusion, the low release of material does not matter for the application envisaged. The ion-channels that will ultimately be linked to the Au surface must have some hydrophobic components or else they will not function in a lipid bilayer. The channel release experiment must also be run in water so electron efficiency is not an issue as water reduction will occur. Extrapolating from the water release experiments, between 5% and 10% of the surface will be removed as thiolate and the remaining monolayer will adhere in an organized fashion to the Au-surface. As a result, the Au microelectrode will

have accomplished its task of delivering a small amount of material under spatial and temporal control.

4.4 Experimental

4.4.1 Electrochemical Desorption

A glass-gold slide (EMF Corporation, New York) is placed in its Teflon (See Chapter 3) in either acetonitrile or DMF containing 1 mL of either tetra-butylammonium hexaflorophosphate or $LiClO_4$ at 1 M concentration. A 1% agar bridge U-tube containing 2 M KNO_3 makes contact with the electrolyte and a 1 M KCl solution for the reference electrode. The counter electrode, positioned 0.5 cm above the planar Au, is a solid Au wire (0.5 mm diameter, Alfa Aesar >99.99% purity) with geometric area of 0.17 cm^2. The reference electrode is a AgCl coated Ag wire (0.5 mm diameter, Alfa Aesar >99.99% purity) placed in a 1 M KCl solution making ionic contact via U-tube salt bridge. The desorption waveform is created using CGWin software controlling a function generator (CompuGen 1100, Gage-Applied Instruments). The waveform is a one-cycle square wave starting at 0 V then to –2.0 V after 1s and holding at this level for times varying from 100μs to 40s then returning to 0 V. The output was acquired and analysed in the same manner as the capacitive measurements. After the desorption event, a 750 μL aliquot was immediately removed and stored in a sealed borosilicate glass vial for trace analysis by HPLC using conditions as described in Chapter 2.

4.4.2 Sampling Procedures

There were two procedures used for sample collection. The first was to use the same Au surface with a complete monolayer and add 1.0 mL of electrolye as described above. Immediately following the reductive cleavage, 750 μL was removed and placed into a sealed borosilicate glass vial. The cell and remaining sample was rinsed with Nanopure water and 100% EtOH then blown dry with a stream of nitrogen. This was done without replacement or disassembly of the electrochemical cell. An additional 1.0

mL of electrolyte was added and the desorption process, sampling process and washing process were repeated several times. All samples were collected and analysed on the same day. The pipette used was an adjustable volume pipette (100 μL to 1 mL) with disposable plastic tips.

The second procedure used fresh monolayers for each reductive desorption so cell disassembly was required between events. In addition, to prevent cross-contamination, the Teflon sleeve and Au counter electrode were boiled in 1.0 L of Nano-pure™ water for 2 hours between reductive cleavage experiments. The same aliquot volumes and procedures as described above were used.

Chapter 5 Ion-Channel Analysis

Recalling the design requirements established in Chapter 1, detailed mechanistic insight concerning the mode of action of artificial ion-channels is needed. Although, it may be possible to obtain such mechanistic detail with artificial systems, this has not yet been achieved. Therefore, one of the goals is to press towards detailing the mechanism of a simple synthetic ionophore. The system that had both available materials for study, and the potential for synthetic feasibility and structural control for future work, was Eggers' compounds[190] **5** and **6** shown in Figure 5-2. The conceptual design of compounds **5** and **6** evolved from the building blocks explored by Cameron[191]. The macrocyclic component shown in Figure 5-1 was synthetically investigated because it was proposed that this macrocycle would form one half of a bilayer-spanning molecule.

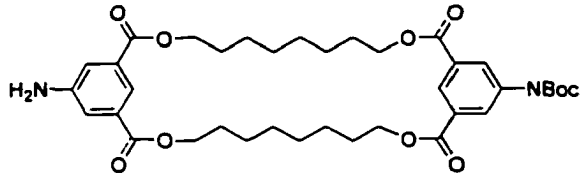

Macrocycle

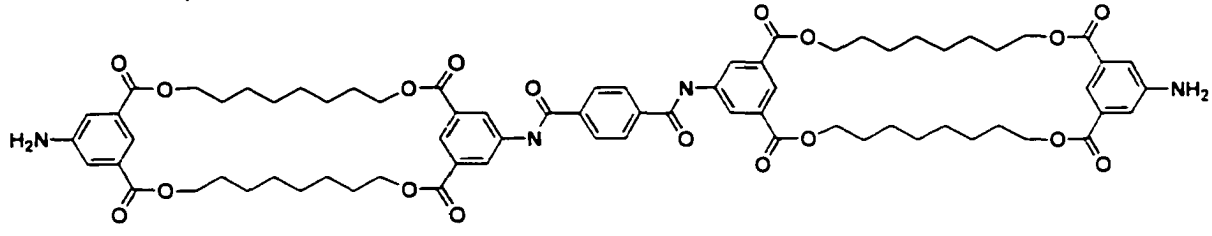

Bis-macrocycle

Figure 5-1. Channel forming compounds containing macrocycles.

The eventual synthesis of the bis-macrocyle shown in Figure 5-1 was achieved by Hu. In bilayer clamp and pH-stat experiments, the bis-macrocycle exhibited ion-channel characteristics, such as step conductance. As expected, since the molecule is centro-symmetric, no voltage-gated properties were observed. The main drawback to macrocyclic channels is the inherently low yields on the macrocyclisation step. As a result, non-centro-symmetric structural derivatives are unlikely. In the case of the bis-macrocycle of Figure 5-1, the very poor solubility limits its utility. A non-macrocyclic system is needed to achieve syntheic feasibility. To this end, the bis-macrocycle in

Figure 5-1 was broken apart at the two ends resulting in compounds **5** and **6** shown in Figure 5-2.

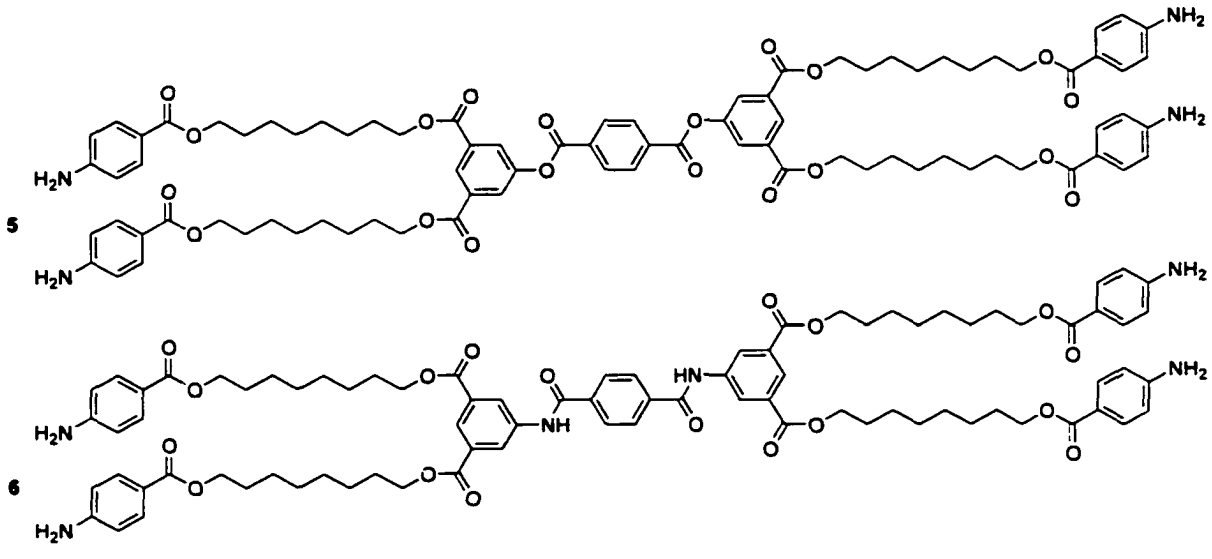

Figure 5-2. Structures of the four-arm compounds studied.

The details of the synthesis can be found in the recent M. Sc. Thesis of Eggers[190]. The structural features incorporated in **5** and **6** have evolved through several generations that have been documented by several theses[60,61,190-194]. The highlights of the structural features that are related to function are as follows. The aromatic amines are expected to protonate and align themselves at the water lipid interface. The molecules have been modeled and been shown to have appropriate length to span a bilayer (40 Å). The center aromatics were claimed by Eggers to cause aggregation by π-stacking and the amides of compound **6** was expected to stabilize aggregates and thereby prolong the channel lifetime. In addition, the ester or amide bonds are thought to stabilize the small amount of water that is layered between the two lipid layer leaflets thus positioning the central unit in the middle of the bilayer. The structural variations between **5** and **6** can address the question of whether hydrogen-bonding can play a role in stabilizing aggregates.

The goal of this chapter is to examine the details of channel formation and concentrate on answering whether these types of structures are suitable platforms to invest synthetic effort directed to voltage gating, for example, by alteration of one of the ends of the molecule, to introduce gating functionality or induce a permanent dipole moment.

5.1 Lipid Bilayer Experiment

Figure 5-3 describes the experimental set-up of a typical bilayer experiment. The bilayer chamber consists of a PVC cuvette holder with two chambers and a polystyrene or Delrin cuvette which fits into one of the chambers. A hole of 250 μm diameter was drilled through the cuvette and the cuvette was shaved to be as thin as possible around the hole. Before the bilayer was painted over the hole, it had to be primed. Priming consisted of adding lipid solution to both sides of the cuvette surrounding the hole with a paint brush and drying the solution with a stream of nitrogen. The bilayer chamber and cuvette were assembled and 5.0 mL of electrolyte was added to the chamber side and 2.6 mL of electrolyte was added to the cuvette side. It was important to ensure that no difference in solution height provided any hydrostatic pressure that could cause the bilayer to bulge. Electrical contact was made by a pair of AgCl wires. The AgCl wires were made by melting AgCl, dipping an Ag wire several times, and annealing the AgCl to coat the Ag wire. The AgCl wires were stored in 1 M HCl in the dark. The electrodes were checked for deterioration by placing them in the same electrolyte solution and checking junction potentials. A junction potential that was greater then 3mV or fluctuated meant new electrodes were necessary. The AgCl electrodes were usually stable for periods of up to 3 months. Junction potential variations can be a large problem during experiments so all experiments were conducted using a 1% agar, containing 2 M KCl, a glass U-tube bridge was used to connect the experimental electrolyte solution to 1 M KCl as shown in Figure 5-3. This setup produced very stable junction potentials. Stock solutions of 1.25 mg diphtanoylphosphatidyl choline in chloroform were prepared and stored at −12°C under argon in a desiccator. To prepare the lipid for bilayer experiment the chloroform was removed under reduced pressure in the dark. Decane (50 μL) was added to bring the concentration of lipid to 25 mg/mL. Once decane had been added to the lipid solution, reliable bilayers could only be formed for about 7-10 hours. The bilayer is then formed by painting a lipid-decane solution over an aperture (250 μm). Using the built in capacitance test, the instrument monitors the formation of the bilayer.

The decane/lipid solution covering the aperture is gradually removed by the brush to thin the membrane to a bilayer. During the thinning process, the bilayer is sometimes broken

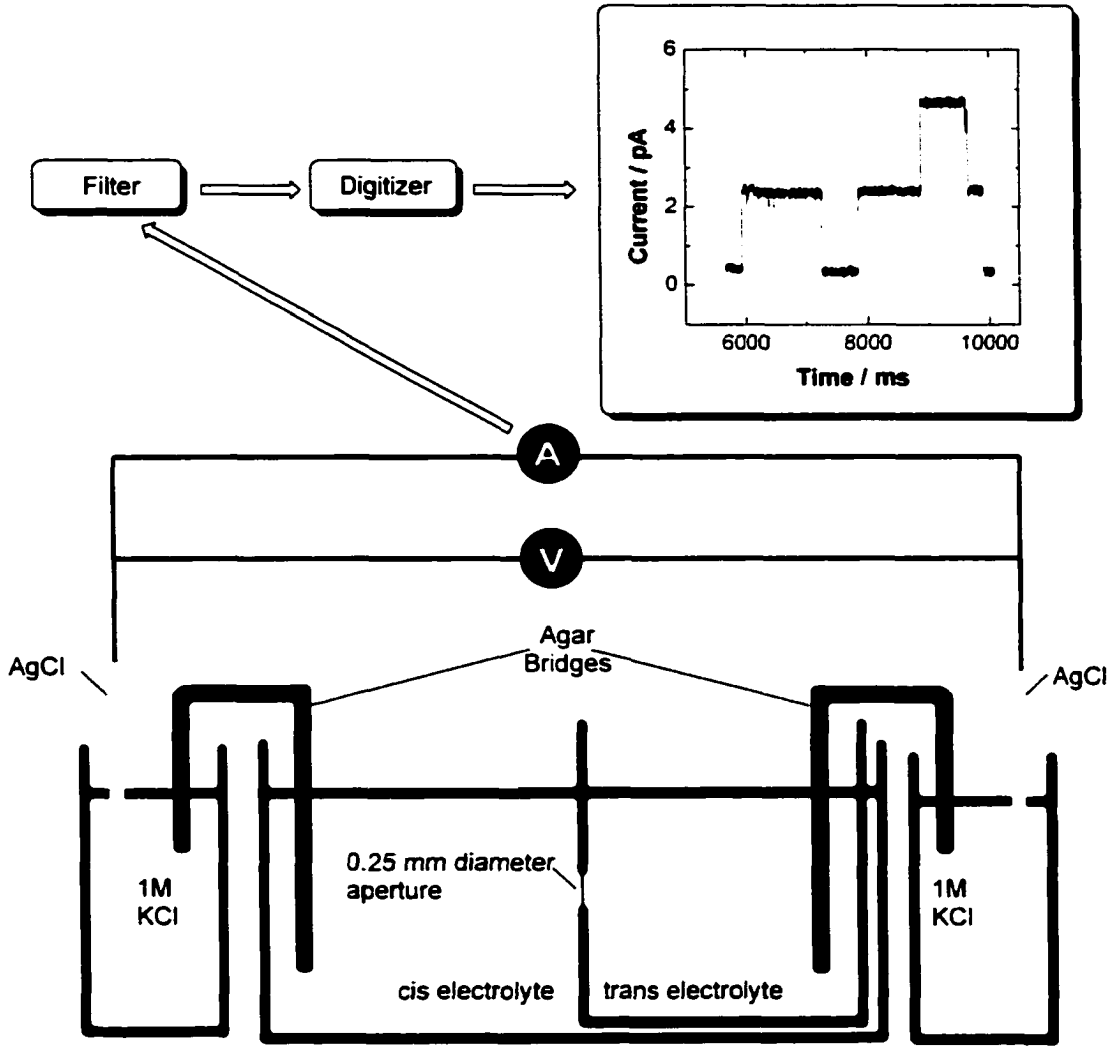

Figure 5-3. Diagram of bilayer clamp general set up.

at which time the electrolyte in the chamber side is quickly removed by syringe and re-injected with a flow rate of approximately 2-3 $mL \cdot s^{-1}$. This method usually results in a bilayer with good capacitance and little leakage. The capacitance test is summarized as follows. An input triangle wave of 100 Hz frequency with amplitude of ±10 mV is directed to the headstage. The output signal is integrated and displayed as a 100 Hz square wave. The peak to trough height of the resulting square wave is indicative of the

capacitance of the bilayer. The thinning of the bilayer can be directly monitored since the thickness of the membrane is related to capacitance by the following equation.

$$C = \varepsilon_0 \varepsilon A d^{-1}$$

Where C is the capacitance, ε_0 the permittivity in vacuum, ε the dielectric constant of the lipid core, A is the membrane area and d is the thickness. Acceptable capacitance values for use of the bilayer in this apparatus are between 180 and 200 pF. In addition to the capacitance test of bilayer formation, a ±100 mV potential was applied to check for current leakage. Leakage exhibits itself by conducting currents at an appreciable level (greater than 0.25 pA) and burst events. Burst events are believed to be caused by bilayer breakdown at applied potentials and cannot be used in ion-channel assays. All experiments utilized bilayers that were apparently stable at ±100 mV for periods of 20 minutes or more.

5.2 Analysis of Idealised Channel Behaviours

The analysis of single channel records was done with Origin 6.1 (OriginLab Corporation). Consider the idealized channel activity shown in Figure 5-4. Calculation

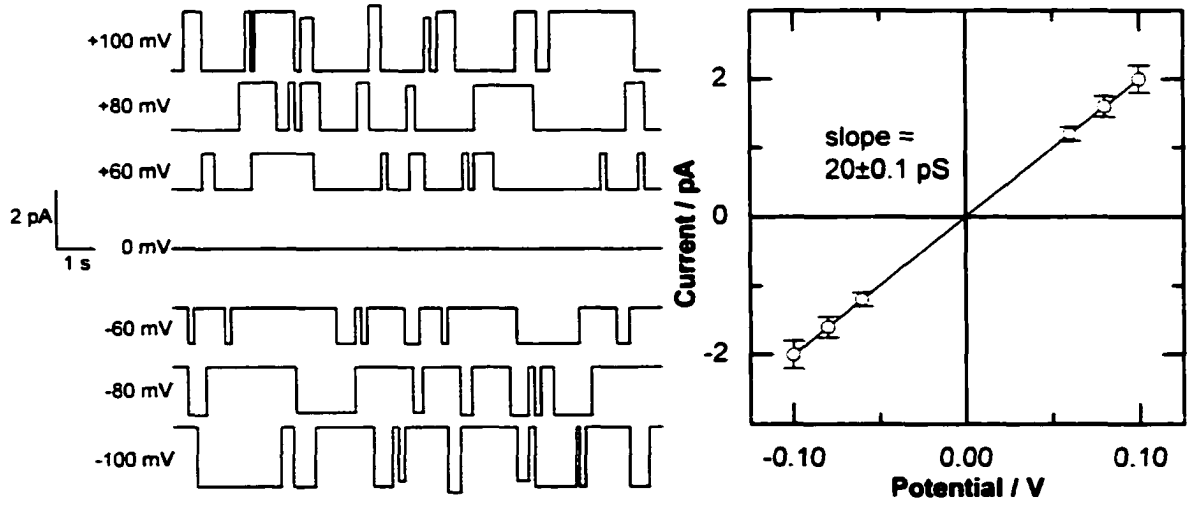

Figure 5-4. An idealized I-V plot using an average of single-channel openings.

of conductivity as a function of applied potential is done on records where only first level openings were observed. The current peak of each opening was averaged and the

standard deviation calculated from a minimum of ten individual openings at each set potential. The slope of the resulting plot, with Y-axis as current in pA and X-axis as set potential in V, yields conductance in pS. If the fit line passes through the origin of the plot and is linear then the channel is described as exhibiting Ohmic behaviour. Alternatively, if the plot is strongly non-linear, the channel is described as rectified or voltage-gated. For example, a rectified channel might show a conductance of 10 pS at – 100 mV and 40 pS at +100 mV.

Further characterisation of ion-channels involves cumulative statistics. The data file must include several step-conduction levels (1 to 4 is typical) and the currents of each step are placed into the bins of a histogram. The bin width is arbitrarily adjusted to obtain counts into the thousands. Sampling rate and filtering frequency also play a role in bin width selection due to aliasing effects. An idealized raw data trace and its associated histogram plot is show in Figure 5-5. The raw data trace shows uniform step conductance changes of 20 pS. The resulting histogram can provide information regarding the mechanism of channel formation. Each distribution of channel step conductance is fit to a Gaussian distribution. The width of the Gaussian distributions comes from two sources. First the noise of the instrument, which will be constant in each level and the second, the molecular changes that occur within one conducting structure. The Δi between each Gaussian peak is 2 pA, indicating that each active channel structure is similar in structure and conductivity is interpreted as multiple copies of the same conducting structure inserting. A model compound, such as gramicidin, shows a Gaussian distribution surrounding each step level and the separation between Gaussian peaks is uniformly incremental similar to the ideal case in Figure 5-5. Mechanistic insight can be gained from the results of these plots since every channel opening produces the same conductance so the channels must make the same sized pore for ion transport.

Alternatively, alamethicin, shows different results in its histogram plot. It is a channel which functions in an aggregate whose mode of action is akin to staves in a barrel as shown in Figure 5-6. Each monomer addition to an aggregate results in a non-uniform increase in step conductance. The step conductance follow the trend plotted in Figure 5-7 whereby the pore size, which is proportional to conductance, increases non-

linearly with monomer number. The calculations are based on a 4 Å stave radius as tightly packed as possible as illustrated in Figure 5-6. The minimum barrel size consists of 3 monomers and the pore size is the calculated largest circle that can fit into

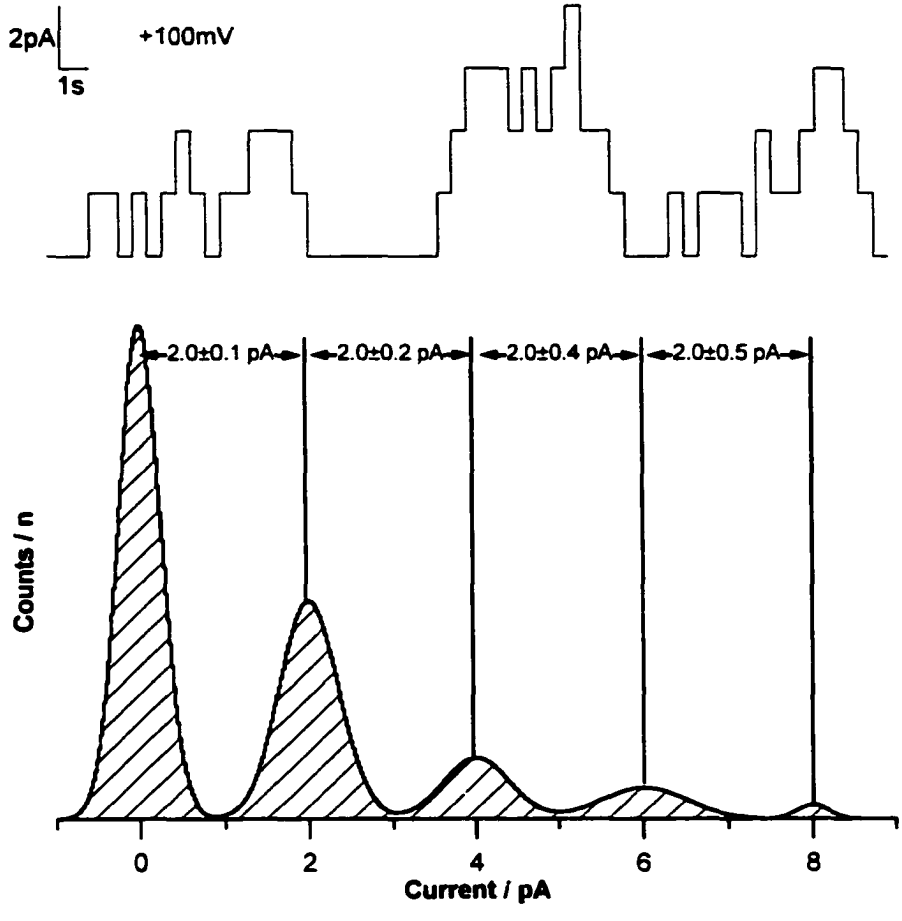

Figure 5-5. An idealized current-time trace exhibiting uniform steps of 2 pA and its associated histogram plot.

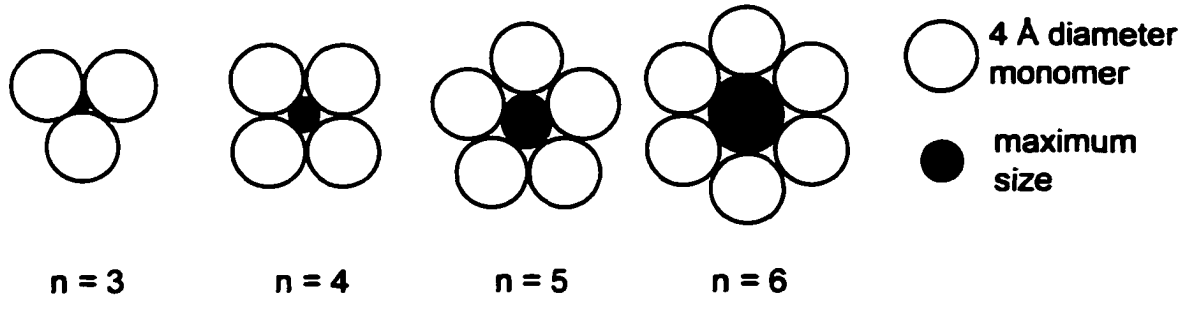

Figure 5-6. Barrel-stave model showing maximum pore size in relation to the number of monomer units.

the aggregated model. A histogram plot results in small increases in step conductance for the first few where n is low, and addition of more monomers results in a larger incremental pore size thus a larger conductance value. The plot in Figure 5-7 is theoretical, and in practice if an aggregate of more than 15 were to form, the bilayer would most likely collapse.

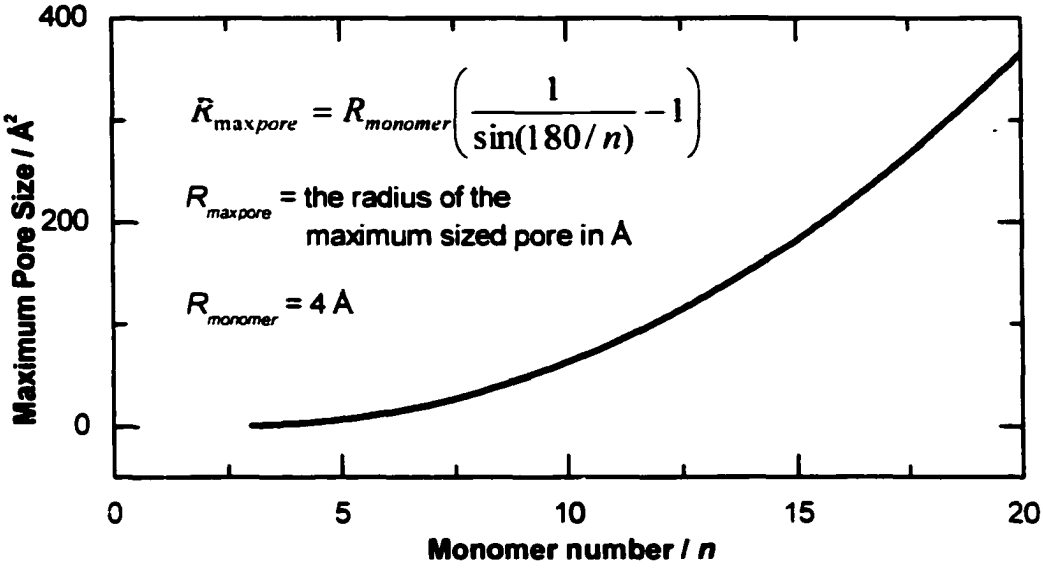

Figure 5-7. Plot of maximum pore size versus number of equally sized monomer units in the barrel-stave model of ion-channel formation.

The probability of a channel conduction level occurring can be predicted by using the following formula.

$$P_{On} = \frac{A_n}{\sum_{i}^{0} A_i}$$

Where P_{On} refers to the probability that level n is open. A_n is the Gaussian area of level n and the denominator is sum of all observed levels including the closed baseline level. The problem with this equation is that the concentration of inserted channel plays a major factor in determining which level is the most probable and as such reported probabilities are meaningless if not reported with an absolute concentration and lipid composition. Histograms of this type are described in Section 5.4.

In addition to histograms of conductance states, histograms of channel lifetimes are a valuable tool to describe single channel activity. The raw data for this type of analysis requires many (>10 000) single level openings, unlike the multiple open states

described above, and the base line must be extremely stable for the entire duration of the trace. The duration of each channel opening is abstracted and placed into a new file. The list of durations is binned into a histogram, which is then fit to the following formula.

$$i(t) = A_0 \exp\left(-\frac{t}{\tau}\right)$$

i(t), is the current at time t, A_0 is the pre-exponential factor and τ is the lifetime. An example trace and associated plot is included in Figure 5-8. The plot generated in this analysis is called a probability density function (pdf). Implied from the equation

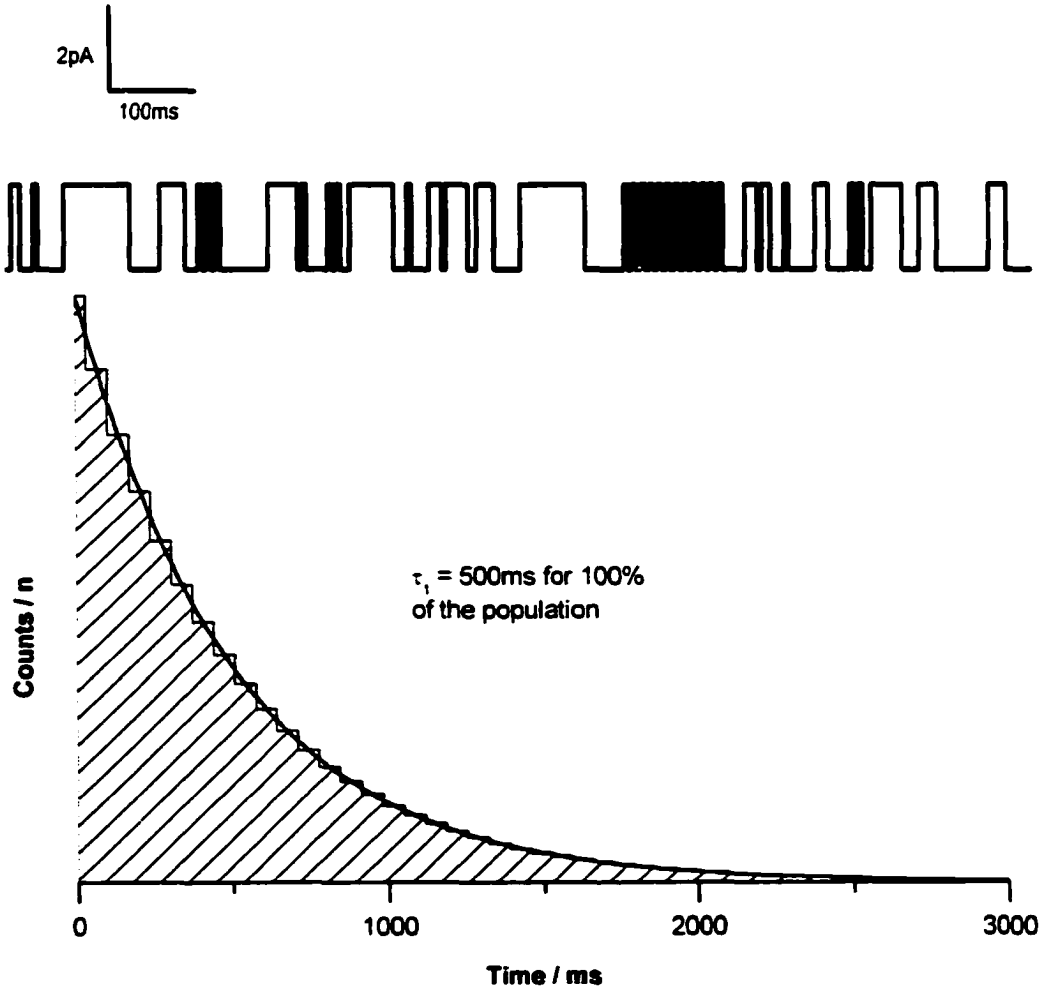

Figure 5-8. Idealized single-channel data and its associated single-channel lifetime histogram.

above is that short-duration events will be encountered more frequently than long-lived durations. An exponetial decay is expected for lifetime of ion-channels under stochastic control and the behaviour can be rationalized by thermal energy. Thermal energy causes

the bonds to vibrate, and the molecules rotate or collide at a very high frequency ($k_BT/h \approx 6\times10^{12}$ sec^{-1}). An open channel represents a shallow energy minimum, thus collisional or vibrational energies are sufficient to "close" the channel via dissociation or reorganization of the components. At longer open channel durations, the number of possible collisions, vibrations or reorganizations increases. As a result, fewer channels remain open at longer durations since only one detrimental event is necessary to close the channel.

5.3 Single-Level Conductance and Ion-Selectivity Study

Compounds **5** and **6** were indistinguishable by direct current trace observation. The record shown in Figure 5-9 is an example of **6** at +200 mV. Notice the lack of any unique identifiers that could be used to differentiate either compound. The expanded region illustrates the long-lived as well as the discrete short-lived channel lifetimes.

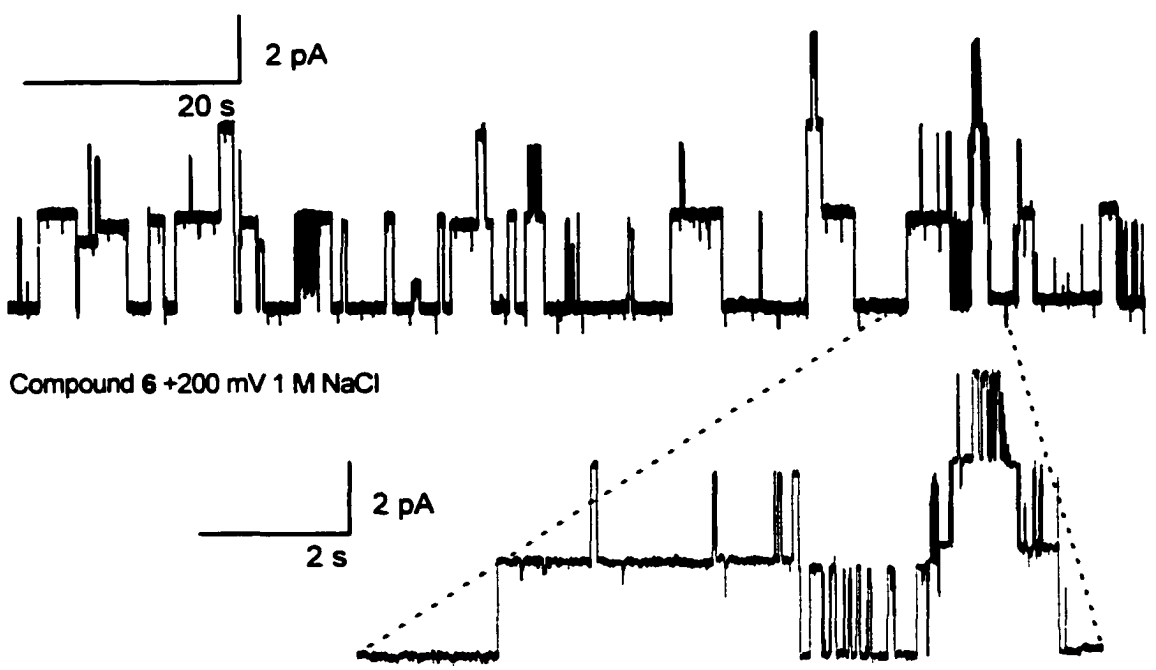

Figure 5-9. Example current trace for compound 6 in DiPhyPC at +200 mV in 1 M NaCl.

Single-channel activity was recorded for potentials ranging from −120 mV to +120 mV stepping by 20 mV is shown in Figure 5-10 for 6.3×10^{-8} moles of compound **5**

for two different electrolytes. The average step conductance for a minimum of 10 opening events was calculated along with its standard deviation, indicated by the Y-error

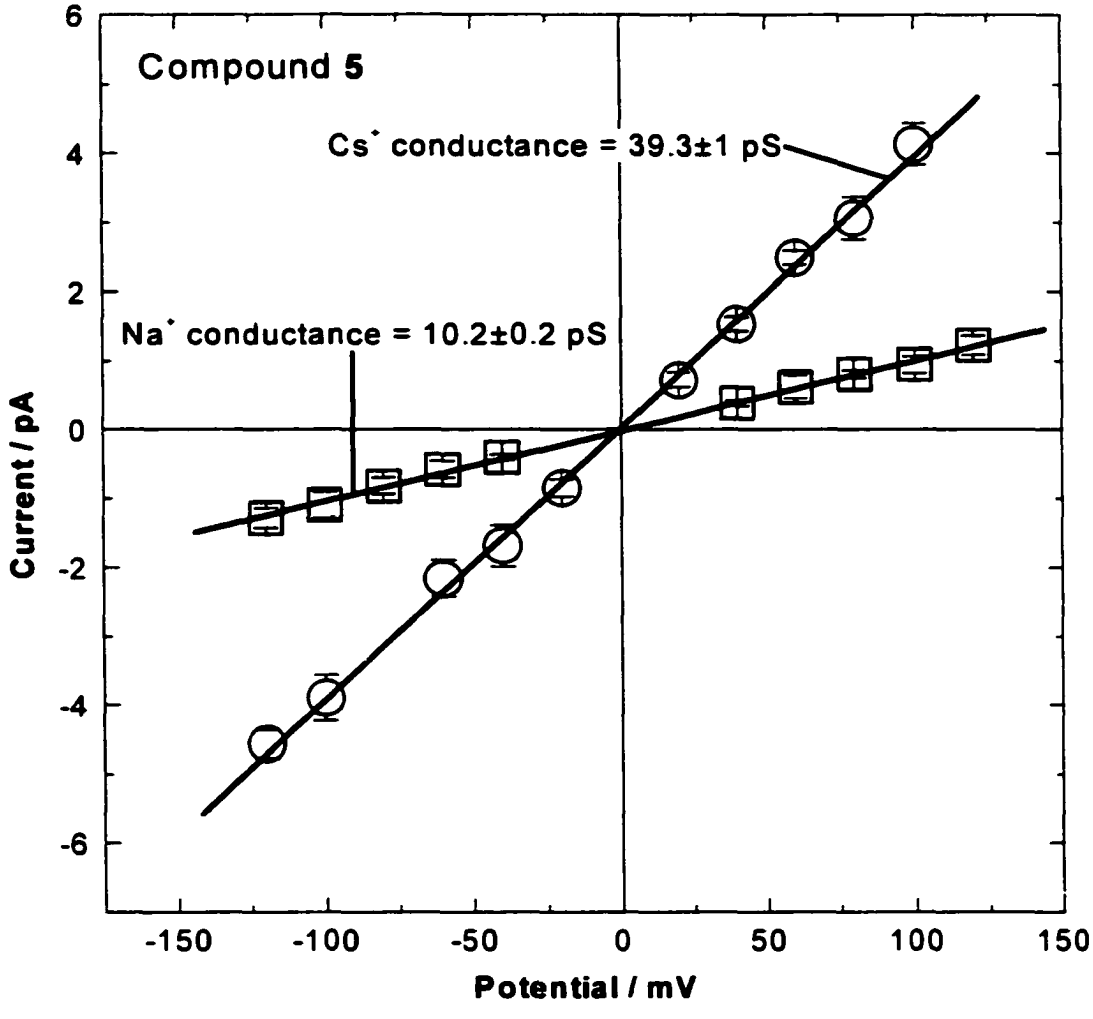

Figure 5-10. Conductance of 6.3×10^{-8} moles of 5 in diPhyPC (1 M CsCl or 1 M NaCl electrolytes).

bars of Figure 5-10. Conductivity was calculated as described above and Ohmic behaviour for both compounds was observed, indicating ion transport is not rectified. However, selectivity between cations was observed. A cation-selective channel is defined as a channel that permits a greater flux of one cation over another. As Figure 5-10 shows channels from compound **5** have a conductance of 39.3±1 pS with CsCl and a conductance of 10.2±0.2 pS with NaCl. In addition, Figure 5-10 provides a clear example of a channel showing non-voltage-gated behaviour. Figure 5-11 shows channels

of compound **6** to have a specific conductance of 38.9±0.9 pS with CsCl ions and a conductance of 10.3±0.4 pS with NaCl ions.

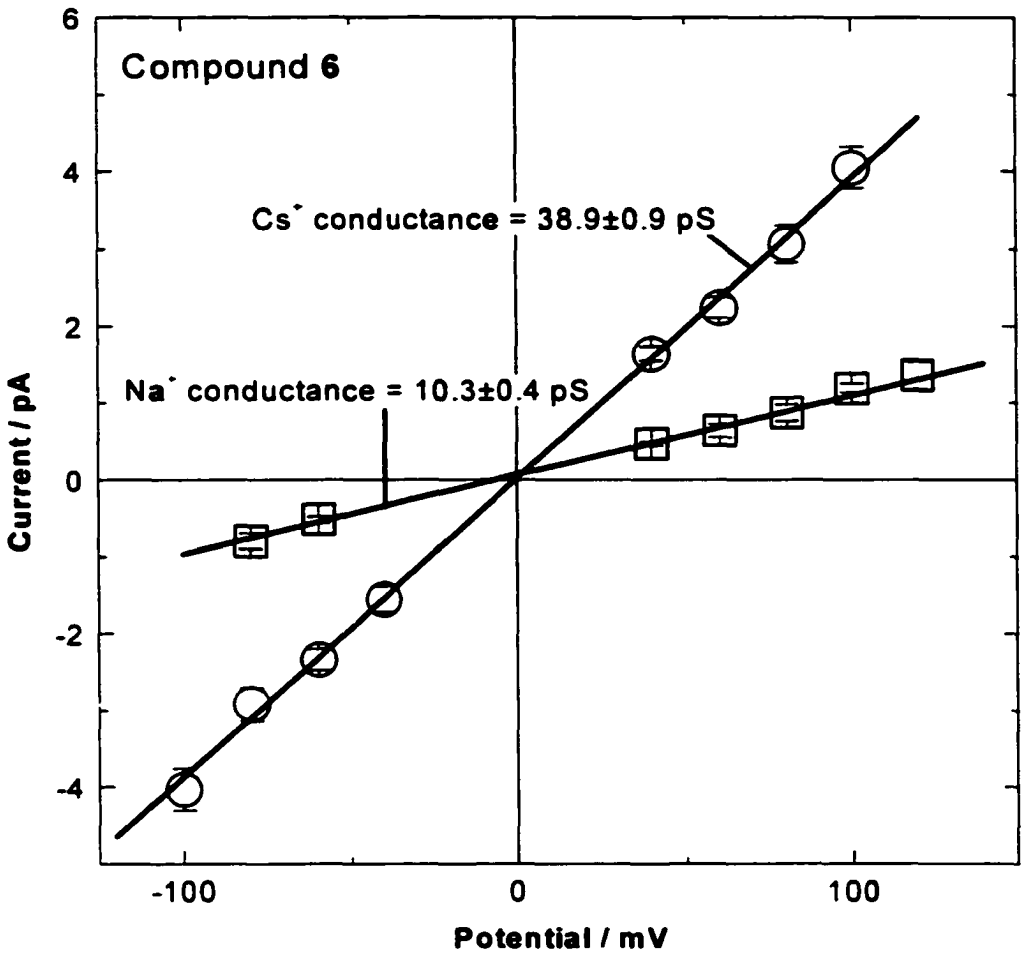

Figure 5-11. Conductance of 3.8×10^{-8} moles of 6 in diPhyPC (1 M CsCl or 1 M NaCl electrolytes).

Both the selectivity and the magnitude of the conductance of **6** are in close agreement with other synthetic ion-channels from the Fyles group[24,48,49]. The principle finding is that the structures of the compounds play only a minor role in determining ion selectivity. This selectivity sequence correlates with the hydration energy of cations in water, which suggests that a bilayer spanning aqueous pore is formed allowing transport of cations without specific interaction with **5** or **6**. This order of cation selectivity suggests the greatest energy barrier for transport lies in partially desolvating the cation before allowing transport across the lipid bilayer. The magnitude of the conductance for

both compounds in 1 M CsCl is about 40 pS compared to 77 pS for gramicidin under the same conditions[11]. At the very least, compounds **5** and **6** have good ion transport rates. In an attempt to quantify the selectivity, a further study was undertaken to determine the permeability ratio of one ion over that of another. There are two categories to compare ion selectivity: one is cation/anion and the other is cation/cation selectivity. Both categories use the Goldmann-Hodgkin-Katz equation[1] shown in Equation 5-1.

$$V_{rev} = \frac{RT}{F} \ln\left(\frac{P_{Na}\gamma_{Na}[Na^+]_{trans} + P_{Cs}\gamma_{Cs}[Cs^+]_{trans} + P_{Cl}\gamma_{Cl}[Cl^-]_{cis}}{P_{Na}\gamma_{Na}[Na^+]_{cis} + P_{Cs}\gamma_{Cs}[Cs^+]_{cis} + P_{Cl}\gamma_{Cl}[Cl^-]_{trans}} \right)$$

Equation 5-1. Goldmann-Hodgkin-Katz equation.

V_{rev}, the reversal potential, is defined as the point in a current-voltage plot where there is no net ionic current in the presence of a concentration gradient. P_X is the permeability of the specified ion (X) measured in mol·cm^{-1} and γ is the activity coefficient. Values of γ were calculated from the empirical Debye-Hückel equation of Morf[195]. All concentrations are measured in mol·L^{-1}. The subscripts *cis* and *trans* refer to the two compartments as illustrated in Figure 5-3. R, T and F are the gas constant, temperature in Kelvin and Faraday constant, respectively. Determination of the cation/anion permeability ratio is done by using the same electrolyte at two different concentrations in each compartment, which, in the case of CsCl concentration gradient, simplifies Equation 5-1 to Equation 5-2.

$$V_{rev} = \frac{RT}{F} \ln\left(\frac{P_{Cs}\gamma_{Cs}[Cs^+]_{trans} + P_{Cl}\gamma_{Cl}[Cl^-]_{cis}}{P_{Cs}\gamma_{Cs}[Cs^+]_{cis} + P_{Cl}\gamma_{Cl}[Cl^-]_{trans}} \right)$$

Equation 5-2. Simplification of Goldmann-Hodgkin-Katz equation for cation:anion selectivity.

Direct substitution of the experimentally derived V_{rev} yields the cation/anion permeability ratios as shown in Figure 5-12 and the results are summarized in Table 5-1. Notice in Figure 5-12 that the curvature of the lines is indicative of non-Ohmic behaviour which is normal for ion-channels separating two different concentrations of electrolytes since the experiment is inherently asymmetric with respect to salt concentration. The point at which each best-fit binomial crosses the X-axis, as specified by the arrows in Figure 5-12, is the point of no net ionic current, also known as V_{rev}. The same experiments were carried out with compound **6** and results are shown in Figure 5-13.

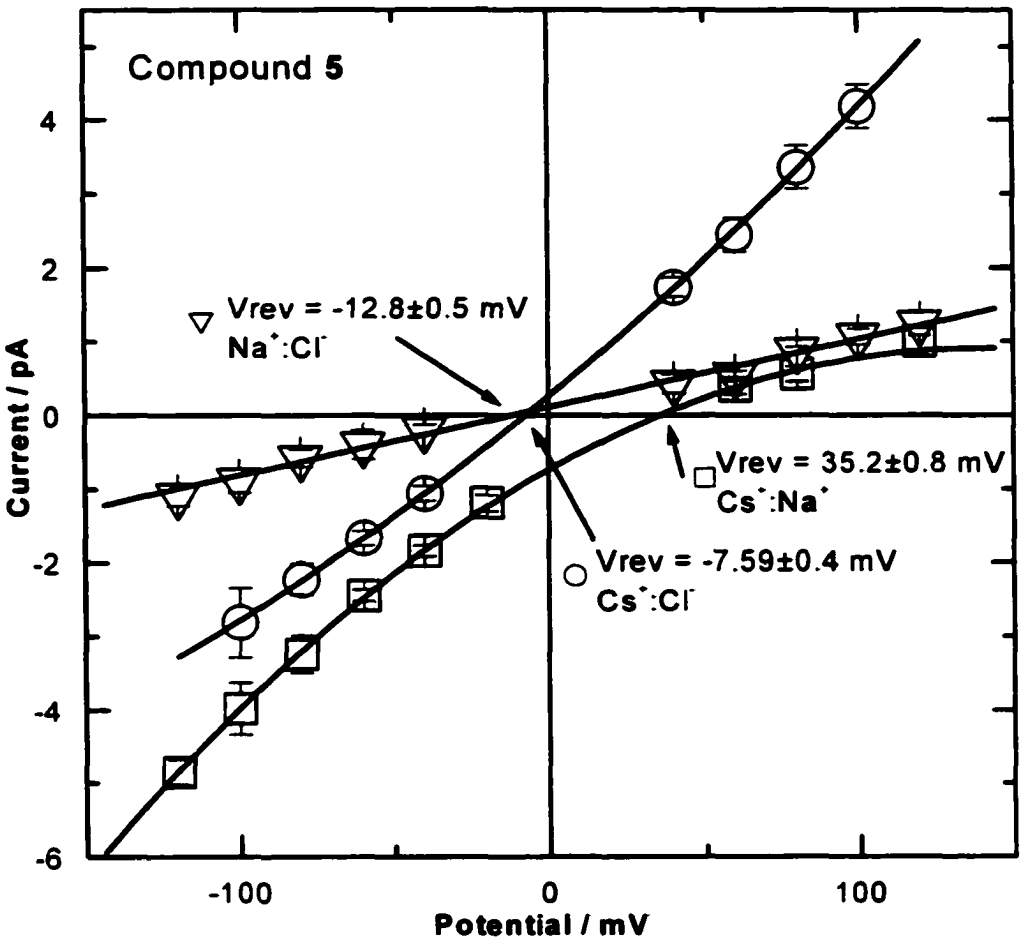

Figure 5-12. Reversal potentials for compound 5.

The second category of cation/cation selectivity simplifies Equation 5-1 to Equation 5-3. The assumption made in this simplification is that all the cationic

$$\frac{P_{Na}}{P_{Cs}} = \exp\left(\frac{V_{rev}F}{RT}\right)$$

Equation 5-3. Simplification of Goldmann-Hodgkin-Katz equation for cation:cation selectivity.

permeability terms are much greater than the anionic terms resulting in all terms containing Cl^- being set to zero.

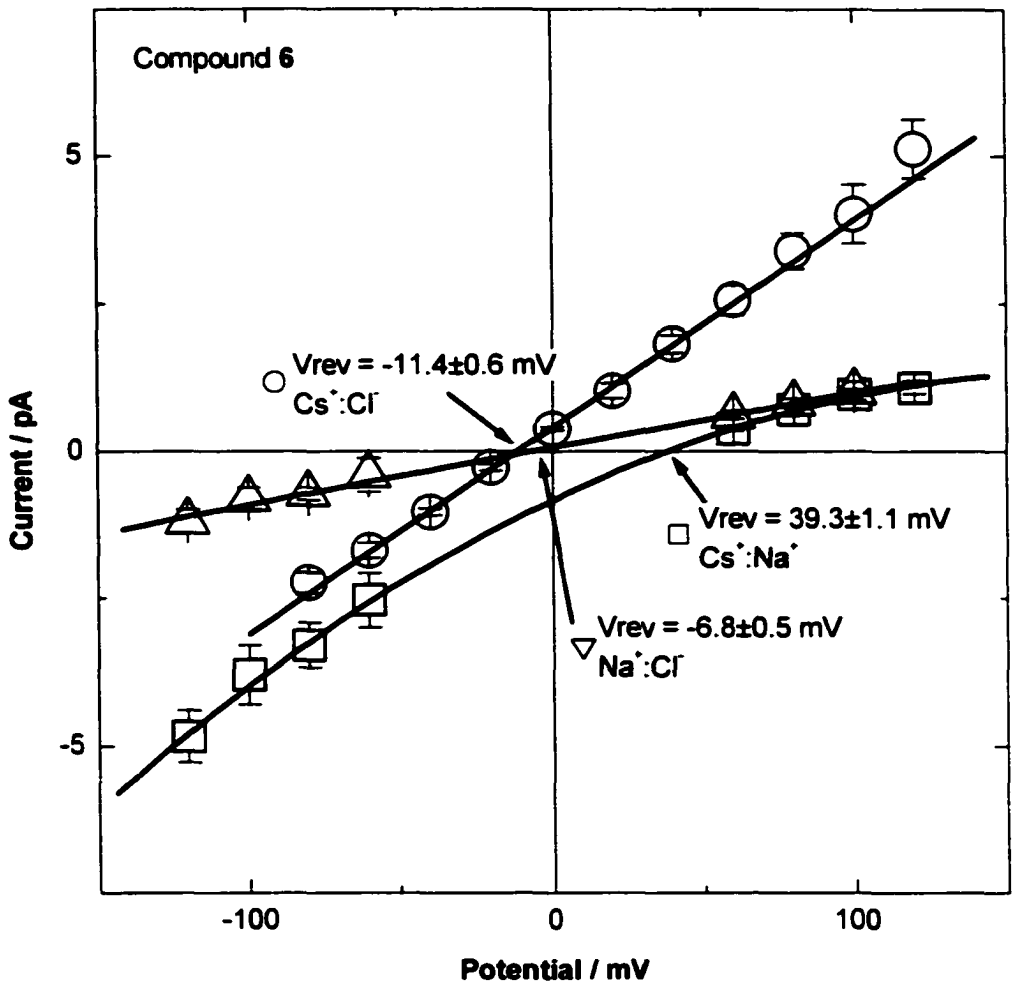

Figure 5-13. Reversal potentials for compound 6.

Cation/cation selectivity can also be calculated by taking the ratio of conductance for the two ions. A summary of reversal potentials, conductance and ion selectivity is included in Table 5-1. Based on the summary below there is no significant experimental difference with respect to ion conductance and selectivity between **5** and **6**.

Table 5-1. Summary of ion conductance and selectivity for compounds 5 and 6.

Compound	Na^+ conductance (pS)	Cs^+ conductance (pS)	Ratio of conductance	Cs^+/Na^+ Permeability ratio	Cs^+/Cl^- Permeability ratio	Na^+/Cl^- Permeability ratio
5	10.2 ± 1.0	39.3 ± 0.9	3.9	4.7 ± 1.0	7.5 ± 0.9	3.1 ± 0.5
6	10.3 ± 0.2	38.9 ± 0.4	3.8	5.2 ± 0.8	7.2 ± 1.0	2.1 ± 0.9

5.4 Multiple Level Opening Analysis

The histogram of conductance levels for compound **5** is shown in Figure 5-14. The average peak-to-peak separation of the Gaussian distributions is 3.4±0.7 pA when the histograms are binned at 0.5 pA. The separation between peaks is uniform, within experimental error, which suggests an ion-channel that does not act as an aggregate of

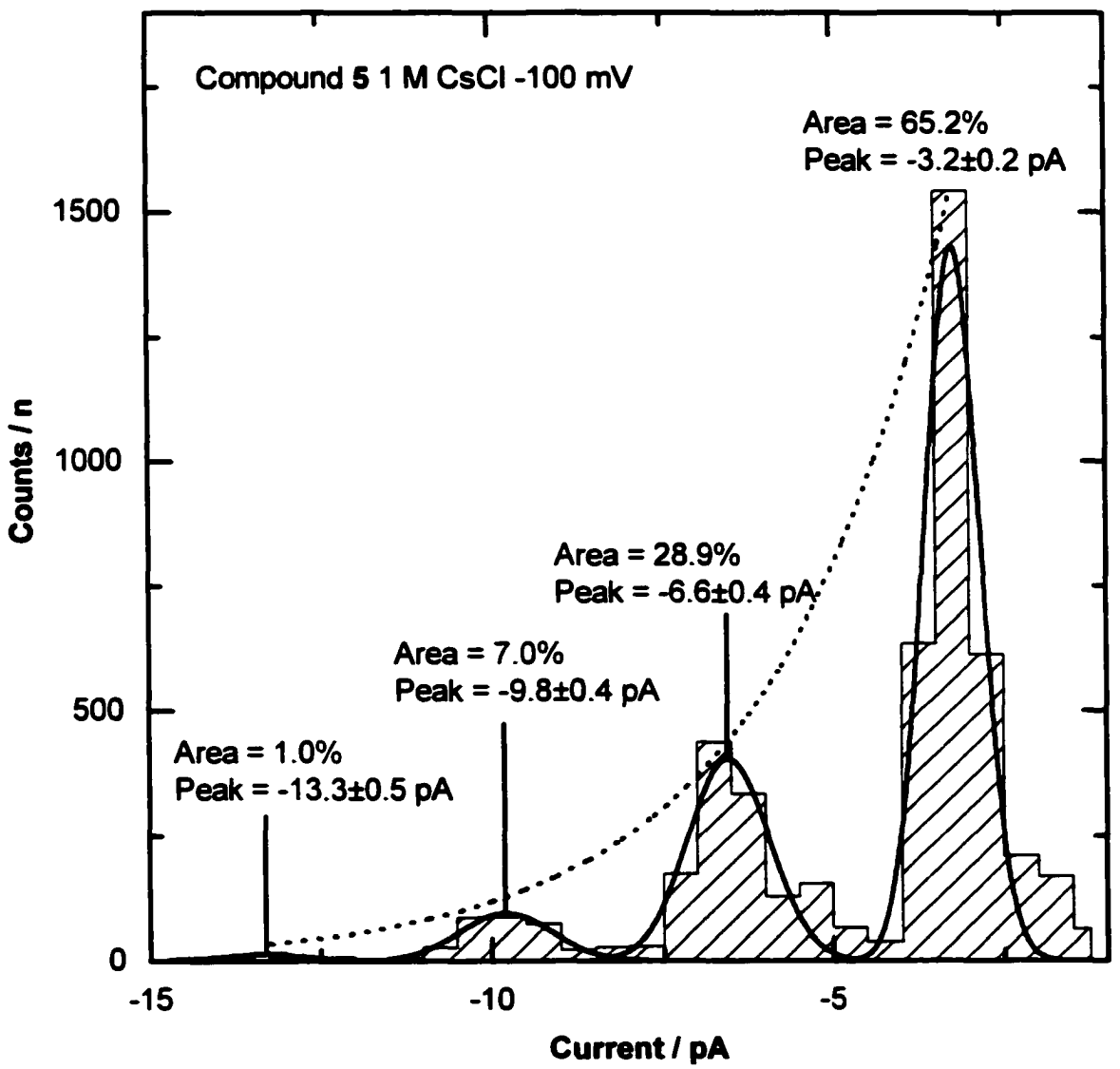

Figure 5-14. Histogram of conductance levels of compound 5 at –100 mV in 1M CsCl with a bin width of 0.5 pA.

increasing size, such as alamethicin. Or, if it does act as an aggregate only one of the aggregate structures is conductive. The peak representing the "closed" system (pA = 0) was not included since its area was much larger than the area shown in Figure 5-14 and made the other peaks difficult to observe. The peak areas are included to show that compound **5** exhibits typical behaviour at multiple opening levels since the areas decrease exponentially with step level, as shown by the fit line in Figure 5-14.

The histogram of conductance level of compound **6** is shown in Figure 5-15. The Gaussian peak-to-peak average separation is 4.1±1.1 pA which does fall within

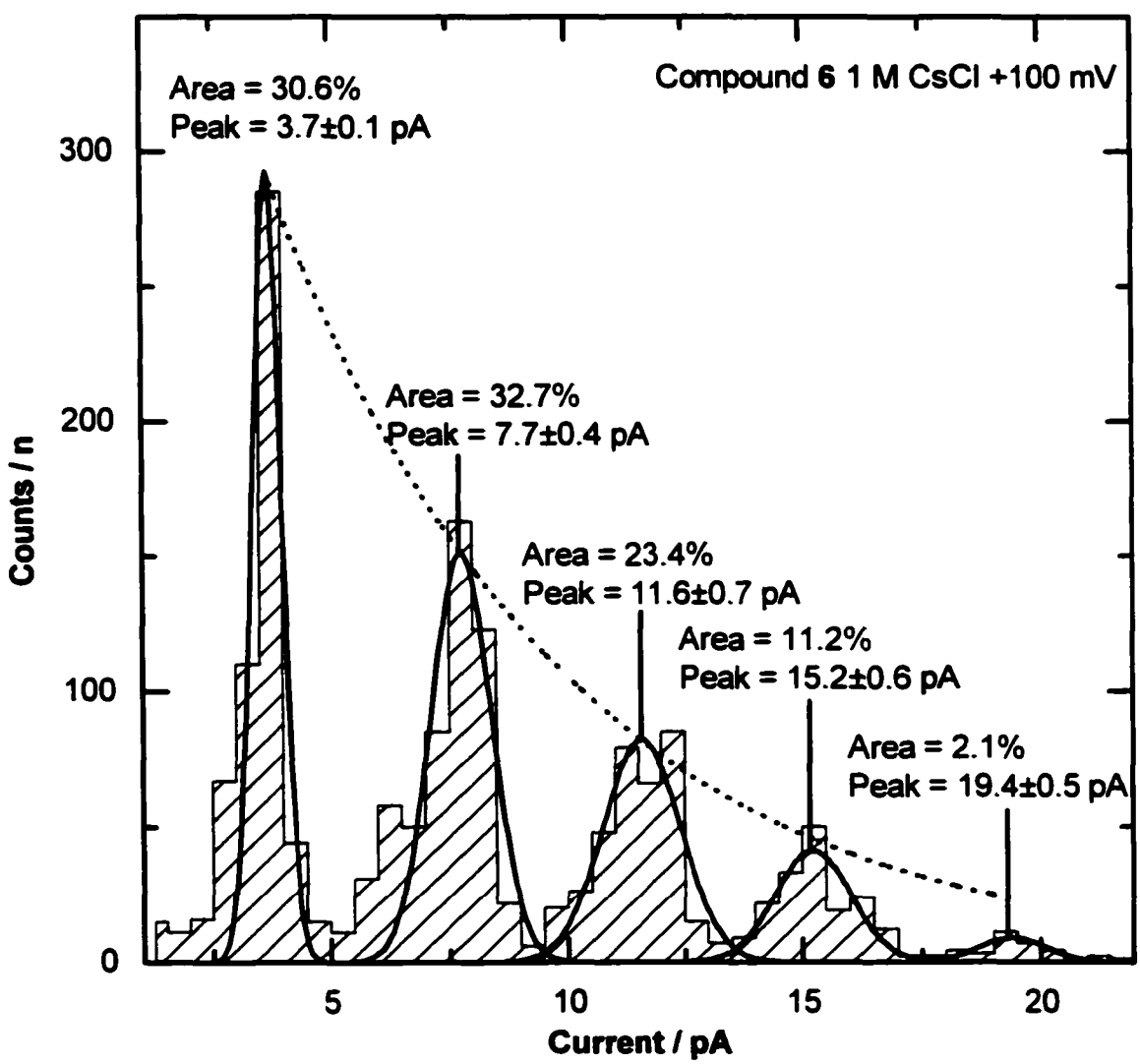

Figure 5-15. Histogram of conductance levels of compound 6 at +100 mV in 1 M CsCl with a bin width of 0.5 pA.

experimental error of compound **5** but has a slightly larger step conductance change. As with compound **5**, the differences between peak centers, as indicated on plot, are uniform within experimental error suggesting the same mode of action as compound **5**. The major difference between the plots shown in Figure 5-14 and Figure 5-15 lies in the conditions of the experiment. Compound **5** was placed at −100 mV whereas compound **6** was placed at +100 mV for the collection period. However, comparison between channels under different conditions is still valid because the channels exhibit non-rectified Ohmic behaviour as proven in Figure 5-10 and Figure 5-11.

The different conducting states within one level, as depicted in Figure 5-16, are unique to the Fyles family of ion-channels. The three sub-levels, labeled a, b and c on Figure 5-16, are characteristic of compounds **5** and **6**. This behaviour allows for a more thorough analysis of multiple steps because multi-level uniform step conductance cannot normally be analyzed at the single channel level because a step change in conductance

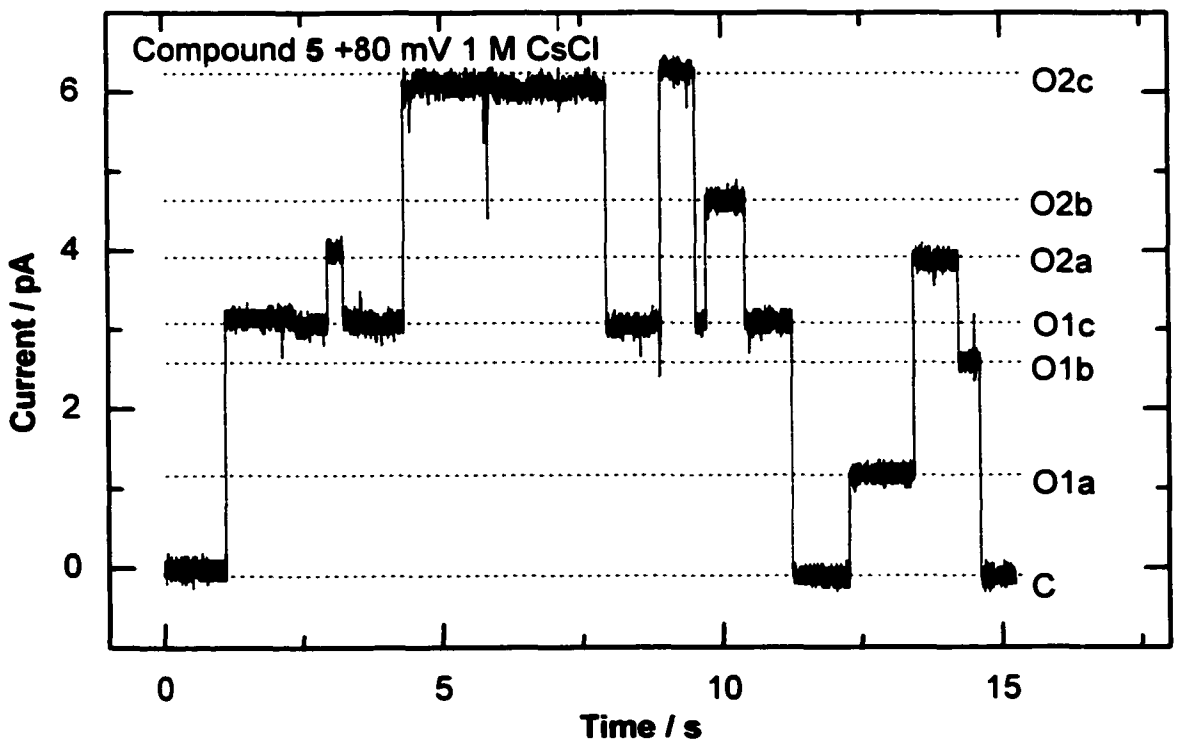

Figure 5-16. A current trace of 5 showing multiple different conducting open states within one level.

cannot be associated with a single channel. The reason is that beyond single step events there is no way to determine whether or not the channel that just closed was the same one

which just recently opened or some other long-lived channel that finally closed. During multi-level events, compounds **5** and **6** periodically allow the specific determination of which channel closed to provide more statistical information regarding lifetime of channel openings.

In addition, the bin size selection has a dramatic effect on interpreting histogram plots. According to Figure 5-16, there should be many sublevel openings within one level but neither of the histograms presented show any indication

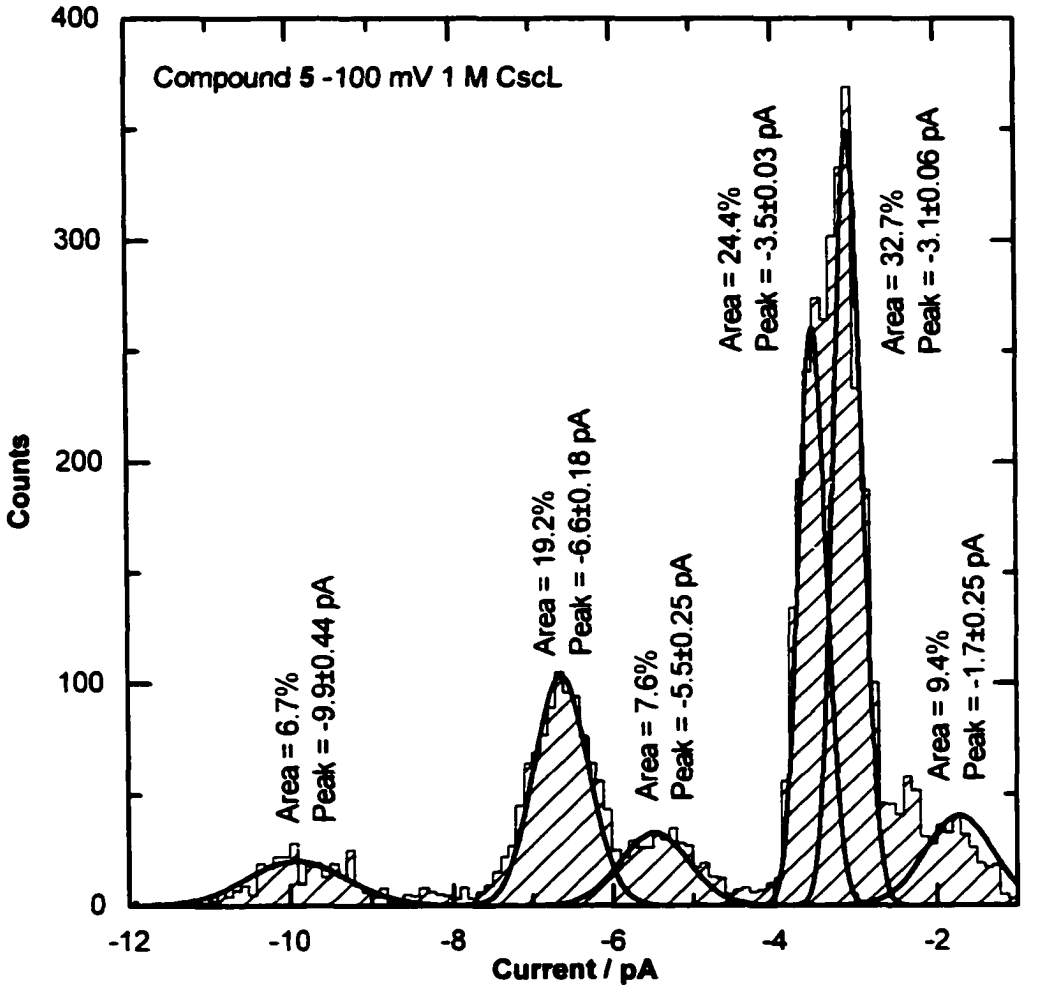

Figure 5-17. Histogram of conductance levels of compound 5 at -100 mV in 1 M CsCl with a bin width of 0.1 pA.

of sub-level openings. In order to extract information regarding the probability of getting sub-level openings, a smaller bin size is required. The plot shown in Figure 5-17 is a re-binning of the data used to create Figure 5-14. Immediately obvious is the emergence of

distinct subpopulations within one level. Likewise, the plot shown in Figure 5-18 is a re-binning of the data used to create Figure 5-15. The mechanistic interpretation of sub-level openings is puzzling. Since each peak does fit to a Gaussian distribution, the sub-level is most likely a stable ion-conducting state where the conformation changes within the structure bring about the Gaussian distribution. Again, mechanistic speculation cannot be undertaken until aggregation numbers are known. In summary, the conductance histogram plots do not provide a handle with which to uniquely identify each compound.

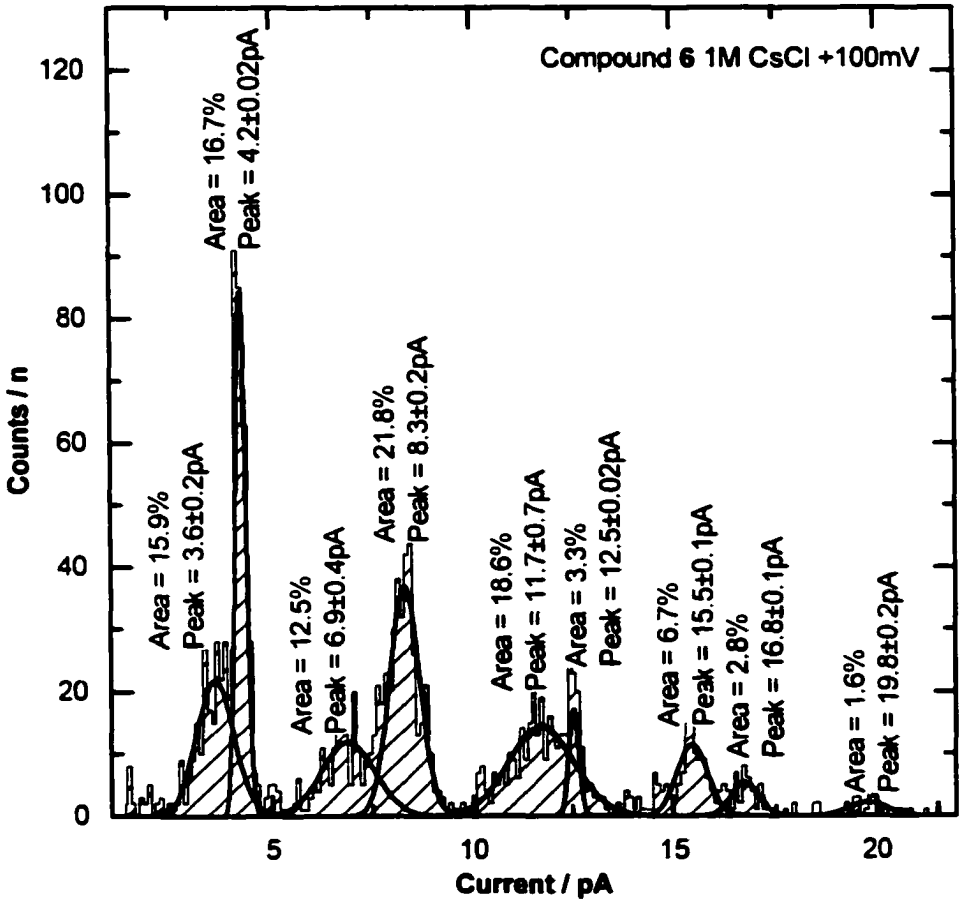

Figure 5-18. Histogram of conductance levels of compound 6 at +100 mV in 1 M CsCl with a bin width of 0.1 pA.

5.5 Lifetime Analysis

The next cumulative statistics approach was to measure lifetimes of channel opening events. The guidelines for the analysis were that a current trace with very little baseline drift was needed with not less than 5 000 single channel events. The difficulty was to adjust the concentration of channel to the point where single opening and closing events were frequent with few double opening events. No double opening events were used in the derivation of channel lifetimes, as an algorithm to account for sub-level

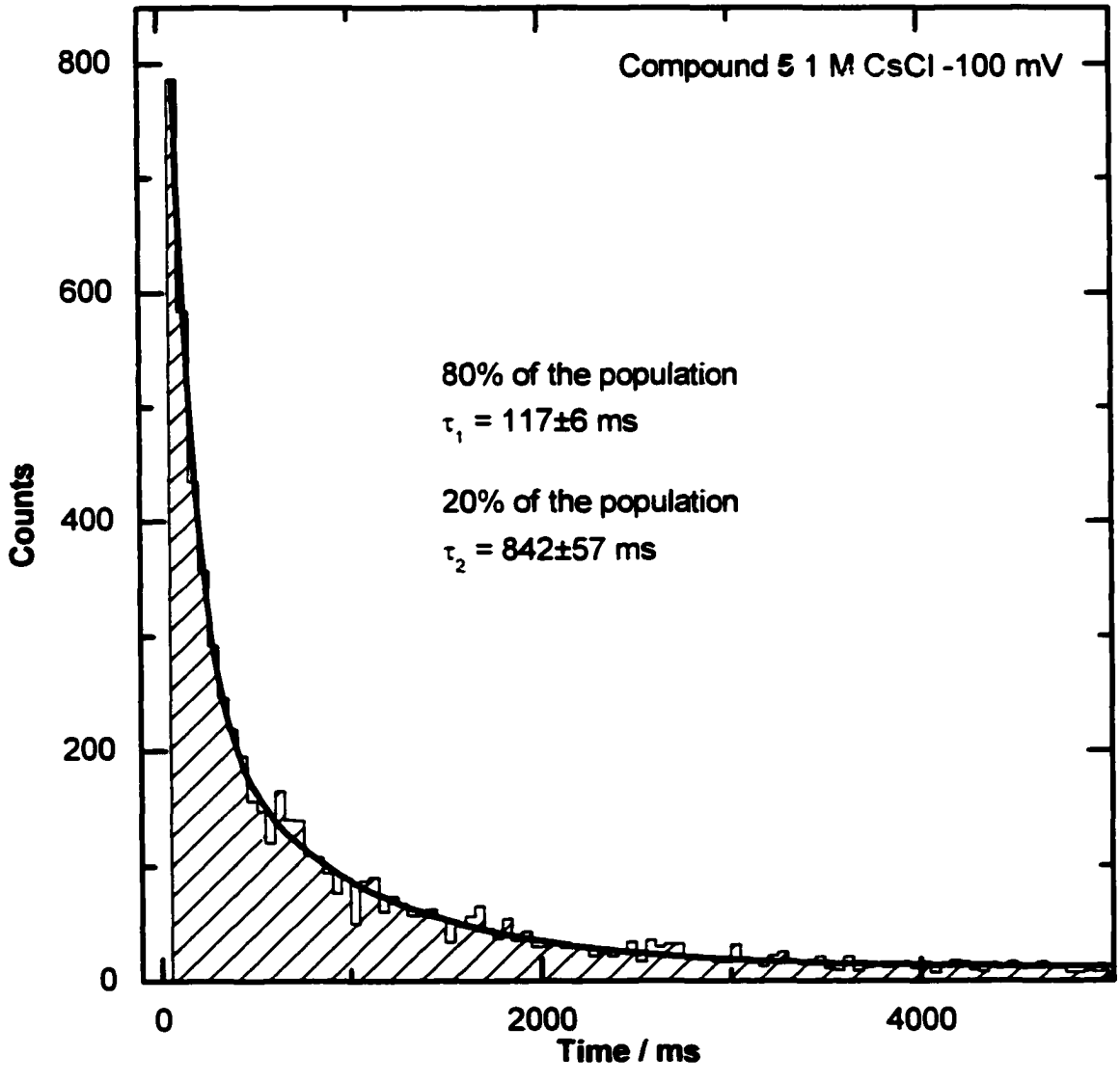

Figure 5-19. Probability density function of dwell times for compound 5.

openings was not available. Figure 5-19 is the result of channel lifetime analysis for compound **5**. The duration of channel opening, termed dwell time, will always decay exponentially. Interestingly the decay curve fits to a minimum of a bi-exponential, which indicates the channel exists in two states with different stabilities. The most common open channel state occurs 80% of the time with a τ of 117 ms whereas the remaining 20% of the population has a much longer τ of 842 ms.

The open channel lifetime of Compound **6** is shown in Figure 5-20. The obvious difference between the lifetime plots is that **6** fits to a mono-exponential and has a shorter

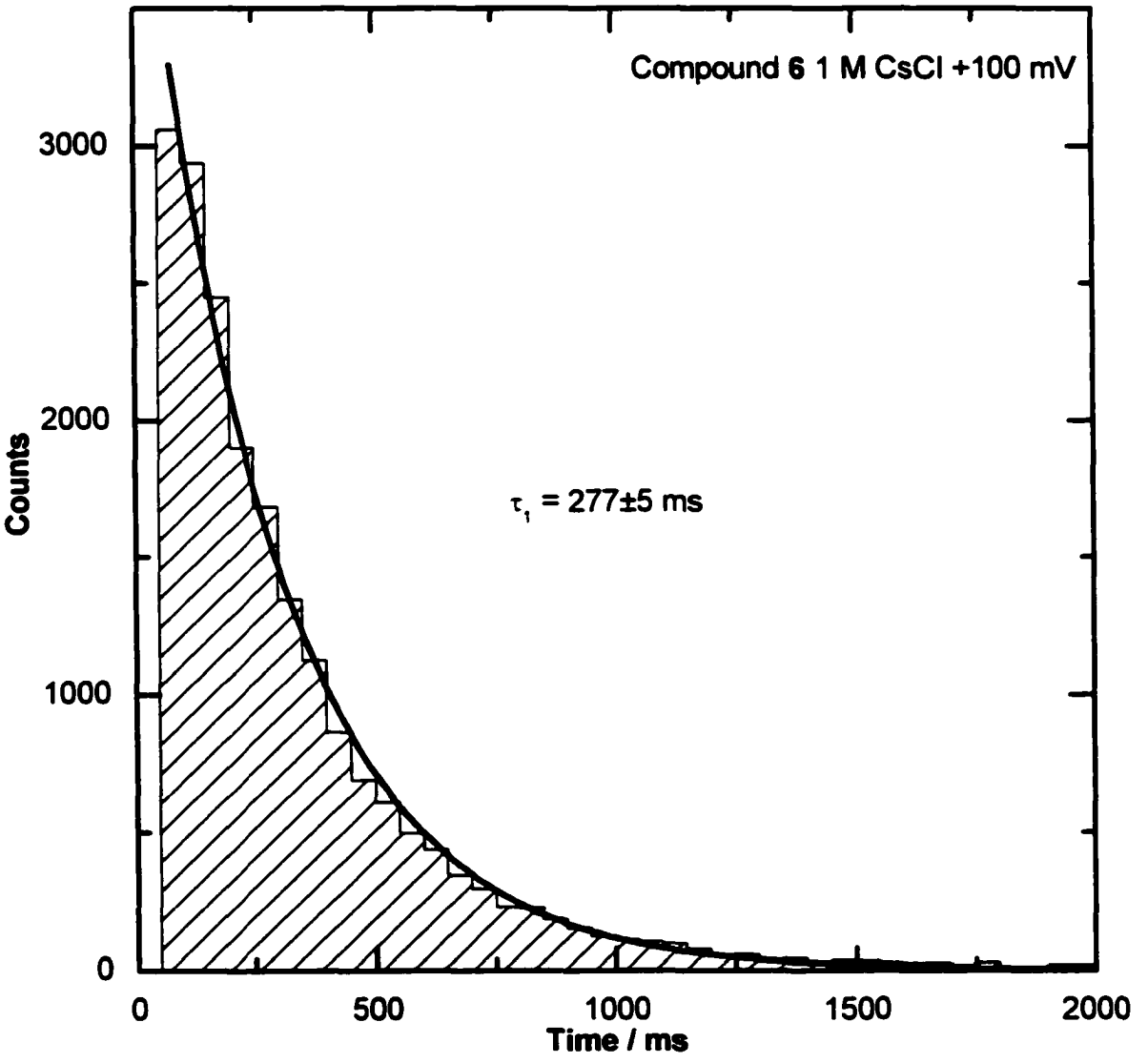

Figure 5-20. Probability density function of dwell times for compound 6.

lifetime than its structural cousin **5**. The implication is that channel **5** has an ion-conducting structure more kinetically stable than **6**. These results are in direct contradiction to the original property-directed design in this synthesis. Based on previous findings from Fyles research, similar bola-amphiphilic structures have been synthesized and were found to form ion-conducting channels in dimers[24]. Assuming a similar mechanism would lend itself to **5** and **6**, the amide bonds of the central linking unit were added to form hydrogen bonds which were hypothesized to stabilize the aggregate and yield longer-lived channels. As it turns out, the amide bonds in the center of a lipid bilayer actually have a detrimental effect on channel lifetime. Regardless of the amide- versus ester-bond stabilization arguments, the kinetic data provides a tool to clearly discriminate between compounds **5** and **6**.

5.6 How long does each conductance state stay open?

Compilation of the lifetime data and conductance histogram data together in the same plot would answer the question of which of the sub-level openings produces the longest lived-channels. A general scheme to help identify the necessary trends in the contour plots is shown below in Figure 5-21. The axes of the contour plot scheme are the absolute value of the current on the X-axis and dwell time on the Y-axis. The scheme illustrates three scenarios. The first scenario describes a situation where the lower conductance levels of the first-level opening are the most stable and thus the longest-lived. The resulting contour plot shows a large population residing at the lower sub-conductance level. The second scenario is the typical Gaussian distribution in both current and direction and shows no selection for conductance levels. The third scenario describes the opposite of the first scenario in which the lowest conducting state of a given level is also the shortest duration. Qualitatively, it was apparent by examining the raw current data that the sub-level openings, labeled **a** and **b** in Figure 5-16, were open for shorter durations than the **c** level openings. This important characteristic of the channels is lost when cumulative statistics are calculated since all data is binned and loses its paired value of either current or duration. Thus, the qualitative expectation is that the third scenario applies. To create a contour plot a large file with multiple openings and

little baseline drift was needed. The analysis yielded a 2D-binned matrix with lifetime along one axis and conductance level in the other. For compound **5** the results are shown in Figure 5-22 and clearly indicate the lower conducting sub-level openings are shorter lived than the largest conducting channel of that level. Examining the first conductance level of Figure 5-22 (-1 pA to –4 pA of X-axis), the plot shows the openings of levels higher than –2.5 pAs have maximum durations of 1000 ms. Whereas, levels centered on

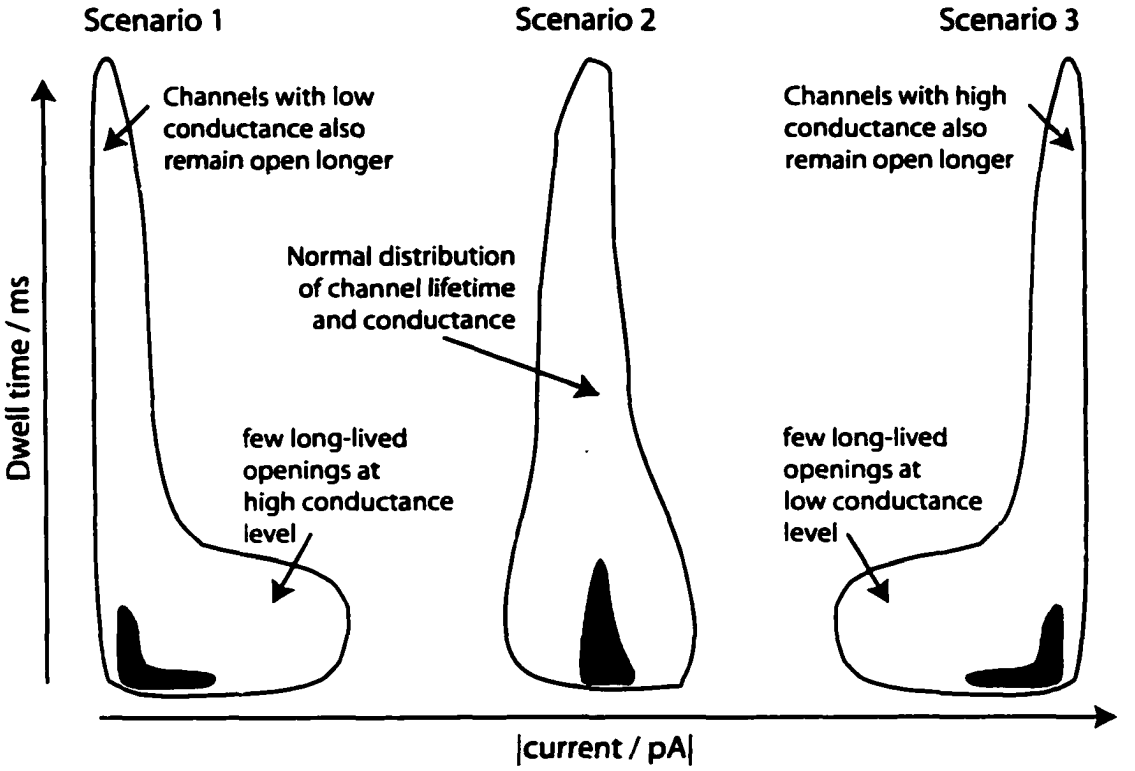

Figure 5-21. Examples of possible relationships between the duration of sub levels and their conductance.

the largest magnitude opening (-3.5 pA to – 4 pA) for level one, have some durations as long as 4 seconds. This trend, described by scenario 3 of Figure 5-22, is repeated in each of the three levels analysed, as revealed by the contour plot.

The compilation of lifetime and conductance data into its contour plot for compound **6** is shown in Figure 5-23. As Figure 5-23 illustrates, the plot has three conductance levels centered at 3.5 pA, 6.5 pA and 9.5 pA. The general shape of the plot in the 0 pA to 6 pA region (corresponding to the first opening levels) shares the same characteristics of the plot shown in Figure 5-22. The plot shown for compound **6** was

done under positive potential therefore the general shape of the plot can be directly compared to scenario 3 of Figure 5-21.

In summary, compounds **5** and **6** are ion-channels because they exhibit step conductance and have currents not obtainable by an ion-carrier mechanism. They each show some level of ion selectivity following Eisenman I sequence. At the single molecule level, they are indistinguishable. Cumulative statistics of current illustrate typical channel behaviour at large bin sizes. At smaller bin sizes, discrete sub-population

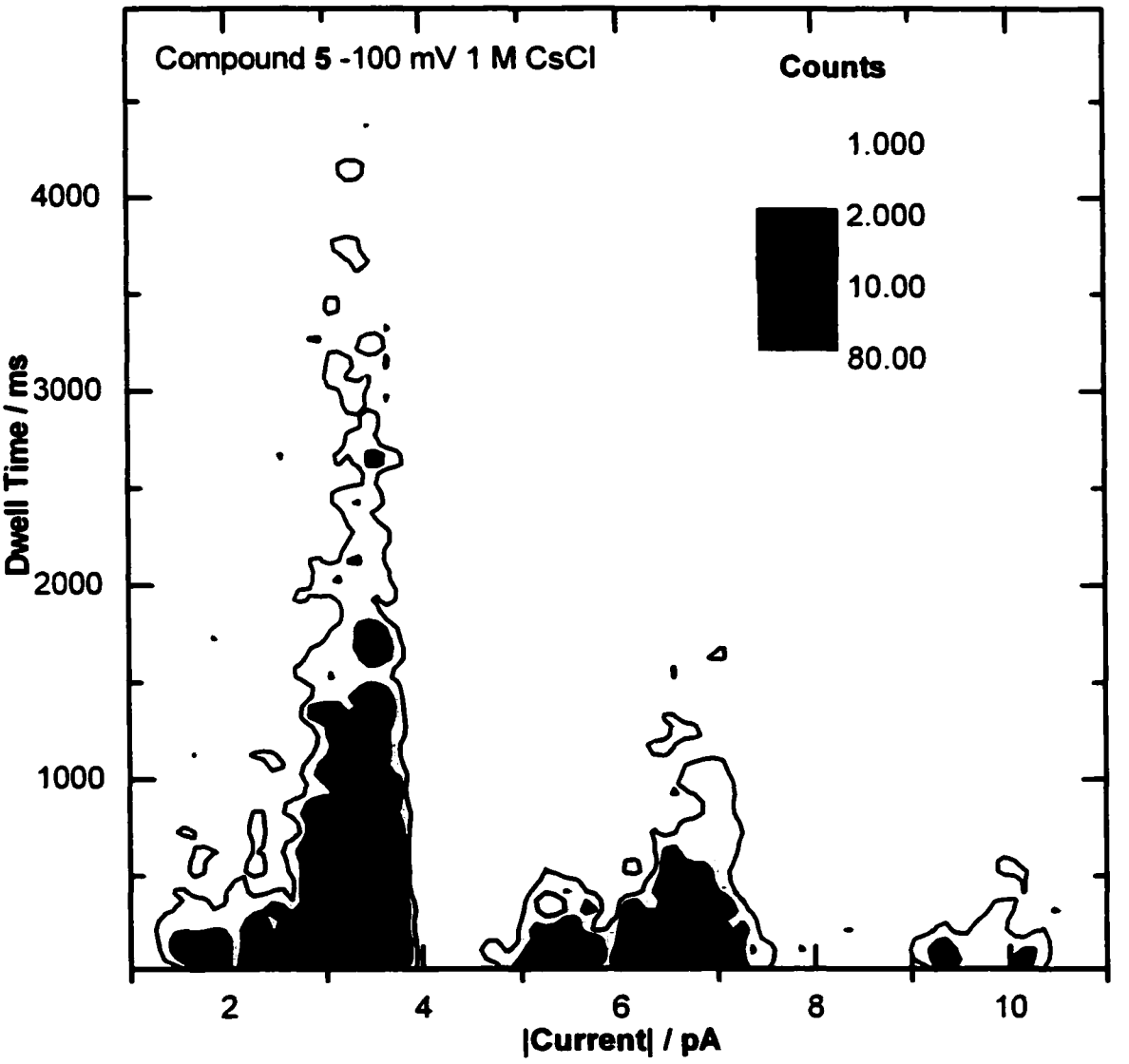

Figure 5-22. Contour plot of dwell time versus absolute current for compound 5.

levels emerge. Again, cumulative statistics cannot differentiate these two compounds since both show similar sub-level populations. Lifetimes of channel duration provide the

handle to discriminate between **5** and **6** because **5** has two lifetimes of 117 ms and 842 ms compared to **6** which has one lifetime of 277 ms. Further investigations also revealed that the sub-level openings have a reproducible relationship with lifetime. The findings show that the smaller conducting states within one level are also the shorter lived opening events or, alternatively, the longer lived channels are also the most conducting channels.

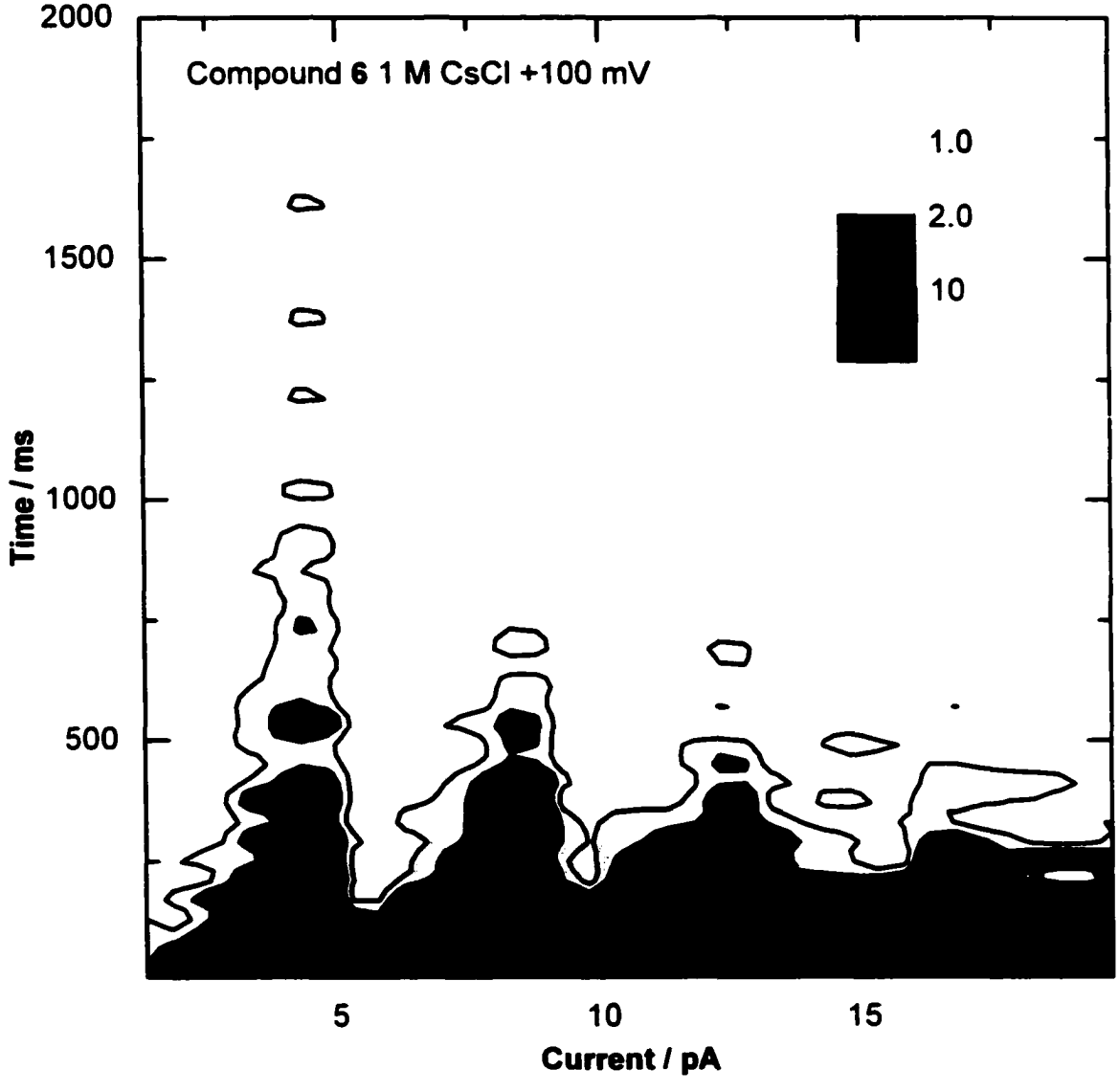

Figure 5-23. Contour plot of dwell time versus absolute current for compound 6.

Despite the amount of information acquired concerning the ion-channel activity of compounds **5** and **6**, an underlying mechanism is elusive. The histogram plots of step conductance suggest that the pore forming structure is not an aggregate like alamethicin but more like gramicidin where each channel is a copy of itself. This is not saying that

the channel is unimolecular. In fact, it is difficult to draw a mechanism that would allow ion transport using only one molecule of either **5** or **6**. For this reason, it is proposed that the active structure is an aggregate (2 or more monomers) but it does not function in a barrel-stave manner. In addition, the emergence of sub-population peaks within one conductance level may be an indication that there are too many degrees of freedom in four-armed structures. Perhaps, a linear derivative with only two arms may have smaller sub-level populations. The lifetime data is puzzling because the amide bonds are presumably able to hydrogen bond and stabilize the aggregate structure; yet the ester shows a much longer-lived, thus more stable, ion-channel. It is speculated that amide bonds do add stability to a channel forming structure compared to the ester derivative as evidence by the shorted lived component of the ester (117 ms) compared with the amide (277 ms). The long-lived component achieved by the ester is a different ion-channel structure than the short-lived structure and the more stable structure of the ester is unattainable by the amide derivative. More baffling, is the result that both channels are unaffected by pH changes. A preliminary look at three pH values (4.0, 7.4 and 10.4) was done and no effect on channel activity was observed on either system suggesting that amine protonation may not play a role in channel orientation.

There are significant challenges for this type of system and it might be better to shift to another of the synthetic systems now available to study the required level of detail.

5.7 Ion-channel Experiment

5.7.1 Chemicals

Diphytanoyl phophatidylcholine (diPhyPC) in chloroform was purchased from Avanti Polar Lipids. They were shipped on dry ice and upon arrival were divided into sealed glass vials under an argon atmosphere and stored at −12 °C. Decane (99%) and ethanol were purchased from Aldrich. Gramicidin D was purchased from Sigma/Aldrich. Potassium nitrate and chloride salts of alkaline halides were purchased from Aldrich (99.8%) and used without further purification. Agar powder was purchased from Northwest Laboratories and use without purification. Only Nano-pure™ water was used with a resistivity of greater than 17.9 Ω·cm.

5.7.2 Instrumentation

A model BC-525A bilayer clamp (Warner Instrument Corporation) was used for planar bilayer experiments. The analog output was filtered with an 8-pole Bessel filter (Frequency Devices, model 902) and digitized with a 333 kHz digitizer (Axon Instruments, Digidata 1200). Data acquisition and analysis was controlled by pClamp8 software package (Axon Instruments). In addition to the analog filter, some instances called for a digital low-pass filter. The headstage and the bilayer chamber were placed on a floating table (Technical Manufacturing Corporation) and electrically shielded by a grounded Faraday cage of aluminum.

Chapter 6 Single-molecule release to bilayer system

The purpose of this chapter is to bring together the release of adsorbed molecules from an Au surface and the ion-channel analysis. The ultimate goal is to covalently link a thiol derivatized ion-channel to an Au-microelectrode, place it next to a bilayer, and release the channel accomplishing spatial control of channel insertion. The conventional methodology of channel insertion relies on a small volume injection near the bilayer. This has a couple of inherent problems. First, the injection method is mechanically abrasive and often times results in bilayer rupture. Reformation of the bilayer is normally not a problem but when rectification is the goal, a process that could allow channel orientation to be scrambled is inherently flawed. The incorporation of a voltage-gated ion-channel will most likely involve a channel that possesses a permanent dipole established by charge separation. The creation of an unsymmetrical bilayer by compound addition to only one of two compartments allows for a unidirectional insertion of an asymmetric ion-channel. Nevertheless, this unsymmetrical bilayer is dependent on keeping the bilayer intact during the insertion process. The rate of bringing a charged group through the low dielectric medium of the bilayer is extremely slow, on the order of 300 min^{-1} to $days^{-1}$ for charged phospholipids[196]. Thus a compound with one highly charged headgroup and one neutral headgroup should insert only one way. This type of situation sets up favorable conditions for current rectification, or voltage-gated channels.

A second problem inherent to syringe injection is the poor efficiency of the incorporation. A typical experiment will inject between 10^{10} and 10^{12} molecules of a synthetic ion-channel into one of the compartments and monitor the actual insertion of only 1-10 of those molecules. The use of a microelectrode attached to a micromanipulator allowed for the required precision to electrochemically insert the channels. Even though the released ion-channel inserts into the bilayer under the same diffusion-controlled partitioning as the syringe method, the local concentration of ion-channels can be much higher proximal to the bilayer under Au electrode control. Recall that the release experiments in water produced insoluble layers indicating a very high local concentration. In addition, the number of channels placed on the tip of an Au electrode is potentially much smaller than any injection method, so efficiency is

increased. This idea of efficiency is critical to the synthetic chemist because, until recently, ion-channel synthesis has been an arduous process resulting in small amounts of final compound and very poor overall yields.

The following two sections explain the experiments attempted, leading towards a device to accomplish the release of ion-channels into lipid bilayers. The first method involves non-covalent, non-specific interactions to accomplish channel insertion and has been termed the mechanical transfer method. The second method is loosely described above and is appropriately termed the electrochemical transfer method.

6.1 Mechanical transfer

This is a method developed to transfer compound to bilayers and can apply to most membrane inserting compounds. The principle behind the transfer is an Au-electrode that can be modified with a covalently linked hydrophobic surface, such as octanethiol. When the octanethiol SAM is placed in the channel containing solution the compound will adhere to the octanethiol by hydrophobic interactions. The incorporation of channels is non-specific since there are numerous geometries and conformations that allow hydrophobic overlap between the channel and the monolayer as depicted in Figure 6-1. This method would provide access to many channel compounds that do not possess thiol functionalities.

Gramicidin was chosen as the first candidate to be adsorbed onto the hydrophobic Au surface and inserted into the bilayer. The experiment was done by preparing a 10 μm diameter Au electrode with a monolayer of octanethiol using methods described in Chapter 3. The monolayer-covered electrode was then dipped into a micromolar solution of gramicidin for 10 seconds and washed with water. The resulting electrode was proposed to have incorporated several gramicidin molecules via hydrophobic interactions as depicted in Figure 6-1. The physisorbed gramicidin was then brought next to the lipid bilayer system with the aid of a microscope and a micromanipulator where it was poised for insertion for a period of half an hour during which the bilayer was clamped at 100 mV and the current was recorded. This was done to test the feasibility of octanethiol as a hydrophobic surface. If the recordings detected channel openings due to gramicidin then

the hydrophobic layer would be deemed insufficient to support gramicidin. However, no channel current was observed for the entire period as indicated by the current trace in Figure 6-1. The bilayer electrodes were turned off and the Au electrode was slowly passed through the aperture in the cuvette and returned to its original position. The

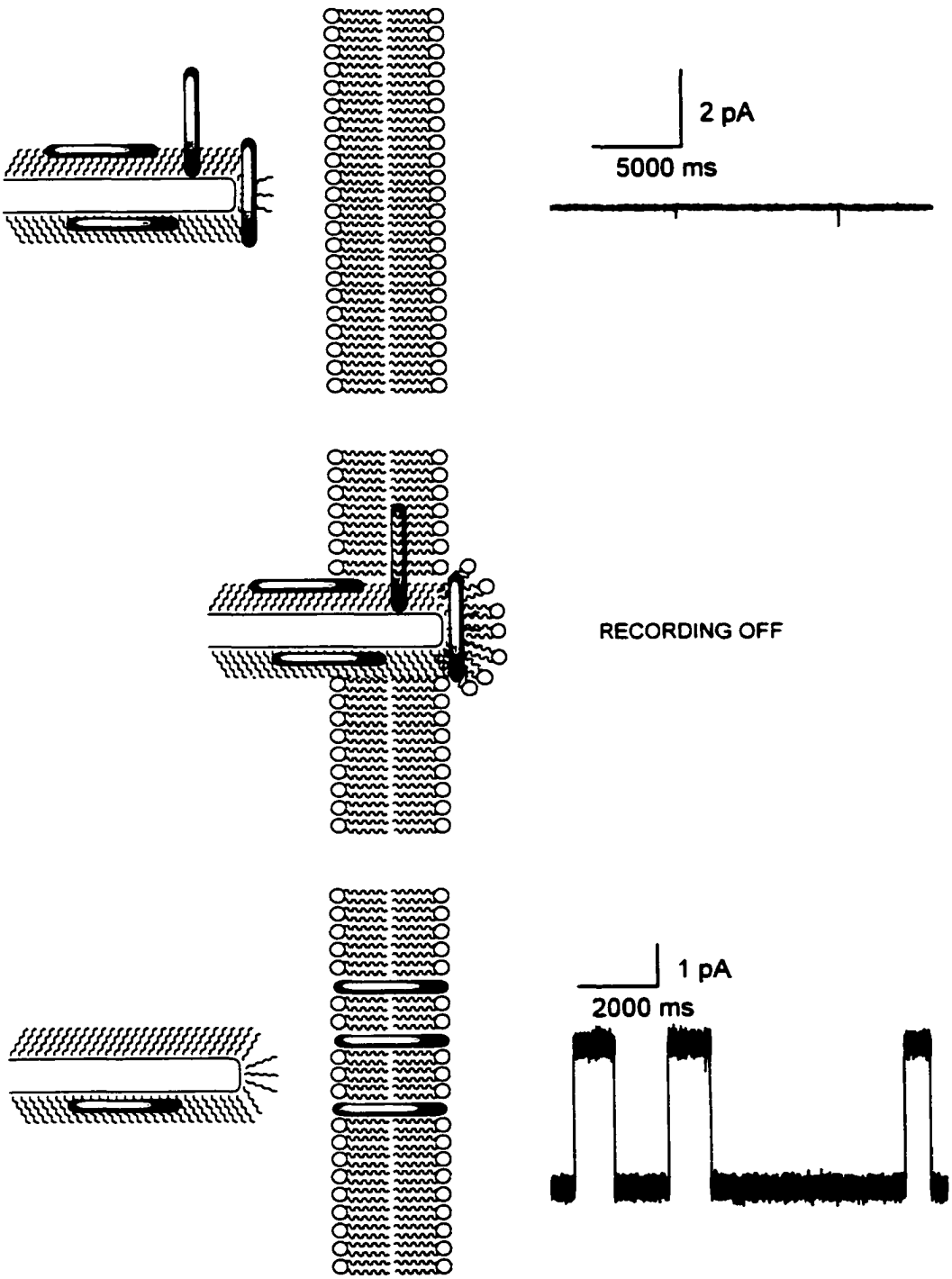

Figure 6-1. Time course of the electrode placement with respect to the bilayer and its associated current trace.

partioning of gramicidin to the bilayer over that of the octanethiol monolayer was expected to occur. The mechanical placement of the Au electrode through the lipid membrane frequently resulted in bilayer rupture. However, if the Au probe is under precise control, the lipid bilayer allows the probe to penetrate the lipid bilayer without rupture. Unfortunately, precise control of the Au electrode requires a more sophisticated X-Y-Z-manipulator than was available so many more bilayers were ruptured than necessary using this method. As shown by Figure 6-1, some gramicidin was transferred by this method.

The mechanical transfer method has the advantage of using a very small number of molecules thus addressing the issue of efficiency of channel incorporation. In the experiment done the actual number of molecules is completely unknown except that that total quantity is certainly less than would be required by conventional techniques. However, the method is still too abrasive, as several of the bilayers were broken during the transfer process and as stated previously, a broken bilayer after insertion can lead to a loss of asymmetry. In addition, this use of hydrophobic interactions to non-specifically adsorb ion-channels cannot be used as a quantitative transfer device since surface topology and ion-channel structure will play key roles in determining how many ion-channels will adsorb.

6.2 Electrochemical transfer

A more elegant approach would be to electrochemically release an ion-channel next to a bilayer system. This would be a "gentle" method of channel incorporation and because of that would preserve the rectification inherent in the design of the molecule since no bilayer would be broken. The only chemical limitation of this method is that it requires a thiol covalently linked to an ion-channel. Not many active channel compounds, either synthetic or peptide based, are known to contain thiols. This has the potential for a fundamental flaw so work was done to try and find a derivatization method that allows incorporation of a covalently linked thiol to channels that will be bound but, when released, the thiol would not be part of the system, liberating the free channel in its active form. To this end, the chemistry of a linker molecule has been developed in

collaboration with undergraduate coworkers Mischki (2000), Buchmann (2001) and Yip (2001). The linker chosen is thiobutyric acid that can undergo common esterification with most alcohols and then be linked to the Au surface by normal means. Many channel compounds contain a free hydroxyl group that can be used to make esters thus opening larger possibilities of channel exploration than was previously possible.

A systematic study to determine the feasibility of using a butyrate ester as a linker group was undertaken. Literature precedence[197] revealed that the thiobutanoic acid underwent intramolecular thiolocatone formation at a greater rate than its six-membered cousin, thiopentanoic acid. To ascertain the use of thiobutanoic acid as an effective linker to Au surfaces the following compounds (Figure 6-2) were synthesized principally

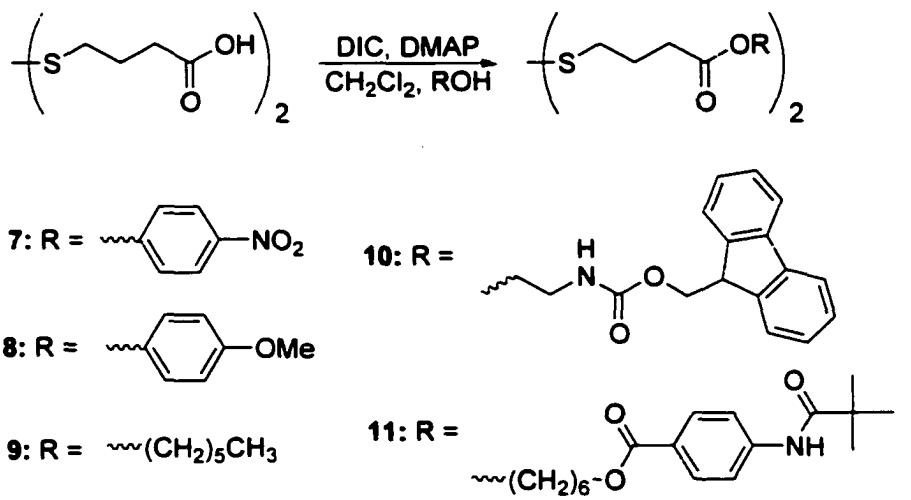

Figure 6-2. Synthesis of dithiobisbutryate esters.

by Buchmann. Reduction of the disulfide bond in compounds **7-11** was done both chemically and electrochemically. The chemical reduction was performed with dithiotheritol (DTT), a commonly used reducing agent. Chemical reduction was necessary because the reaction was monitored by UV-Visible spectrometry and products were confirmed by ^{1}H-NMR. Both of these techniques fall outside the concentration range attainable by Au surface reduction. The chemical reduction of the disulfides was found to only operate at basic pH. This constraint required a further study because it is possible that the release of alcohols could be due to base hydrolysis rather than the desired thiolactone formation. Figure 6-3 shown below outlines the competitive pathways that could lead to phenolate (**7** and **8**) release. The experiment was run under

basic conditions (pH 10.4) and therefore specific base hydrolysis of the ester had to be considered as a viable alternative for phenolate release. The evolution of phenolate, as followed by a UV-Visible spectrometry, under basic conditions without addition of DTT showed a phenolate release half-life of 3000 s. Under the same conditions with the addition of DTT, the formation of phenolate had a half-life of 22 s. The specific base hydrolysis rate (k_{OH}) is assumed constant in the presence and absence of DTT. The

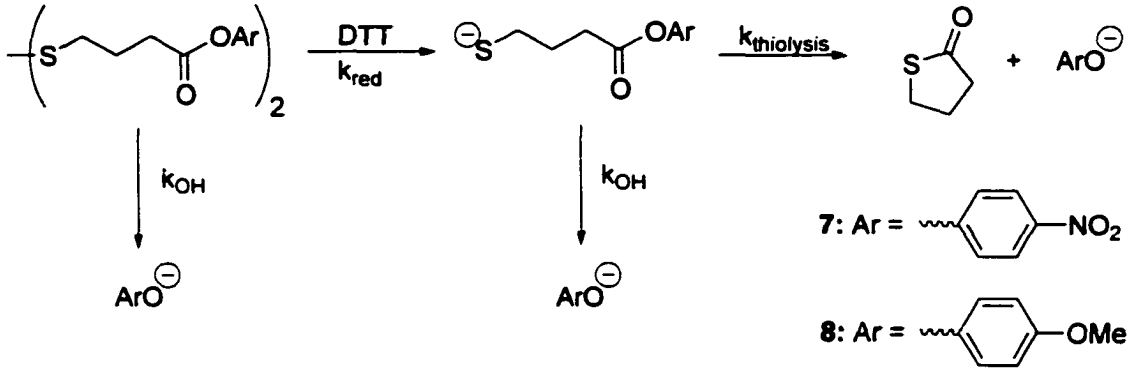

Figure 6-3. Competitive pathways for phenolate release in basic solution.

100-fold increase in rate is attributed to the intramolecular thiolysis reaction to produce the phenolate ion. The experiments clearly show that on a kinetic scale, intramolecular thiolysis of thiobutyric acid is feasible as a candidate linker to Au surfaces.

^{1}H-NMR experiments were done on compounds **7**, **8**, **9**, **10** and **11**. The goal in this set of experiments was to identify all products and ratios of products that are formed under chemical reduction and basic pH. The results agreed with the UV/Visible spectrometry results in that phenolate or alcohol was the only release product and the formation of thiolactone was detected. The significance of the product identification is that primary alcohols could also be released, even though at slower rates.

Compound **10**, a primary alcohol upon release, is an Fmoc-derivative of ethanolamine. This compound has a couple of features that made it appealing for the electrochemical release experiment. First, it is fluorescent, which lowers the detection limit for direct determination. Second, if Au is to be used as a solid support for organic synthesis, Fmoc derivatives are standard protocol in polyamide synthesis. Third, ethanolamine is the final residue on the C-terminus of gramicidin. This corresponds to a simplified gramicidin mimic. The electrochemical release of **10** from an Au-surface was

done on Au-powder instead of planar Au electrodes in hopes of attaining a ^{1}H-NMR spectrum of the released material. Unfortunately, the quantities were much too low for ^{1}H-NMR and fluorescence was needed. Regardless, after electrochemical reduction for 30 s at –2.0 V, the release of Fmoc-ethanolamine was confirmed by HPLC. The overall use of thiobutyric acid as a "traceless" linker molecule to liberate alcohols has been shown to be successful and can be extended to releasing channel-forming compounds. The details of this traceless linker have been published by our group[198].

Buchmann and Yip have developed the esterification process outlined in Figure 6-4. One equivalent of gramicidin is coupled with one equivalent of **12** to give a mixture of unreacted gramicidin and the monoester, **13**. The compounds are purified by an LH-20 gel permeation column. Chemical reduction of **13** with DTT liberates gramicidin as seen by HPLC analysis and MALDI TOF MS[199].

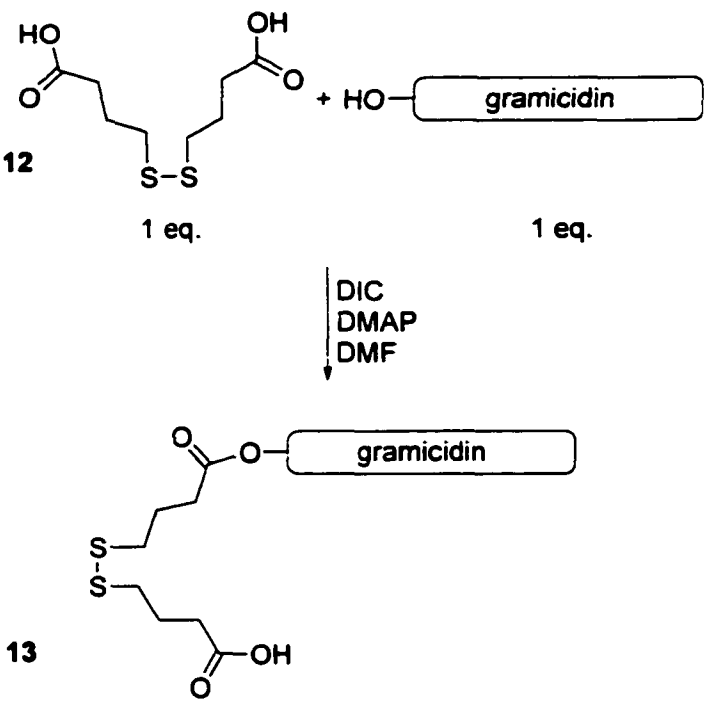

Figure 6-4. The linkage of dithiobutryic diacid to free hydroxyl group of gramicidin.

The proposed mechanism for the release of gramicidin via intramolecular thiolysis is shown in Figure 6-5. The Au-S bond is cleaved to produce the thiolate, the thiolate undergoes thiolysis forming the five membered thiolactone ring. The ring formation reaction yields the gramicidin oxide, which is immediately, or concertedly, protonated to release the alcohol.

Efforts in the electrochemical reduction proximal to a lipid bilayer with a derivatized gramicidin have been promising to date. The main limitation is in the positioning of the microelectrode close to the lipid bilayer without rupturing it: The available micromanipulator is insufficiently discriminating and positioning is extremely difficult.

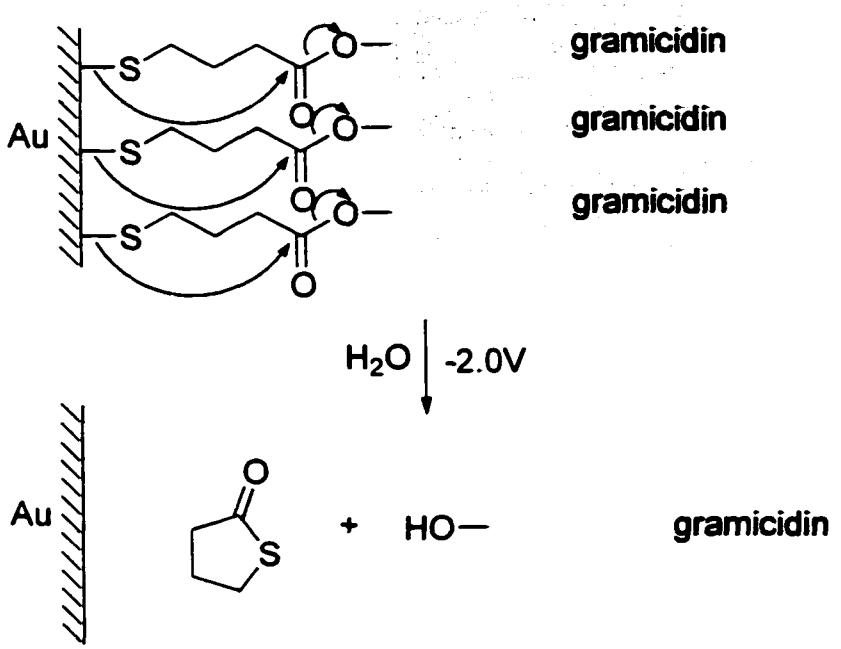

Figure 6-5. Mechanism for intramolecular thiolysis of thiobutryric acid to release ion-channels at reductive potentials.

Figure 6-6 shows the current traces of a bilayer in two situations. The first is the lipid bilayer with an Au electrode containing immobilized **13**, positioned within 10μm of the aperture. The second is the same bilayer after electrochemical reduction has taken place. Both of the traces shown have the same vertical and horizontal scale. The gramicidin ester **13** has the same single channel properties as gramicidin so would be indistinguishable in this experiment. The first trace of Figure 6-6 shows some channel activity, which is attributed to insufficient rinsing of the Au electrode after deposition. It is clear that some gramicidin was mechanically transferred to the bilayer. After electrochemical release, the trace shows more frequent channel activity. The integrated current of all events before electrochemical release is 0.19 μC compared to the total charge passed after gramicidin release of 1.5 μC. After release, an eight-fold increase in activity is observed. In the pre-release trace, there is a minimum of six gramicidin molecules producing the trace. By extrapolation of the total charge consumed, there would be a minimum of 50-gramicidin molecules producing the bottom trace. In summary, a method using non-specific adsorption of gramicidin to an octanthiol-modified electrode can be used to mechanically transfer small amounts of compound to a lipid bilayer. The lack of thiol containing ion-channels led to the successful development

of a traceless linker capable of derivatizing most alcohols. The feasibility of the linker molecule has been confirmed by the release of Fmoc ethanolamine and gramicidin. The electrochemical release of gramicidin, although not conclusive, has shown that electrochemical release results in an increase in overall channel activity. It is unclear at this time whether the increased activity observed is due to native gramicidin or **13**.

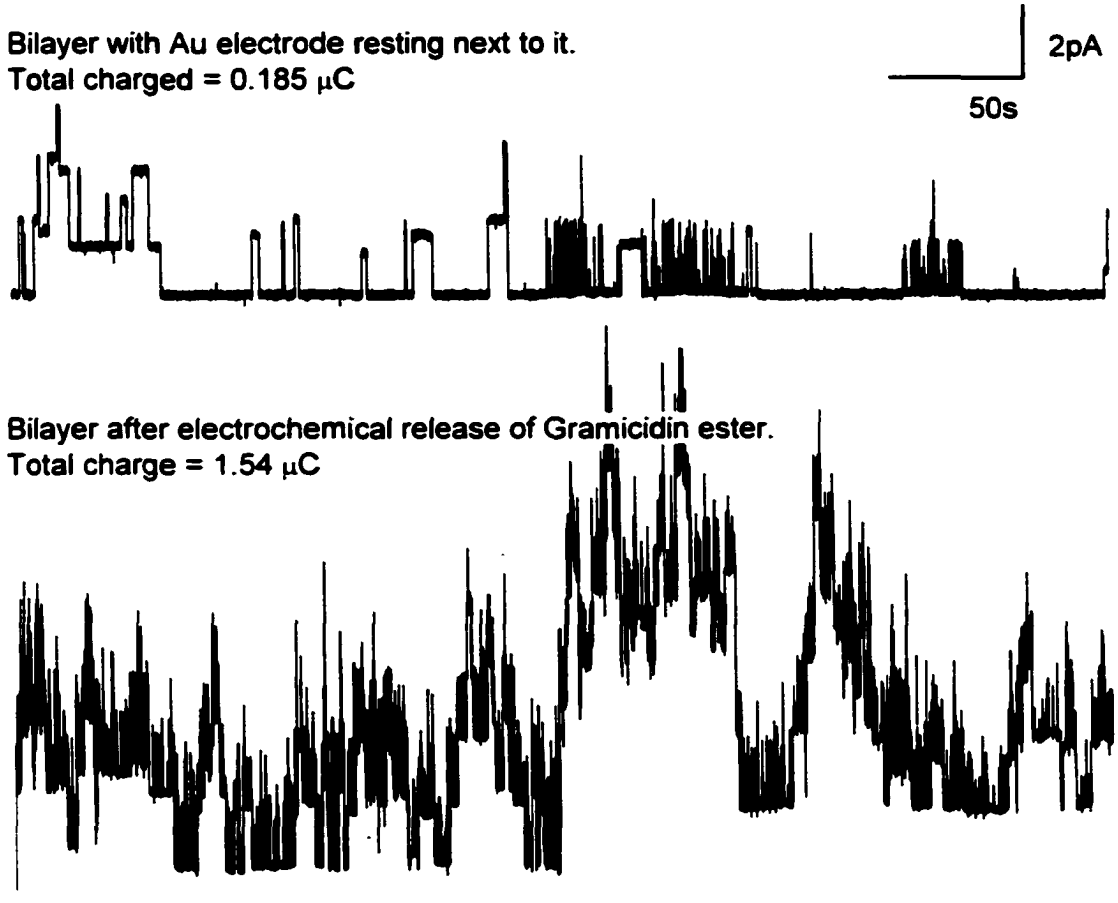

Figure 6-6. Current trace of the lipid bilayer clamped at +100 mV before and after electrochemical release of gramicidin ester (diPhyPC 1 M KCl).

6.3 Experimental

6.3.1 Procedure

The procedure for the mechanical transfer method was as follows. The Au microelectrode was cleaned according to procedures outlined in Chapter 3. The octanethiol solution was deposited using the open circuit incubation method from a pure octanethiol solution. The rinsing procedure of Chapter 3 was used. The tip of monolayer-protected Au electrode was dipped into a 6.3 μM methanolic solution of gramicidin for 10 seconds followed by rinsing with Nano-pure™ water. The electrode was attached to the micromanipulator by HoldIt® putty and positioned with an X-Y-Z manipulator on a grounded microscope stage (Northwest Supplies). The bilayer clamp setup was the same as described in Chapter 5 on the stage of the microscope. The electrolyte used was a 1.0 M NaCl pH4 citrate buffer. The Au electrode was placed next to the lipid bilayer in the trans compartment and held for 30 minutes while the bilayer was clamped at +100 mV. During the positioning of the electrode, the BC-525A was placed in the "standby" mode because the microscope light source produced too much noise. Once positioning of the electrode was completed, the power source of the microscope was unplugged and the cord placed inside the Faraday cage. After 30 minutes of recording, the BC-525A was switched to "standby" mode while the Au electrode was directed by the micromanipulator to slowly penetrat the aperture and return to its original position. Immediately the BC-525A was switched "on" and recording under +100mV clamp continued.

The procedure for the electrochemical transfer was as follows. The Au microelectrode was cleaned as described in Chapter 3. The thiobutyric ester of gramicidin was deposited under controlled-potential conditions as described in Chapter 3 from a 1 mM solution in DMF containing 0.5 M Bu_4NPF_6. The same rinsing procedure was followed as described in Chapter 3. The two experiments- releasing ion-channel and bilayer clamp- were done independently of one another. "Independently" means that as one experiment is underway the other is in the "off" state with all power sources disconnected and all electrical connections placed within the Faraday cage to limit

antennae effects. The Au microelectrode was fastened to the manipulator arm and connected to the home-built potentiostat via a BNC cable. The positioning of the electrode required the BC-525A to be "off" because of the light source noise. Once a bilayer was established the microelectrode was positioned close (10 μm) to the aperture in the trans compartment. A 0.17 cm^2 counter Au wire electrode was placed next to it. An Ag/AgCl wire used in the bilayer clamp experiment doubled as a reference electrode. The bilayer clamp experiment was set up as described in Chapter 5 with 1.0 M NaCl pH4 citrate buffer as the electrolyte. Once the microelectrode was positioned, 30 minutes of bilayer under +100 mV clamp conditions were recorded. The reductive cleavage occurred as described in Chapter 4 with the BC-525A in the "standby" mode. Immediately following the cleavage recording under +100mV clamp conditions continued.

The following pictures are included to give a better understanding of the positional arrangement of the apparatus.

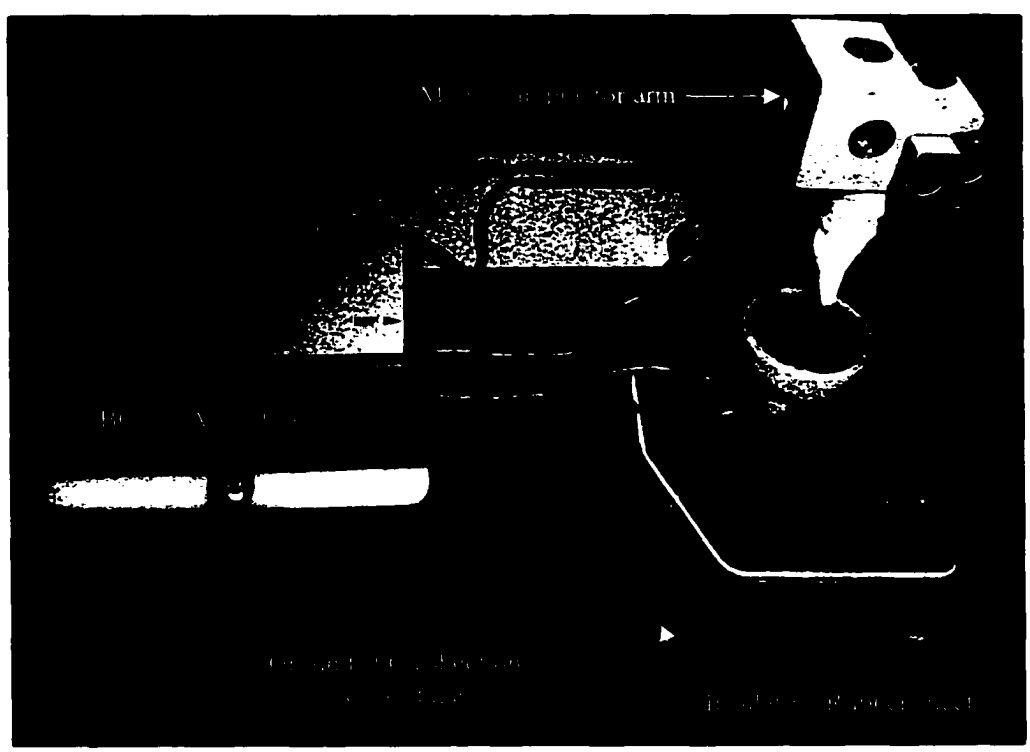

Figure 6-7. The stage of the microscope with the bilayer clamp cell setup.

Figure 6-8. Bilayer clamp cell: front view.

Chapter 7 Summary and Prospects

The long-term goal of this project is directed towards signal propagation in an artificial system. However, successfully meeting the functional and physical requirements of such a system may be several years away. The synthesis of ion-channels is at stage where many structural variations resulting in the desired properties are near. As a result, this thesis has described how the physical requirements could be met once the correct synthetic channels arrive. The core idea behind the thesis is the controlled release of thiols from an Au surface by electrochemical reduction.

In the first section of the thesis was the synthesis of the dye molecule that satisfied both electrochemical and analytical demands. The electrochemical demands were easily met by using a long alkyl chain to space the immobilized thiol from the terminal dye chromophore and the fluorescent demands were met by choosing a biphenyl ether. Au-thiolate monolayers were created by two means: one used the standard open-circuit incubation method and the other used the potential-assisted deposition method. Both methods formed monolayers with adequate surface coverage as monitored by cyclic voltammetry and double-layer capacitance techniques. Analysis of the fluorescent-labeled thiol was developed with detection limits in the range of 10^{-9} M. Analysis of mixtures produced by reductive cleavage gave different results depending on the reduction solvent. In MeCN and water the thiol was the sole detectable product in unpredictable amounts whereas in DMF the reductive release produced only the disulfide. The explanation for these strange results probably stems from the poor solubility of the thiol compounds and several alternatives were discussed in the summary to Chapter 4.

At this intermediate point the thesis turned to a detailed evaluation of the channel activity of two four-armed compounds. Both compounds formed channels but the channels had the same ion selectivity and conductance and neither was voltage-gated. Cumulative statistics describing a population of ion-channels was needed to differentiate between the two compounds. Unique sub-level opening events were seen for the family of channels tested. Delving deeper into the analysis led to the findings that the smaller conducting sub-level openings also had shorter ion-channel lifetimes. Analysis of the

structure-function relationship was difficult because aggregation numbers are presently unknown. However, the statistical results clearly show that the ester moiety in the central linking unit stabilizes the conducting state more than the amide moiety in the same location. This analysis also indicates that the use of the 4-armed channels will pose significant problems in the eventual development of a signal propagation system.

The use of Au to release ion-channels was explored in Chapter 5 with varying degrees of success. The mechanical transfer of gramicidin by using non-specific hydrophobic interactions works well. However, the major disadvantage of this method is that the bilayer is often broken and thus ion-channel rectification could potentially be lost. Chemical cleavage of a thiobutyrate ester derivative of gramicidin by DTT and subsequent analysis by HPLC has shown that gramicidin is regenerated in its channel active form and no thiobutyrate ester was observed. Electrochemical reduction of an ion-channel next to a lipid bilayer resulted in a very significant increase in the number of ion channels active in the bilayer. This constitutes a proof of principle experiment that awaits a more sophisticated micromanipulator system to bring this to a truly practical method.

7.1 Outlook

The thesis describes the first step leading to a system capable of signal propagation. The success of this effort will require significant efforts on several fronts. Current synthetic work has led to the development of a rapid synthesis of non-symmetric channels. With ion-channel synthesis coming to a more synthetically achievable level, more derivatives will be available to probe the structure-function relationship at a much faster rate than has been possible in the past. The large step forward in channel synthesis has led to the necessary development of a system which, when the voltage-gated ion channels come into hand, will allow for the study of ionic signal propagation. There is also significant work to be done to elucidate mechanism. The functional pieces that are missing are two voltage-gated ion channels that are also ion selective. It is not necessary for the ion-channels to have the same ion-selectivity as the natural system but a

complementary preference for one ion over another is necessary to keep a resting membrane potential.

The physical requirements made in this thesis point to a possible experimental structure for the system to be created. Such an experiment will take the present system of one aperture and one Au microelectrode covered in ion-channels in an asymmetric electrolyte medium and build an array of apertures. The array of bilayers is shown

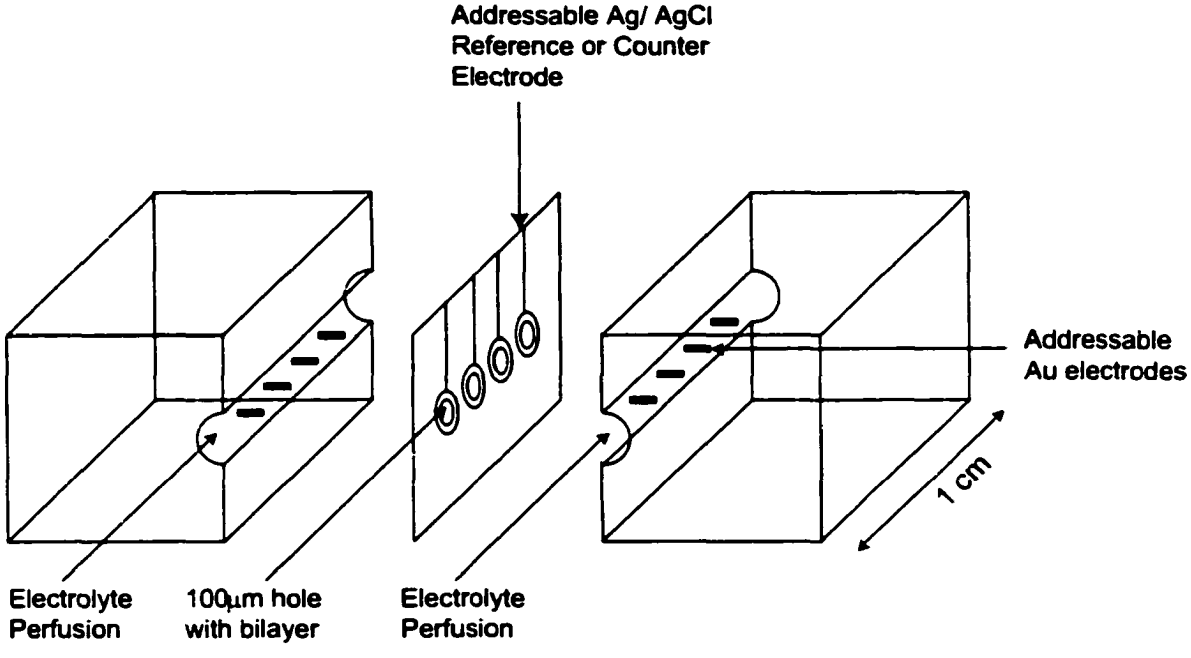

Figure 7-1. Schematic design of an array of bilayers whereby each bilayer is monitored by its own electrode and contains its own Au microelectrode allowing for release of ion channels to different sides of the bilayer.

schematically in Figure 7-1. The maintenance of a resting potential gradient is established by continual electrolyte perfusion. Each patch of bilayer has its own addressable Au microelectrode on either side poised to release ion-channels. The separation between the bilayer patches should be a similar to the distance between nodes of Ranvier. The material chosen for the aperture support must be of a very insulating material akin to the myelin sheath of the neuron axon. That way, upon depolarization by one of the electrodes, the ions can only propagate the signal in a radial fashion.

Whatever, the eventual device, this project has begun the synthetic exploration of systems of supramolecular systems.

Appendix

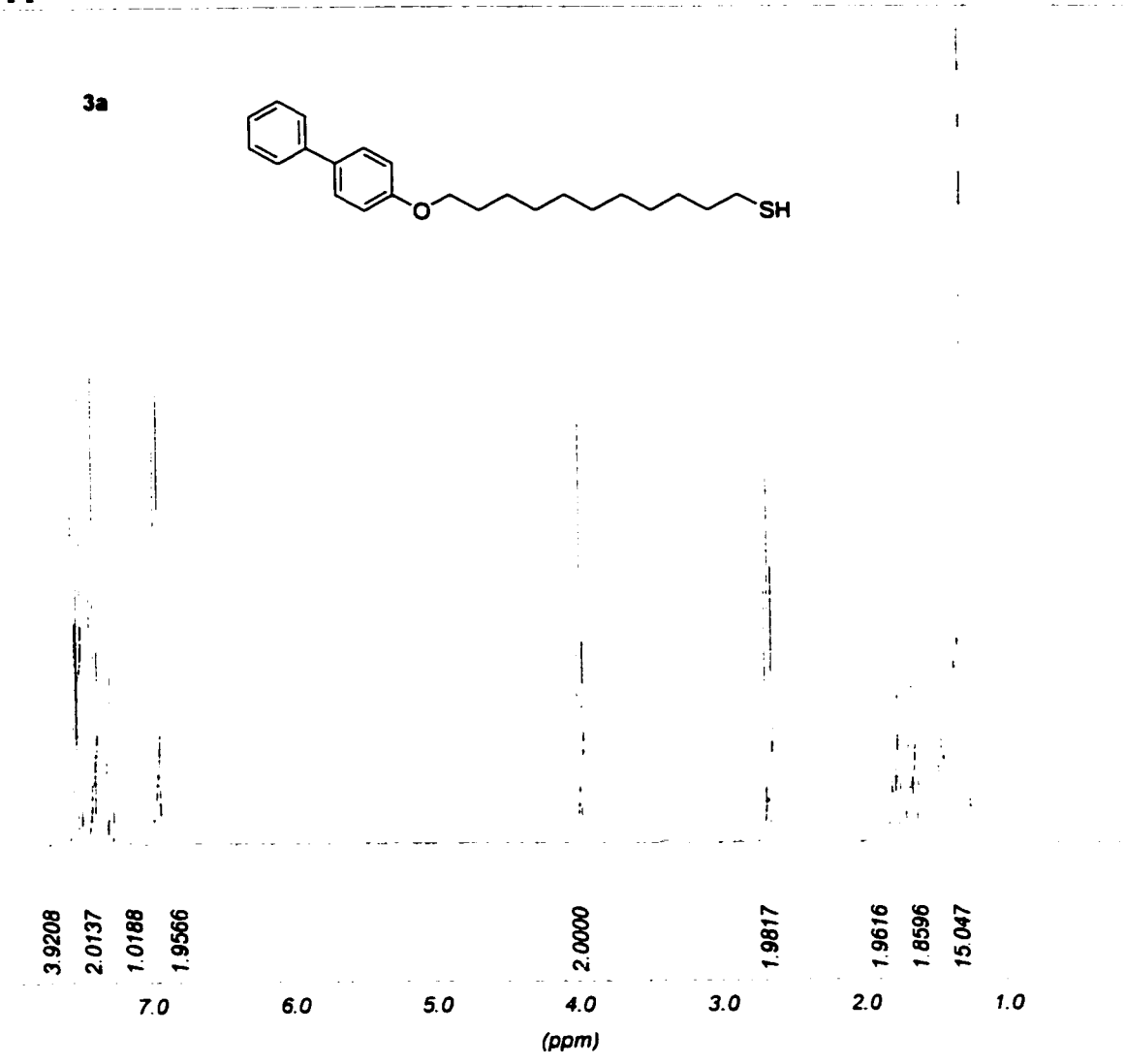
3a
O
SH
3.9208
2.0137
1.0188
1.9566
2.0000
1.9817
1.9616
1.8596
15.047
7.0
6.0
5.0
4.0
3.0
2.0
1.0
(ppm)

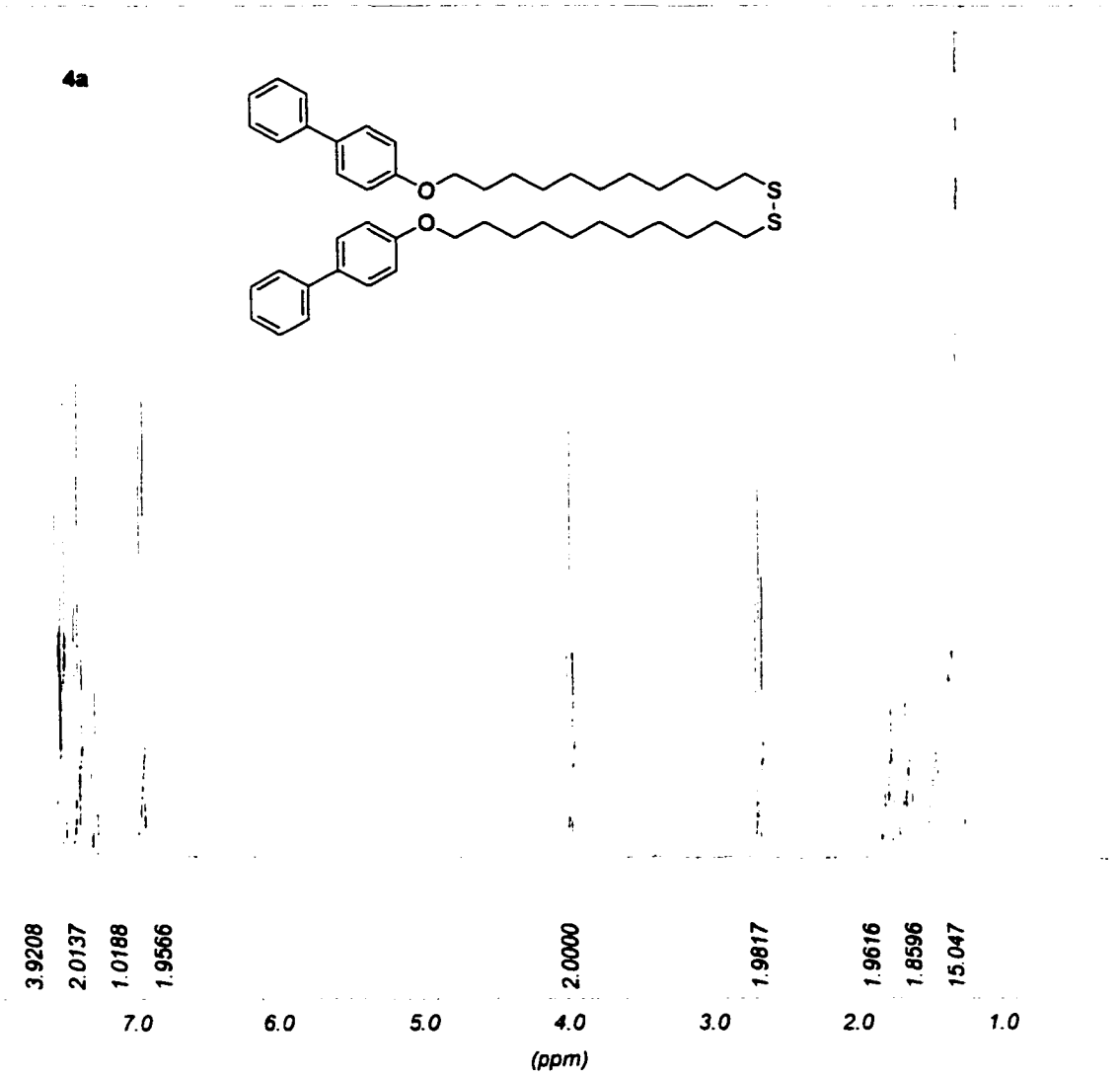
4a
O
O
S
S
3.9208
2.0137
1.0188
1.9566
2.0000
1.9817
1.9616
1.8596
15.047
7.0
6.0
5.0
4.0
3.0
2.0
1.0
(ppm)

3b

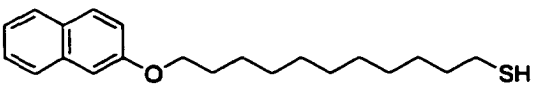
O
SH

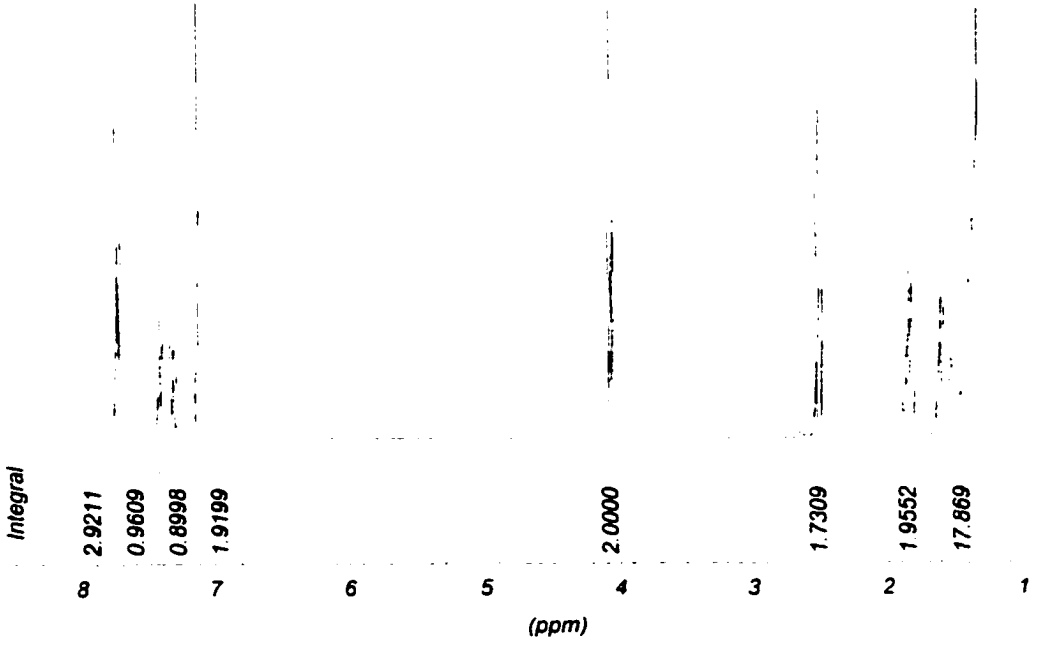
Integral
2.9211
0.9609
0.8998
1.9199
2.0000
1.7309
1.9552
17.869
8
7
6
5
4
3
2
1
(ppm)

4b

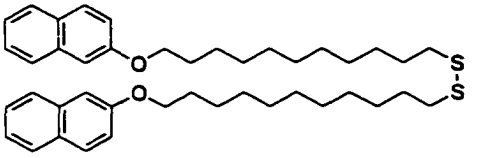
O
O
S
S

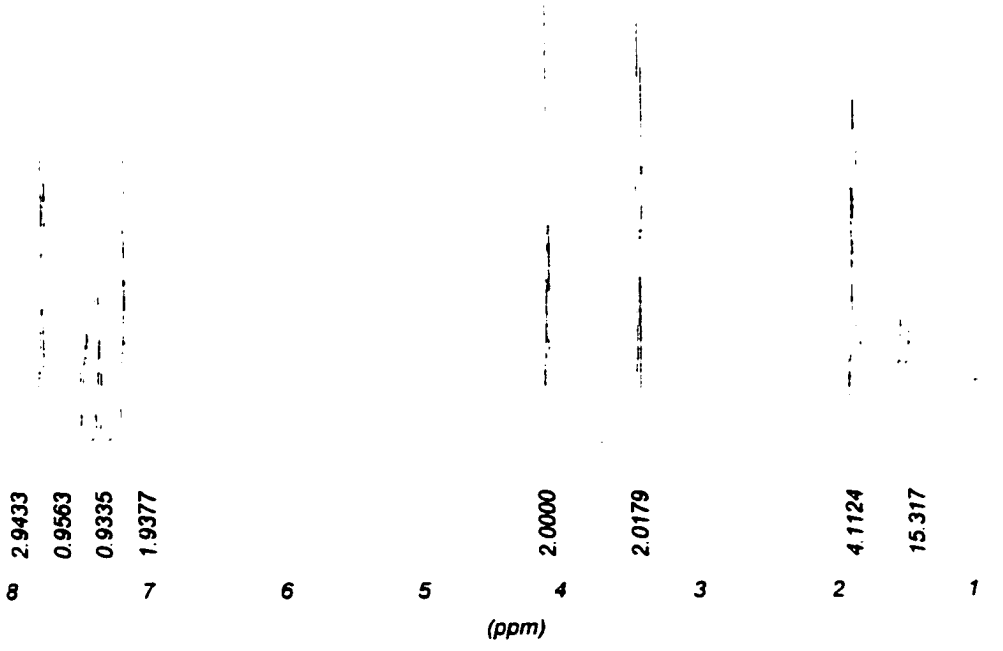
2.9433
0.9563
0.9335
1.9377
2.0000
2.0179
4.1124
15.317
8
7
6
5
4
3
2
1
(ppm)

References

(1) Hille, B. *Ionic Channels of Excitable Membranes*; Sinauer Associates, Incorporated: Sunderland, 1984.

(2) Haarer, D. *Angewandte Chemie-International Edition in English* **1989**, *28*, 1544-1547.

(3) Lundbaek, J. A.; Maer, A. M.; Andersen, O. S. *Biochemistry* **1997**, *36*, 5695-5701.

(4) Zubay, G. L. *Biochemistry*; Addison-Wesley: Reading, MA, 1983.

(5) Lodish, H. F.; Darnell, J. E. *Molecular cell biology*; 3rd ed.; Scientific American Books : Distributed by W.H. Freeman and Co.: New York, 1995.

(6) Zhou, Y. F.; Morais-Cabral, J. H.; Kaufman, A.; MacKinnon, R. *Nature* **2001**, *414*, 43-48.

(7) Miller, C. *Nature* **2001**, *414*, 23-24.

(8) Morais-Cabral, J. H.; Zhou, Y. F.; MacKinnon, R. *Nature* **2001**, *414*, 37-42.

(9) Berneche, S.; Roux, B. *Nature* **2001**, *414*, 73-77.

(10) Lear, J. D.; Schneider, J. P.; Kienker, P. K.; DeGrado, W. F. *Journal of the American Chemical Society* **1997**, *119*, 3212-3217.

(11) Lien, L.; Jaikaran, D. C. J.; Zhang, Z. H.; Woolley, G. A. *Journal of the American Chemical Society* **1996**, *118*, 12222-12223.

(12) Borisenko, V.; Sansom, M. S. P.; Woolley, G. A. *Biophysical Journal* **2000**, *78*, 1335-1348.

(13) Kumita, J. R.; Smart, O. S.; Woolley, G. A. *Proceedings of the National Academy of Sciences of the United States of America* **2000**, *97*, 3803-3808.

(14) Lear, J. D.; Wasserman, Z. R.; Degrado, W. F. *Science* **1988**, *240*, 1177-1181.

(15) Akerfeldt, K. S.; Lear, J. D.; Wasserman, Z. R.; Chung, L. A.; Degrado, W. F. *Accounts of Chemical Research* **1993**, *26*, 191-197.

(16) Woolley, G. A.; Zunic, V.; Karanicolas, J.; Jaikaran, A. S. I.; Starostin, A. V. *Biophysical Journal* **1997**, *73*, 2465-2475.

(17) Koeppe, R. E.; Andersen, O. S. *Annual Review of Biophysics and Biomolecular Structure* **1996**, *25*, 231-258.

(18) Woolley, G. A.; Kerr, I. D.; Sansom, M. S. P.; Wallace, B. A. *Biophysical Journal* **1993**, *64*, A300-A300.

(19) Woolley, G. A.; Wallace, B. A. *Journal of Membrane Biology* **1992**, *129*, 109-136.

(20) Koeppe, R. E.; Mazet, J. L.; Andersen, O. S. *Biochemistry* **1990**, *29*, 512-520.

(21) Russell, E. W. B.; Weiss, L. B.; Navetta, F. I.; Koeppe, R. E.; Andersen, O. S. *Biophysical Journal* **1986**, *49*, 673-686.

(22) Woolley, G. A.; Jaikaran, A. S. I.; Zhang, Z. H.; Peng, S. Y. *Journal of the American Chemical Society* **1995**, *117*, 4448-4454.

(23) Gokel, G. W.; Murillo, O. *Accounts of Chemical Research* **1996**, *29*, 425-432.

(24) Fyles, T. M.; Loock, D.; Zhou, X. *Canadian Journal of Chemistry-Revue Canadienne De Chimie* **1998**, *76*, 1015-1026.

(25) Clark, T. D.; Buehler, L. K.; Ghadiri, M. R. *Journal of the American Chemical Society* **1998**, *120*, 651-656.

(26) Murray, C. L.; Shabany, H.; Gokel, G. W. *Physical Chemistry Chemical Physics* **2000**, *2*, 2371-2372.

(27) Seebach, D.; Brunner, A.; Burger, H. M.; Reusch, R. N.; Bramble, L. L. *Helvetica Chimica Acta* **1996**, *79*, 507-517.

(28) Matile, S. *Chemical Society Reviews* **2001**, *30*, 158-167.

(29) Sakai, N.; Matile, S. *Chemistry-a European Journal* **2000**, *6*, 1731-1737.

(30) Yoshino, N.; Satake, A.; Kobuke, Y. *Angewandte Chemie-International Edition* **2001**, *40*, 457-459.

(31) Kobuke, Y.; Nagatani, T. *Journal of Organic Chemistry* **2001**, *66*, 5094-5101.

(32) Otto, S.; Osifchin, M.; Regen, S. L. *Journal of the American Chemical Society* **1999**, *121*, 10440-10441.

(33) Deng, G.; Dewa, T.; Regen, S. L. *Journal of the American Chemical Society* **1996**, *118*, 8975-8976.

(34) Deng, G.; Merritt, M.; Yamashita, K.; Janout, V.; Sadownik, A.; Regen, S. L. *Journal of the American Chemical Society* **1996**, *118*, 3307-3308.

(35) Bandyopadhyay, P.; Janout, V.; Zhang, L. H.; Sawko, J. A.; Regen, S. L. *Journal of the American Chemical Society* **2000**, *122*, 12888-12889.

(36) DiGiorgio, A. F.; Otto, S.; Bandyopadhyay, P.; Regen, S. L. *Journal of the American Chemical Society* **2000**, *122*, 11029-11030.

(37) Bolard, J. *Biochimica et Biophysica Acta* **1986**, *864*, 257.

(38) Winum, J. Y.; Matile, S. *Journal of the American Chemical Society* **1999**, *121*, 7961-7962.

(39) Ni, C. Y.; Matile, S. *Chemical Communications* **1998**, 755-756.

(40) Baumeister, B.; Sakai, N.; Matile, S. *Angewandte Chemie-International Edition* **2000**, *39*, 1955.

(41) Tedesco, M. M.; Ghebremariam, B.; Sakai, N.; Matile, S. *Angewandte Chemie International Edition* **1999**, *38*, 540-543.

(42) Sakai, N.; Gerard, D.; Matile, S. *Journal of the American Chemical Society* **2001**, *123*, 2517-2524.

(43) Robert, F.; Winum, J. Y.; Sakai, N.; Gerard, D.; Matile, S. *Organic Letters* **2000**, *2*, 37-39.

(44) Gokel, G. W.; Ferdani, R.; Liu, J.; Pajewski, R.; Shabany, H.; Uetrecht, P. *Chemistry-a European Journal* **2001**, *7*, 33-39.

(45) Abel, E.; Maguire, G. E. M.; Meadows, E. S.; Murillo, O.; Jin, T.; Gokel, G. W. *Journal of the American Chemical Society* **1997**, *119*, 9061-9062.

(46) Abel, E.; Meadows, E. S.; Suzuki, I.; Jin, T.; Gokel, G. W. *Chemical Communications* **1997**, 1145-1146.

(47) Cross, G. G.; Fyles, T. M. *Journal of Organic Chemistry* **1997**, *62*, 6226-6230.

(48) Fyles, T. M.; Loock, D.; vanStraatenNijenhuis, W. F.; Zhou, X. *Journal of Organic Chemistry* **1996**, *61*, 8866-8874.

(49) Fyles, T. M.; Hu, C. W.; Knoy, R. *Organic Letters* **2001**, *3*, 1335-1337.

(50) Hu, C. W. *unpublished* **2002.**

(51) Doyle, D. A. *Science* **1998**, *280*, 69-77.

(52) Lehn, J.-M. *Angewandte Chemie International Edition* **1990**, *29*, 1304-1319.

(53) Fyles, T. M.; James, T. D.; Pryhitka, A.; Zojaji, M. *Journal of Organic Chemistry* **1993**, *58*, 7456-7468.

(54) Fyles, T. M.; James, T. D.; Kaye, K. C. *Journal of the American Chemical Society* **1993**, *115*, 12315-12321.

(55) Kobuke, Y.; Ueda, K.; Sokabe, M. *Chemistry Letters* **1995**, 435-436.

(56) Kobuke, Y. *Journal of Synthetic Organic Chemistry Japan* **1995**. *53*, 451-460.

(57) Tanaka, Y.; Kobuke, Y.; Sokabe, M. *Angewandte Chemie-International Edition in English* **1995**, *34*, 693-694.

(58) Voyer, N.; Robitaille, M. *Abstracts of Papers of the American Chemical Society* **1994**, *207*, 450-ORGN.

(59) Voyer, N.; Robitaille, M. *Journal of the American Chemical Society* **1995**, *117*, 6599-6600.

(60) Zhou, X., Ph. D. Dissertation, University of Victoria, Victoria, BC, 1997.

(61) Loock, D., Ph. D. Dissertation, University of Victoria, Victoria, BC, 1997.

(62) Dubois, L. H.; Nuzzo, R. G. *Annual Review of Physical Chemistry* **1992**, *43*, 437-463.

(63) Smela, E. *Langmuir* **1998**, *14*, 2996-3002.

(64) Himmel, H. J.; Woll, C.; Gerlach, R.; Polanski, G.; Rubahn, H. G. *Langmuir* **1997**, *13*, 602-605.

(65) Hu, K.; Bard, A. J. *Langmuir* **1998**, *14*, 4790-4794.

(66) Oyamatsu, D.; Nishizawa, M.; Kuwabata, S.; Yoneyama, H. *Langmuir* **1998**, *14*, 3298-3302.

(67) Beulen, M. W. J.; Kastenberg, M. I.; van Veggel, F.; Reinhoudt, D. N. *Langmuir* **1998**, *14*, 7463-7467.

(68) Nelson, K. E.; Gamble, L.; Jung, L. S.; Boeckl, M. S.; Naeemi, E.; Golledge, S. L.; Sasaki, T.; Castner, D. G.; Campbell, C. T.; Stayton, P. S. *Langmuir* **2001**, *17*, 2807-2816.

(69) Haag, R.; Rampi, M. A.; Holmlin, R. E.; Whitesides, G. M. *Journal of the American Chemical Society* **1999**, *121*, 7895-7906.

(70) Shon, Y. S.; Lee, S.; Perry, S. S.; Lee, T. R. *Journal of the American Chemical Society* **2000**, *122*, 1278-1281.

(71) Zhang, H. L.; Chen, M.; Li, H. L. *Journal of Physical Chemistry B* **2000**, *104*, 28-36.

(72) Imabayashi, S.; Hobara, D.; Kakiuchi, T. *Langmuir* **2001**, *17*, 2560-2563.

(73) Tsao, M. W.; Rabolt, J. F.; Schonherr, H.; Castner, D. G. *Langmuir* **2000**, *16*, 1734-1743.

(74) Huang, E.; Zhou, F. M.; Deng, L. *Langmuir* **2000**, *16*, 3272-3280.

(75) Dijksma, M.; Kamp, B.; Hoogvliet, J. C.; van Bennekom, W. P. *Langmuir* **2000**, *16*, 3852-3857.

(76) Boeckl, M. S.; Bramblett, A. L.; Hauch, K. D.; Sasaki, T.; Ratner, B. D.; Rogers, J. W. *Langmuir* **2000**, *16*, 5644-5653.

(77) Liao, S.; Shnidman, Y.; Ulman, A. *Journal of the American Chemical Society* **2000**, *122*, 3688-3694.

(78) Shon, Y. S.; Lee, T. R. *Journal of Physical Chemistry B* **2000**, *104*, 8182-8191.

(79) Ma, F. Y.; Lennox, R. B. *Langmuir* **2000**, *16*, 6188-6190.

(80) Hobara, D.; Sasaki, T.; Imabayashi, S.; Kakiuchi, T. *Langmuir* **1999**, *15*, 5073-5078.

(81) Terrill, R. H.; Balss, K. M.; Zhang, Y. M.; Bohn, P. W. *Journal of the American Chemical Society* **2000**, *122*, 988-989.

(82) Mohri, N.; Matsushita, S.; Inoue, M.; Yoshikawa, K. *Langmuir* **1998**, *14*, 2343-2347.

(83) Kakiuchi, T.; Sato, K.; Iida, M.; Hobara, D.; Imabayashi, S.; Niki, K. *Langmuir* **2000**, *16*, 7238-7244.

(84) Imabayashi, S.; Hobara, D.; Kakiuchi, T.; Knoll, W. *Langmuir* **1997**, *13*, 4502-4504.

(85) Mulder, W. H.; Calvente, J. J.; Andreu, R. *Langmuir* **2001**, *17*, 3273-3280.

(86) Schneider, T. W.; Buttry, D. A. *Abstracts of Papers of the American Chemical Society* **1992**, *203*, 34-ANYL.

(87) Zhong, C. J.; Zak, J.; Porter, M. D. *Journal of Electroanalytical Chemistry* **1997**, *421*, 9-13.

(88) Imabayashi, S.; Iida, M.; Hobara, D.; Feng, Z. Q.; Niki, K.; Kakiuchi, T. *Journal of Electroanalytical Chemistry* **1997**, *428*, 33-38.

(89) Vinokurov, I. A.; Morin, M.; Kankare, J. *Journal of Physical Chemistry B* **2000**, *104*, 5790-5796.

(90) Byloos, M.; Al-Maznai, H.; Morin, M. *Journal of Physical Chemistry B* **2001**, *105*, 5900-5905.

(91) Byloos, M.; Al-Maznai, H.; Morin, M. *Journal of Physical Chemistry B* **1999**, *103*, 6554-6561.

(92) Byloos, M.; Rifai, S.; Al-Maznai, H.; Laferriere, M.; Morin, M. *Langmuir* **2001**, *17*, 2478-2484.

(93) Yang, D. F.; Wilde, C. P.; Morin, M. *Langmuir* **1997**, *13*, 243-249.

(94) Yang, D. F.; Wilde, C. P.; Morin, M. *Langmuir* **1996**, *12*, 6570-6577.

(95) Hobara, D.; Yamamoto, M.; Kakiuchi, T. *Chemistry Letters* **2001**, 374-375.

(96) Yang, D. F.; Morin, M. *Journal of Electroanalytical Chemistry* **1997**, *429*, 1-5.

(97) Yang, D. F.; AlMaznai, H.; Morin, M. *Journal of Physical Chemistry B* **1997**, *101*, 1158-1166.

(98) Kawaguchi, T.; Yasuda, H.; Shimazu, K.; Porter, M. D. *Langmuir* **2000**, *16*, 9830-9840.

(99) Walczak, M. M.; Popenoe, D. D.; Deinhammer, R. S.; Lamp, B. D.; Chung, C. K.; Porter, M. D. *Langmuir* **1991**, *7*, 2687-2693.

(100) Imabayashi, S.; Gon, N.; Sasaki, T.; Hobara, D.; Kakiuchi, T. *Langmuir* **1998**, *14*, 2348-2351.

(101) Imahori, H.; Norieda, H.; Nishimura, Y.; Yamazaki, I.; Higuchi, K.; Kato, N.; Motohiro, T.; Yamada, H.; Tamaki, K.; Arimura, M.; Sakata, Y. *Journal of Physical Chemistry B* **2000**, *104*, 1253-1260.

(102) Lamont, C. L. A.; Wilkes, J. *Langmuir* **1999**, *15*, 2037-2042.

(103) Miller, C.; Cuendet, P.; Gratzel, M. *Journal of Physical Chemistry* **1991**, *95*, 877-886.

(104) Zamborini, F. P.; Crooks, R. M. *Langmuir* **1998**, *14*, 3279-3286.

(105) Reese, S.; Fox, M. A. *Journal of Physical Chemistry B* **1998**, *102*, 9820-9824.

(106) Chechik, V.; Schonherr, H.; Vancso, G. J.; Stirling, C. J. M. *Langmuir* **1998**, *14*, 3003-3010.

(107) Labayen, M., Ph. D. dissertation, University of Victoria, Victoria, B. C., 2002.

(108) Bain, C. D.; Troughton, B.; Tao, Y. T.; Evall, J.; Whitesides, G. M.; Nuzzo, R. G. *Journal of the American Chemical Society* **1989**, *111*, 321-335.

(109) Nakashima, N.; Takada, Y.; Kunitake, M.; Manabe, O. *Journal of the Chemical Society Chemical Communications* **1990**, *12*, 845-847.

(110) Takehara, K.; Takemura, H.; Ide, Y. *Electrochimica Acta* **1994**, *39*, 817-822.

(111) Nuzzo, R. G.; Zegarski, B. R.; Dubois, L. H. *Journal of the American Chemical Society* **1987**, *109*, 733-740.

(112) Dannenberger, O.; Wolff, J. J.; Buck, M. *Langmuir* **1998**, *14*, 4679-4682.

(113) Terrill, R. H.; Tanzer, T. A.; Bohn, P. W. *Langmuir* **1998**, *14*, 845-854.

(114) Jung, C.; Dannenberger, O.; Xu, Y.; Buck, M.; Grunze, M. *Langmuir* **1998**, *14*, 1103-1107.

(115) Chechik, V.; Stirling, C. J. M. *Langmuir* **1998**, *14*, 99-105.

(116) Bensebaa, F.; Ellis, T. H.; Badia, A.; Lennox, R. B. *Langmuir* **1998**, *14*, 2361-2367.

(117) French, M.; Creager, S. E. *Langmuir* **1998**, *14*, 2129-2133.

(118) Schonherr, H.; Ringsdorf, H.; Jaschke, M.; Butt, H. J.; Bamberg, E.; Allinson, H.; Evans, S. D. *Langmuir* **1996**, *12*, 3898-3904.

(119) Schoenfisch, M. H.; Pemberton, J. E. *Journal of the American Chemical Society* **1998**, *120*, 4502-4513.

(120) Lee, M. T.; Hsueh, C. C.; Freund, M. S.; Ferguson, G. S. *Langmuir* **1998**, *14*, 6419-6423.

(121) Schessler, H. M.; Karpovich, D. S.; Blanchard, G. J. *Journal of the American Chemical Society* **1996**, *118*, 9645-9651.

(122) Tao, Y. T.; Wu, C. C.; Eu, J. Y.; Lin, W. L. *Langmuir* **1997**, *13*, 4018-4023.

(123) Peterlinz, K. A.; Georgiadis, R. *Langmuir* **1996**, *12*, 4731-4740.

(124) Kang, J.; Rowntree, P. A. *Langmuir* **1996**, *12*, 2813-2819.

(125) Camillone, N.; Leung, T. Y. B.; Schwartz, P.; Eisenberger, P.; Scoles, G. *Langmuir* **1996**, *12*, 2737-2746.

(126) Ishida, T.; Hara, M.; Kojima, I.; Tsuneda, S.; Nishida, N.; Sasabe, H.; Knoll, W. *Langmuir* **1998**, *14*, 2092-2096.

(127) Vanderah, D. J.; Pham, C. P.; Springer, S. K.; Silin, V.; Meuse, C. W. *Langmuir* **2000**, *16*, 6527-6532.

(128) Cooper, E.; Leggett, G. J. *Langmuir* **1999**, *15*, 1024-1032.

(129) Boubour, E.; Lennox, R. B. *Langmuir* **2000**, *16*, 4222-4228.

(130) Boubour, E.; Lennox, R. B. *Langmuir* **2000**, *16*, 7464-7470.

(131) Badia, A.; Lennox, R. B.; Reven, L. *Accounts of Chemical Research* **2000**, *33*, 475-481.

(132) Smith, D. A.; Wallwork, M. L.; Zhang, J.; Kirkham, J.; Robinson, C.; Marsh, A.; Wong, M. *Journal of Physical Chemistry B* **2000**, *104*, 8862-8870.

(133) Hagenstrom, H.; Schneeweiss, M. A.; Kolb, D. M. *Langmuir* **1999**, *15*, 2435-2443.

(134) Bensebaa, F.; Voicu, R.; Huron, L.; Ellis, T. H.; Kruus, E. *Langmuir* **1997**, *13*, 5335-5340.

(135) Janek, R. P.; Fawcett, W. R.; Ulman, A. *Langmuir* **1998**, *14*, 3011-3018.

(136) Schlenoff, J. B.; Li, M.; Ly, H. *Journal of the American Chemical Society* **1995**, *117*, 12528-12536.

(137) Yu, H. Z.; Ye, S.; Zhang, H. L.; Uosaki, K.; Liu, Z. F. *Langmuir* **2000**, *16*, 6948-6954.

(138) Sugihara, K.; Shimazu, K.; Uosaki, K. *Langmuir* **2000**, *16*, 7101-7105.

(139) Hasan, M.; Bethell, D.; Brust, M. *Journal of the American Chemical Society* **2002**, *124*, 1132-1133.

(140) Ishida, T.; Yamamoto, S.; Mizutani, W.; Motomatsu, M.; Tokumoto, H.; Hokari, H.; Azehara, H.; Fujihira, M. *Langmuir* **1997**, *13*, 3261-3265.

(141) Bandyopadhyay, K.; Vijayamohanan, K. *Langmuir* **1998**, *14*, 625-629.

(142) Molinero, V.; Calvo, E. J. *Journal of Electroanalytical Chemistry* **1998**, *445*, 17-25.

(143) Bandyopadhyay, K.; Patil, V.; Sastry, M.; Vijayamohanan, K. *Langmuir* **1998**, *14*, 3808-3814.

(144) Avila, A.; Gregory, B. W.; Niki, K.; Cotton, T. M. *Journal of Physical Chemistry B* **2000**, *104*, 2759-2766.

(145) Offord, D. A.; Sachs, S. B.; Ennis, M. S.; Eberspacher, T. A.; Griffin, J. H.; Chidsey, C. E. D.; Collman, J. P. *Journal of the American Chemical Society* **1998**, *120*, 4478-4487.

(146) Crooks, R. M.; Ricco, A. J. *Accounts of Chemical Research* **1998**, *31*, 219-227.

(147) Patolsky, F.; Katz, E.; Bardea, A.; Willner, I. *Langmuir* **1999**, *15*, 3703-3706.

(148) Lukkari, J.; Kleemola, K.; Meretoja, M.; Ollonqvist, T.; Kankare, J. *Langmuir* **1998**, *14*, 1705-1715.

(149) Brousseau, L. C.; Zhao, Q.; Shultz, D. A.; Feldheim, D. L. *Journal of the American Chemical Society* **1998**, *120*, 7645-7646.

(150) Green, M.; P, O. B. *Chemical Communications* **2000**, 183-184.

(151) Templeton, A. C.; Hostetler, M. J.; Warmoth, E. K.; Chen, S. W.; Hartshorn, C. M.; Krishnamurthy, V. M.; Forbes, M. D. E.; Murray, R. W. *Journal of the American Chemical Society* **1998**, *120*, 4845-4849.

(152) Ingram, R. S.; Murray, R. W. *Langmuir* **1998**, *14*, 4115-4121.

(153) Tao, G. L.; Katz, E.; Willner, I. *Chemical Communications* **1997**, 2073-2074.

(154) Flink, S.; Boukamp, B. A.; vandenBerg, A.; vanVeggel, F.; Reinhoudt, D. N. *Journal of the American Chemical Society* **1998**, *120*, 4652-4657.

(155) Fox, M. A.; Whitesell, J. K.; McKerrow, A. J. *Langmuir* **1998**, *14*, 816-820.

(156) Li, W. J.; Lynch, V.; Thompson, H.; Fox, M. A. *Journal of the American Chemical Society* **1997**, *119*, 7211-7217.

(157) Chechik, V.; Crooks, R. M.; Stirling, C. J. M. *Advanced Materials* **2000**, *12*, 1161-1171.

(158) Brockman, J. M.; Frutos, A. G.; Corn, R. M. *Journal of the American Chemical Society* **1999**, *121*, 8044-8051.

(159) Hodneland, C. D.; Mrksich, M. *Langmuir* **1997**, *13*, 6001-6003.

(160) Lahiri, J.; Ostuni, E.; Whitesides, G. M. *Langmuir* **1999**, *15*, 2055-2060.

(161) Sabapathy, R. C.; Bhattacharyya, S.; Cleland, W. E.; Hussey, C. L. *Langmuir* **1998**, *14*, 3797-3807.

(162) Moav, T.; Hatzor, A.; Cohen, H.; Libman, J.; Rubinstein, I.; Shanzer, A. *Chemistry- A European Journal* **1998**, *4*, 502-507.

(163) Hou, Y. C.; Chen, Y. S.; Amro, N. A.; Wadu Mesthrige, K.; Andreana, P. R.; Liu, G.; Wang, P. G. *Chemical Communications* **2000**, 1831-1832.

(164) Houmam, A.; Lawrence, I.; Loock, D.; Mauzeroll, J.; Lee, L.; Lennox, R. B. *unpublished* **2001**, 1-17.

(165) Persson, H. H. J.; Caseri, W. R.; Suter, U. W. *Langmuir* **2001**, *17*, 3643-3650.

(166) Perez-Luna, V. H.; O'Brien, M. J.; Opperman, K. A.; Hampton, P. D.; Lopez, G. P.; Klumb, L. A.; Stayton, P. S. *Journal of the American Chemical Society* **1999**, *121*, 6469-6478.

(167) Pilloud, D. L.; Chen, X. X.; Dutton, P. L.; Moser, C. C. *Journal of Physical Chemistry B* **2000**, *104*, 2868-2877.

(168) Schierbaum, K. D.; Weiss, T.; Vanvelzen, E. U. T.; Engbersen, J. F. J.; Reinhoudt, D. N.; Gopel, W. *Science* **1994**, *265*, 1413-1415.

(169) Kanayama, N.; Kanbara, T.; Kitano, H. *Journal of Physical Chemistry B* **2000**, *104*, 271-278.

(170) Flink, S.; van Veggel, F.; Reinhoudt, D. N. *Journal of Physical Chemistry B* **1999**, *103*, 6515-6520.

(171) Walter, D. G.; Campbell, D. J.; Mirkin, C. A. *Journal of Physical Chemistry B* **1999**, *103*, 402-405.

(172) Ista, L. K.; Mendez, S.; Perez-Luna, V. H.; Lopez, G. P. *Langmuir* **2001**, *17*, 2552-2555.

(173) Shipway, A. N.; Willner, I. *Accounts of Chemical Research* **2001**, *34*, 421-432.

(174) Sfez, R.; De-Zhong, L.; Turyan, I.; Mandler, D.; Yitzchaik, S. *Langmuir* **2001**, *17*, 2556-2559.

(175) Smith, E. A.; Wanat, M. J.; Cheng, Y. F.; Barreira, S. V. P.; Frutos, A. G.; Corn, R. M. *Langmuir* **2001**, *17*, 2502-2507.

(176) Sabapathy, R. C.; Crooks, R. M. *Langmuir* **2000**, *16*, 1777-1782.

(177) Friggeri, A.; Schonherr, H.; van Manen, H. J.; Huisman, B. H.; Vancso, G. J.; Huskens, J.; van Veggel, F.; Reinhoudt, D. N. *Langmuir* **2000**, *16*, 7757-7763.

(178) Chapman, R. G.; Ostuni, E.; Yan, L.; Whitesides, G. M. *Langmuir* **2000**, *16*, 6927-6936.

(179) Clegg, R. S.; Hutchison, J. E. *Langmuir* **1996**, *12*, 5239-5243.

(180) Sek, S.; Misicka, A.; Bilewicz, R. *Journal of Physical Chemistry B* **2000**, *104*, 5399-5402.

(181) Clegg, R. S.; Hutchison, J. E. *Journal of the American Chemical Society* **1999**, *121*, 5319-5327.

(182) Reek, J. N. H.; Priem, A. H.; Engelkamp, H.; Rowan, A. E.; Elemans, J.; Nolte, R. J. M. *Journal of the American Chemical Society* **1997**, *119*, 9956-9964.

(183) Rudkevich, D. M.; Hilmersson, G.; Rebek, J. *Journal of the American Chemical Society* **1997**, *119*, 9911-9912.

(184) Schmitt, H.; Badia, A.; Dickinson, L.; Reven, L.; Lennox, R. B. *Advanced Materials* **1998**, *10*, 475.

(185) Bard, A. J.; Faulkner, L. R. *Electrochemical Methods : Fundamentals and Applications*; Wiley: New York, 1980.

(186) Buck, R. P.; Lindner, E. *Accounts of Chemical Research* **1998**, *31*, 257-266.

(187) Rodriguez, J. F.; Mebrahtu, T.; Soriaga, M. P. *Journal of Electroanalytical Chemistry* **1987**, *233*, 283-289.

(188) Oesch, U.; Janata, J. *Electrochimica Acta* **1983**, *28*, 1237-1246.

(189) Deakin, M. R.; Melroy, O. *Journal of Electroanalytical Chemistry* **1988**, *239*, 321-331.

(190) Eggers, P., Master's Thesis, University of Victoria, Victoria, B.C., 2002.

(191) Cameron, L. M., Ph. D. dissertation, University of Victoria, Victoria, B. C., 1997.

(192) Cross, G. G., Ph. D. dissertation, University of Victoria, Victoria, B. C., 1994.

(193) Zeng, B., Ph. D. dissertation, University of Victoria, Victoria, B. C., 1997.

(194) Knoy, R., Master's Thesis, University of Victoria, Victoria, B. C., 2001.

(195) Morf, W. *Personal Communication* **1976**.

(196) Mathews, C. K.; van Holde, K. E. *Biochemistry*; The Benjamin/Cummings Publishing Company: Redwood City, CA, 1990.

(197) Schanberg, E. *Berichte der Bunsen-Gesellschaft Physical Chemistry Chemical Physics* **1942**, *75B*, 468.

(198) Buchmann, M. B.; Fyles, T. M.; Mischki, T.; Sutherland, T.; Tong, C. C.; Yip, V. L. Y. *Arkivoc* **2001**, *2*, U9-U16.

(199) Buchmann, M. B. *unpublished* **2002**.